Silicon Photomultipliers as Optical Wireless Receivers in Ambient Light

Characterisation, Modelling, Monte-Carlo Simulation, and Mitigation of Ambient Light

This thesis is submitted to the Department of Engineering Science, University of Oxford, in partial fulfilment of the requirements for the degree of Doctor of Philosophy.

William Matthews

University College

Supervised by Professor Steve Collins

January 18, 2024

UNIVERSITY OF
OXFORD

Declaration

I declare that this thesis is entirely my own work, and except where otherwise stated, describes my own research performed in the Department of Engineering Science at the University of Oxford between October 2019 and July 2023 under the general supervision of Professor Steve Collins.

W. A. Matthews,

University College

0.1 Abstract

Existing RF wireless communications systems are increasingly struggling to guarantee the quality of service expected by users, especially in environments with many terminals [1]. Visible light communication (VLC) systems are consequently being considered as a solution to this problem, as they offer the potential for densely packing channels in space and do not contribute to RF congestion. Receivers based upon silicon photomultipliers (SiPMs) have been shown to be more sensitive than other VLC receivers, for on-off keying (OOK) data rates less than 1.5 Gbps [2]. Despite having the ability to detect individual photons, one of the major issues in using a SiPM as a receiver is device saturation. SiPM saturation may begin at low irradiances (starting at 10 mWm^{-2} at 405 nm for a J-Series 30020 SiPM), which may be from either a transmitter or ambient light.

In this thesis, two off the shelf SiPMs are investigated as an OOK VLC receiver these are both characterised and compared in their operating performance. A robust optical communications system using a SiPM as a receiver, operating at 405 nm in eye-safe irradiances is described. The highest performing SiPM of the two is further pushed to operate in hostile environments with high ambient light levels. An alternative evaluation board is utilised to achieve a higher maximum count rate and probe SiPM saturation to understand the mechanisms at work.

The results from characterisation and operation in hostile environments is used to develop and validate an accurate Monte Carlo simulation of SiPMs, and the time domain non-linearity is explained as a consequence of the time taken to recharge a microcell. The simulation is used to 'look inside' the SiPM and examine typically unobservable parameters, and work is done to quantify the statistical process behind the distribution of time since detection. This Monte Carlo simulation is the first of its class that has been validated against experimental data.

Additionally, a new form of form of nonlinear inter-symbol interference (ISI) is presented, which occurs when a SiPM operates in ambient light causing time domain non-linearity. This is achieved through understanding the key mechanisms at play when ambient light illuminates a SiPM, and designing a new receiver that combines multiple SiPMs together to improve the system's ambient light performance as predicted by Poisson statistics.

Finally, a novel receiver is presented which allows for field of view selection in solid state. This receiver allows for reducing the impact of ambient light from a large field of regard, and the selection of transmitters.

0.2 Publications

Publications which result from this thesis:

1. W. Matthews, Z. Ahmed, W. Ali and S. Collins, "A SiPM-based VLC Receiver for 3.45 Gigabits/s Communication Using OOK Modulation," *2020 IEEE Photonics Conference (IPC)*, 2020, pp. 1-2
   doi: 10.1109/IPC47351.2020.9252218.

2. W. Ali, G. Faulkner, Z. Ahmed, W. Matthews, D. O'Brien and S. Collins, "Silicon photomultiplier receivers and future VLC systems," *2020 IEEE Globecom Workshops* (GC Wkshps, 2020, pp. 1-5, doi: 10.1109/GCWkshps50303.2020.9367590.

3. W. Matthews, W. Ali, Z. Ahmed, G. Faulkner and S. Collins, "Inter-Symbol Interference and Silicon Photomultiplier VLC Receivers in Ambient Light," in *IEEE Photonics Technology Letters*, vol. 33, no. 9, pp. 449-452, 1 May, 2021, doi: 10.1109/LPT.2021.3067511.

4. W. Matthews, Z. Ahmed, W. Ali and S. Collins, "A 3.45 Gigabits/s SiPM-Based OOK VLC Receiver," in *IEEE Photonics Technology Letters*, vol. 33, no. 10, pp. 487-490, 15 May, 2021, doi: 10.1109/LPT.2021.3069802.

5. W. Ali, G. Faulkner, Z. Ahmed, W. Matthews and S. Collins, "Giga-Bit Transmission Between an Eye-Safe Transmitter and Wide Field-of-View SiPM Receiver," in *IEEE Access*, vol. 9, pp. 154225-154236, 2021, doi: 10.1109/ACCESS.2021.3116704.

6. W. Matthews and S. Collins, "The negative impact of anode resistance on SiPMs as VLC receivers," *2022 17th Conference on Ph.D Research in Microelectronics and Electronics (PRIME)*, Villasimius, SU, Italy, pp. 41-44, 2022, doi: 10.1109/PRIME55000.2022.9816749.

7. W. Matthews, S. Collins "An Experimental and Numerical Study of

the Impact of Ambient Light of SiPMs in VLC Receivers," *Photonics*, 9(12):888, 2022. doi: 10.3390/photonics9120888

8. W. Matthews, S. Collins "A Roadmap for Gigabit to Terabit Optical Wireless Communications Receivers," *Sensors* 23(3):1101, 2023. doi: 10.3390/s23031101

9. W. Matthews, S. Collins "Transmitter Selection in Solid-State Field of View Selection for Optical Wireless Receivers," In Preparation

10. W. Matthews, S. Collins "Ambient Light Control in Solid-State Field of View Selection for Optical Wireless Receivers," In Preparation

Additional publications, which arise from work supplementary to the thesis:

1. W. Ali, W.Matthews, G. Faulkner and S. Collins, "A wide field-of-view receiver that incorporates fluorescent fibers and a SiPM," *OWC Conference Eindhoven 2021*, 2021

2. W. Ali, Z. Ahmed, W. Matthews and S. Collins, "The Impact of the Length of Fluorescent Fiber Concentrators on the Performance of VLC Receivers," in *IEEE Photonics Technology Letters*, vol. 33, no. 24, pp. 1451-1454, 15 Dec., 2021, doi: 10.1109/LPT.2021.3115965.

3. W. Matthews, C. He and S. Collins, "DCO-OFDM Channel Sounding with a SiPM Receiver," *2021 IEEE Photonics Conference (IPC)*, 2021, pp. 1-2, doi: 10.1109/IPC48725.2021.9592851.

4. G. Zhang, A. Schreier, X. Wang, W. Matthews, J. Farmer, G. Faulkner, S. Elston, S. Morris and D. O'Brien "Free-Space Optical Communication Link with Liquid Crystal Beam-steering". *Photonics Technology Letters*, vol. 35, no. 22, pp. 1199-1202, 15 Nov.15, 2023, doi: 10.1109/LPT.2023.3308774.

5. F. Liu, J. Farmer, A. Schreier, G. Faulkner, H. Chun, W. Matthews, Z. Wang, D. O'Brien "Ultra-Sensitive UV Solar-Blind Optical Wireless Communications with a SiPM", *Optics Letters*, 2023, doi: 10.1364/OL.503235

0.3 Acknowledgements

under pressure. I am especially grateful for you guiding me towards the scientific method while I was young, I know I would have made a mean biologist, but I hope that being an engineer comes a close second.

Finally I would like to thank my mother Elena, your practicality, realism and love built me to be the man I am today. From the solar car challenge to the many adventures in Bulgaria, you have forged the key principles in me that have proudly made me an engineer. I know we butt heads at times, but you have helped me grow beyond what I ever thought I could have achieved.

For Mum & Dad

"All my means are sane, my motive and my object mad."

Herman Melville, Moby Dick

Contents

List of Figures

List of Tables

Nomenclature

Acronyms and Initialisms

AC	Alternating Current
ADA	Angle Diversity Aperture
AP	Access Point
APD	Avalanche Photodiode
AWG	Arbitrary Waveform Generator
BER	Bit Error Rate
CAD	Computer Aided Design
dB	Decibel
DC	Direct Current
DFE	Decision Feedback Equalisation
FEC	Forward Error Correction
FoR	Field of Regard
FoV	Field of View
FoVSD	Field of View Selection Device
FWHM	Full Width Half Max
GM-APD	Geiger Mode Avalanche Photodiode
HDMI	High-Definition Multimedia Interface
IR	Infrared
ISI	Inter Symbol Interference
LASER	Light Amplification by Stimulated Emission of Radiation
LCD	Liquid Crystal Display
LED	Light Emitting Diode
LEQ	Linear Equalisation
MC	Monte Carlo
MIMO	Multiple Input Multiple Output
OFDM	Orthogonal Frequency Division Modulation
OOK	On Off Keying
OWC	Optical Wireless Communication
PCB	Printed Circuit Board
PD	Photodiode

PDE	Photon Detection Efficiency
PMT	Photomultiplier Tube
RF	Radio Frequency
RX	Receiver
SiPM	Silicon Photomultiplier
SMA	SubMiniature version A
SMT	Surface Mount Technology
SMTPA	SMT Pin Adaptor
SNR	Signal to Noise Ratio
SPAD	Single Photon Avalanche Diode
TSV	Through Silicon Via
TX	Transmitter
UV	Ultraviolet
VLC	Visible Light Communication
VNA	Vector Network Analyser
WDM	Wavelength Division Multiplexing
WLED	White LED

Mathematical Symbols

η	Photon Detection Efficiency
$\frac{\mathrm{d}D}{\mathrm{d}t}$	Photon Detection Rate
Λ	Rate Parameter
λ	Wavelength
$\mathbb{P}$	Probability
τ	Characteristic Recharge Time
A	Area
C_{cell}	Microcell Capacitance
D	Photon Detection Count
$E_p(\lambda)$	Photon Energy at Wavelength λ
I	Current
I_{photo}	Photocurrent
L	Optical Irradiance
Q_{cell}	Microcell Charge
t	Time
V	Voltage
V_{bias}	Bias Voltage
V_{br}	Breakdown Voltage
V_{over}	Overvoltage ($V_{\mathrm{bias}} - V_{\mathrm{br}}$)

Mathematical and Physical Constants

π Ratio of Circumference to Diameter of a Circle
3.14159265

c Speed of Light
299792485 $m\,s^{-1}$

e Euler's Number
2.71828183

h Planck Constant
6.62607015$\times 10^{-34}$ $J\,Hz^{-1}$

q Elementary Charge
1.60217663$\times 10^{-19}$ C

Physical Units

$\circ$ Degree, Unit of Angle (dimensionless)

Ω Ohm, Unit of Resistance ($kg\,m^2\,s^{-3}\,A^{-2}$)

A Ampere, Unit of Electrical Current ($C\,s^{-1}$)

b Bit, Unit of Information (base)

C Coulomb, Unit of Charge (SI base)

F Farad, Unit of Capacitance ($C\,V^{-1}$)

Hz Frequency, Unit of Frequency (s^{-1})

kg Kilogram, Unit of Mass (SI base)

m Metre, Unit of Distance (SI base)

s Second, Unit of Time (SI base)

V Volt, Unit of Electrical Potential ($kg\,m^2\,s^{-3}\,A^{-1}$)

W Watt, Unit of Power ($kg\,m\,s^{-2}$)

Chapter 1

Introduction

1.1 Motivations for the Field

Wireless services have become an important part of modern life by providing convenient high data transmission rate links for mobile users. Existing radio frequency (RF) wireless communications systems are increasingly struggling to guarantee the quality of service expected by users, especially in environments with high-density traffic [1]. For example, a Wi-Fi Access Point (AP) may have a high capacity of approximately 900 Mbit/s under normal operation, however due to concurrency effects, 18 connected users will each experience a rate of $\approx$6 Mbit/s. This is an overall throughput of $\approx$108 Mbit/s [1], only 11% of the total capacity of the Radio Frequency (RF) channels available. This phenomenon is due to users of the network performing 'access requests', which request permission to transmit from the AP to transmit data. These requests from different clients clash, meaning the AP cannot decipher the messages sent, so each user must try to repetitively send an access request again. This effect only worsens with more connected devices. As a solution Huawei has included another RF channel on their new enterprise AP, which transmits WiFi on a separate channel. The new AP from Huawei (AP4050DN-HD) has three RF channels, which are only present to reduce the number users on each channel [1]. This addition of a third RF

channel only solves the immediate problem, and merely pushes the issue into the future a few years. This new RF channel will eventually become saturated, and only add more power to the RF environment, increasing the amount of interference. Adding more RF channels is not sustainable, as the computation complexity and RF equipment required to continue this pathway prohibit direct scaling with throughput and availability.

A longer term solution is required, so supplementary to RF, a visible light communications (VLC) channel could be used to augment last mile data delivery and remove RF congestion, while ensuring quality of service and satisfied future bandwidth requirements [3]. VLC is a subset of optical wireless communication (OWC), which has the limitation that the optical bands used must be visible. When contrasted to RF systems, VLC offers advantages in using unlicensed bands (any electromagnetic wave with a frequency above 300 GHz is unlicensed in the USA), the ease of localisation to support high user densities, which is where RF typically has quality of service problems, and the prevention of eavesdropping. Other scenarios where VLC links are applicable are in high RF noise environments (e.g. some factories which use spot welders or high power machinery) or environments where light propagates further relative to RF, (e.g. underwater environments) [4, 5, 6, 7].

Over 70% of all mobile traffic occurs indoors, which suggests a significant demand to use VLC to offload indoor traffic within future heterogeneous networks. [8] As of March 2017, there is a Task Group with the responsibility of defining an emerging IEEE standard, IEEE 802.15.13. This emerging standard aims to define the physical (PHY) and Media Access Control (MAC) layers of visible light communications channels, with an emphasis on 'Li-Fi' [9]. Interest in current and future capability of VLC is demonstrated by this standard, coupled with startups such as PureLifi, and a more established businesses such as Signify. PureLifi is a startup looking to produce integrated circuits, transmitters and receivers

to enable VLC communication in a practical manner on mobile devices. In contrast, Signify is a lighting company wishing to add value to lighting products now that their old business model (replacing bulbs frequently) has been destroyed by the use of comparatively long-life WLEDs.

1.2 Optical Wireless Communications (OWC)

OWC is a subset of wireless communications, which uses the visible light spectrum to transmit data. OWC has been a topic of research for many years, and has been used in many applications, including inter-satellite communications, and short range indoor communications. For example, the first OWC link was demonstrated in 1880, when Alexander Graham Bell used sunlight to transmit audio signals [10]. Since then, OWC has been under active research.

1.3 Visible Light Communications (VLC)

VLC is a compelling subset of OWC, leveraging the *visible* light spectrum to provide high speed wireless communications. VLC systems are typically composed of a transmitter, a receiver, and a communication channel.

1.3.1 Differences between VLC and RF

VLC and RF are both forms of wireless communications, however VLC and RF are fundamentally different.

Propagation The propagation of light is fundamentally different to RF. Light is an electromagnetic wave, and hence is subject to the same laws of physics as RF. However, the wavelength of light is much smaller than RF, which means that light is more easily blocked by objects, and does not diffract as much as RF.

Interference Interference is a key difference between VLC and RF. VLC systems are typically deployed indoors, and hence the interference is typically from other VLC transmitters, which are typically con-

trolled by the same entity. RF systems are also typically indoors, however the interference is typically from other RF transmitters, which are typically controlled by different entities. This means that VLC systems can be designed to cooperate with each other, and hence can be designed to avoid interference. RF systems cannot be designed to cooperate with each other, and hence must be designed to tolerate interference.

Bandwidth The bandwidth of light is much higher than RF, which means that VLC systems can support higher data rates than RF systems. This is due to the Shannon-Hartley theorem, which states that the maximum data rate of a system is proportional to the bandwidth of the system.

Security VLC systems are inherently more secure than RF systems, as light does not propagate through walls. This means that an eavesdropper must be in the same room as the transmitter and receiver to intercept the signal. This is in contrast to RF systems, where an eavesdropper can be in a different room to the transmitter and receiver, and still intercept the signal.

Range The range of VLC systems is much lower than RF systems, which means that VLC systems are typically used for indoor communications. This is in contrast to RF systems, which can be used for indoor and outdoor communications.

VLC systems are not without their disadvantages, which, for the most part, are due to the fundamental differences between light and RF. For example, VLC systems have struggled to achieve the same range as RF systems, and are typically limited to indoor communications. Additionally, VLC systems are typically more expensive than RF systems, as the components used in VLC systems are more expensive than the components used in RF systems.

Another case where VLC struggles is outdoor communications, as the sun is a very bright source of light, which will saturate the receiver. This is in contrast to RF systems, which are not affected by the sun, as the sun does not emit RF. Additionally, RF systems do not rely on line of sight, as RF can diffract around objects, whereas light cannot.

1.3.2 Free Space Optics (FSO)

Free space optics (FSO) is a subset of OWC which uses lasers to transmit data through free space. Free space is any unguided physical medium or environment through which light propagates without being confined to a physical waveguide.

FSO is typically used to transmit data over long distances, and is used in applications such as inter-satellite communications. FSO uses lasers or highly collimated light sources to transmit data, and hence requires a line of sight between the transmitter and receiver. In contrast, VLC does not require collimated light sources, and can use light sources which have a wide beam angle. The range of FSO is typically much longer than VLC, with FSO links being able to transmit data over distances of 100 km [11]. VLC links are typically much shorter, with a maximum range of 10 m [12].

1.3.3 Components of a VLC System

VLC systems, like all wireless communications systems, are composed of a transmitter, a receiver, and a communication channel. The transmitter is responsible for encoding data into a signal, and transmitting the signal through the communication channel. The receiver is responsible for receiving the signal from the communication channel, and decoding the signal into data. The communication channel is responsible for transmitting the signal from the transmitter to the receiver.

In VLC systems, transmitters include light emitting diodes (LEDs), lasers, and organic light emitting diodes (OLEDs). The channel is free space, as wireless VLC systems do not use waveguides. The receiver

has many different forms, which this this introduction will now discuss.

1.3.4 VLC Receivers

Currently, there are no commercially available VLC systems. There are many reasons for this, including the lack of a standards, the lack of a business case, and the lack of a suitable receiver. However, there are many research groups working on VLC systems, and many different receivers have been used in the pursuit of a practical VLC system.

Over the past decade, many different receivers have been used in VLC systems. These receivers include PIN photodiodes, APDs, and now, Silicon Photomultipliers (SiPMs) are drawing a lot of attention. The following sections will discuss receivers which have been used in VLC systems, and provide a brief overview of each type of receiver.

PIN Photodiodes

PIN diodes are the lowest cost, most mature, and most widely used photo-detector. PIN diodes are used in many applications, including fibre optic communications, and optical sensing. When used in fibre optic communications, PIN diodes are used to convert the optical signal into an electrical signal. In this application, PIN diodes are able to benefit from the high optical power density of the optical fibre.

Avalanche Photodiodes

Avalanche photodiodes (APDs) are a type of photodiode which exploit avalanche multiplication to achieve a higher gain than a PIN photodiode. APDs are used in many applications, including fibre optic communications, and optical sensing. Importantly, APDs are able to achieve a gain of approximately 1×10^6 [13], which is significantly higher than PIN photodiodes. This high gain means that APDs are able to achieve a higher sensitivity than PIN photodiodes, and are able to detect individual photons.

Single Photon Avalanche Detectors

Single photon avalanche detectors (SPADs) are a type of avalanche photodiode which are able to detect individual photons. Because SPADs are able to detect individual photons, they are able to achieve a higher sensitivity than APDs. As a result, SPADs are used in many applications where single photon detection is required, including time of flight (ToF) sensing, and medical imaging. SPADs are able to achieve a higher gain than APDs, which means that SPADs are able to achieve a higher sensitivity than APDs [13].

The material used to make SPADs is typically silicon, as silicon is inexpensive, and has a high quantum efficiency. However, silicon SPADs are limited to the visible spectrum, as silicon has a band gap of 1.1 eV, which corresponds to a wavelength of 1100 nm. This means that silicon SPADs are not suitable for applications which require a wavelength outside of the visible spectrum. SPADs which are enhanced for specific wavelength ranges can be made by using different materials, such as InGaAs, and by controlling the doping profile of the SPAD.

There are two main types of SPADs, active quenching SPADs, and passive quenching SPADs. Active quenching SPADs use active circuitry to arrest the avalanche, and reset the SPAD. Passive quenching SPADs rely on the resistance to quench the avalanche, and reset the SPAD.

As a consequence, the variety of SPADs available is large, and the performance between different SPADs varies greatly. This is in contrast to PIN photodiodes, which are all very similar, and have similar performance.

Silicon Photomultipliers

Silicon photomultipliers (SiPMs) are arrays of SPADs, which are able to achieve a gain of approximately 1×10^6 [13]. SiPMs are used in many applications, including time of flight (ToF) sensing, and medical imaging. SiPMs are able to achieve a higher gain than APDs, which means that

SiPMs are able to achieve a higher sensitivity than APDs.

1.4   Importance of Receivers

A crucial component in every communications link is the receiver, and many different receivers have been used. In practical indoor VLC system deployment, the maximum permitted optical power for a transmitter is limited by eye safety limits, the indoor illumination regulation and also the comfort of users [14]. This results in the receiver's sensitivity as the determining factor in the VLC system's maximum achievable data rate and/or transmission distance. As the optical signal is dispersed throughout space, free space VLC systems typically require highly sensitive photo-detectors. Sensitivity is measured by the minimum usable optical power required to achieve a given bit error rate (BER) [15]. Free space VLC is a challenging environment for receivers, as the optical power density is low, and the receiver must have a wide field of view (FOV) to support mobility.

The simplest method to detect light, a p-n junction, will generate an electron hole pair in the depletion region for each detected photon. As a photon must strike the depletion region to be detected, the sensitivity of p-n diodes is poor due to the depletion region being relatively thin, p-n junctions also have a large capacitance and so are limited in bandwidth. Consequently, PIN photodiodes are preferred, as their thicker depletion region means a lower capacitance per unit area. These PIN photodiodes achieve a higher sensitivity than a p-n junction through having a thicker depletion region by using their p-doped - intrinsic - n-doped structure. PIN diodes are aggressively low cost devices due to their wide range of applications, mature manufacturing techniques, simple structure and ease of manufacture. As a consequence, they have been considered as a potential mobile phone receiver [16] and have practically found their way into open source VLC systems such as RONJA [17]. Despite having a higher sensitivity than a p-n junction, PIN photodiodes are still limited

by no gain (only one electron-hole pair is generated for each photon). When small (such as use cases of coupling to a single mode optical fibre with a 16 μm$\times$16μm detection surface) these devices have a generally high bandwidth (above 50 GHz) and as a consequence can achieve data rates above 10 Gbps [18, 19]. The optical fibre constrains the light to a small area, which means the optical power density is high, and consequently the sensitivity of the device is not a limiting factor. For the case of free-space VLC, the detection area must be far larger to increase the sensitivity of the device, which consequently results in a decreased bandwidth. Larger PIN diodes such as the SGH203 with 1 mm^2 detection area being around 100 MHz [17]. This is a significant limitation, as the bandwidth of the receiver limits the maximum data rate of the system.

The most sensitive detectors are all single-photon detectors. APDs are one such example, and offer benefits in their high gain due to photons causing avalanche multiplication which significantly amplifies the optical signal [20]. APDs are biased just below their breakdown voltage, and incident photons are absorbed by the depletion region, generating an electron-hole pair. The generated electron or hole is then accelerated by the strong electric field over the multiplication region. The electrons or holes gain enough energy to themselves create an electron hole pair. Consequently, each detected photon can result in the generation of multiple e-h pairs, and hence providing a gain from the single absorbed photon. Unfortunately avalanche breakdown is a random process which causes the generation of gain-dependant excess noise, which limits the maximum useful APD gain. As a result, there is an optimal APD gain to achieve the highest signal to noise ratio (SNR). The optimal SNR limits the avalanche gain that can be achieved, typically to less than 100 [15].

This limitation in gain can be avoided by biasing the APD above its breakdown voltage, which causes the APD to undergo a self-sustaining avalanche. This process of avalanche multiplication increases the APD

gain to approximately 1×10^6 [13]. APDs operating in this mode are often known as Geiger-Mode APDs (GM-APD), and are able to detect individual photons. When combined with circuitry to quench the avalanche and reset the device after a detection, the combination is referred to as a SPAD.

Previous work has shown success by replacing APDs with SPADs to achieve higherperforming VLC links [20]. The The quenching circuit used was passive, consisting of a resistor, and demonstrated a measurable improvement in the noise performance [2]. As SPADs can avalanche on a single photon, they have been demonstrated to have a higher sensitivity than APDs, with an early example showing a SPAD requiring 33 times fewer photons than an APD to achieve the same BER [15].

A feature of SPADs is that they must recharge after detection of a photon. Figure 1.1 outlines the mechanism of how a single passively quenched SPAD avalanches, quenches, and then recharges, ready to detect another photon. On detection of a photon the SPAD avalanches, outputting a measurable avalanche current. This avalanche current causes the bias over the avalanche diode to decrease, as some of the voltage is dropped over a quenching resistor, which rapidly halts the avalanche. The SPAD then recharges until the entire bias voltage drops over it. During the time taken to recharge the SPAD (which is known as the 'dead' or 'recovery' time), it has a reduced ability to detect a photon. Once fully recharged, a SPAD is ready to detect another photon with maximum sensitivity and repeat the process. This means a SPAD is heavily limited in the rate of photon detection due to the process of recovering after detection of a photon.

1.5 Silicon Photomultipliers (SiPMs)

Traditionally, photomultiplier tubes (PMTs) were used to sense low-light signals at the single photon level, yet due to their size, cost and fragility PMTs have limited application in VLC systems. SiPMs have
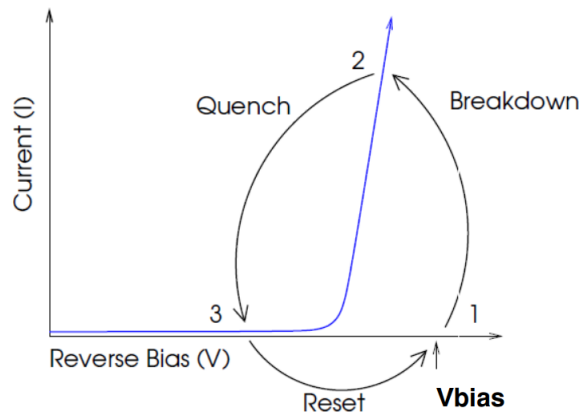
Figure 1.1: A diagram illustrating how a single SPAD (microcell) avalanches, quenches, and recharges. [21]

been developed as a solid-state alternative to replace PMTs, primarily in sensing applications (such as time of flight for LIDAR), but may also work as an inexpensive, more durable receiver for optical communications [22]. SiPMs are an array of SPADs which in this context are called microcells. Having many microcells offers the ability to detect photons despite some of the microcells recharging, which means SiPMs have a higher maximum count rate than PMTs. SiPMs were used by Oxford in previous work on receivers, and achieves the title as the world's most sensitive photo-detector in VLC [15, 2, 23]. This was shown through a SiPM achieving results close to the Poisson limit which is the number of photons required by Poisson statistics to ensure a bit error rate below the forward error correction (FEC) limit [2, 23].

SiPMs are large arrays consisting of thousands of microcells, and are preferred as receivers as the large number of detectors allows for a higher maximum count rate, remedying the recovery time problem of small groups of SPADs [13] [24]. Figure 1.2 shows an electrical diagram of the SiPM as produced by Onsemi, highlighting what a microcell is, and distinguishing it from a SPAD (Geiger-Mode APD (GM-APD)). Commercially available SiPMs which use this circuit include devices manufactured by Onsemi, of which an example is shown in figure 1.3. Inspection of the top of the detector shows many microcells making a large array.

The combination of exploiting avalanche multiplication to create internal gain, its large area, high bandwidth, and high number of microcells means the lowest irradiances for VLC have been reported in literature with SiPMs [2, 25].

SiPMs have many non-ideal behaviours, the most important of which are described here, with additional detail for each in section 2.2.

Dark Counts Microcells inside the SiPM frequently avalanche, due to thermally generated electron hole pairs. These avalanches, called 'dark counts', occur even when no light strikes the SiPM, and cannot be differentiated from photons being detected.

After Pulsing After a microcell avalanches, the cell may avalanche again while it is recharging. This additional detection pulse, called an 'after pulse' is indistinguishable from a photon being detected.

Cross Talk Microcells adjacent to a microcell which is undergoing an avalanche may also avalanche, despite not detecting a photon. The stimulated avalanche is caused by the high rate of change of the electric field within the adjacent avalanching microcell. This additional detection cannot be distinguished from another photon being detected.

Saturation SiPMs saturate under sufficiently high irradiances. This behaviour, caused by the small but finite recharge time of the microcells, limits the maximum detection rate of the SiPM.

Output Pulse Width Output pulses from any SiPM will have a small but finite pulse width. This limitation sets a limit on the bandwidth of SiPMs.

These non-ideal behaviours place limitations on the performance of SiPMs. In any communications system, the SNR of a link determines the BER. Should a SiPM be used as a VLC receiver, dark counts, after pulsing and

crosstalk will introduce additional noise, which will degrade the SNR, and consequently must be considered.

Despite these non ideal behaviours, impressive results have been achieved. Using incident powers of 10 nW (-50 dBm) data rates greater than 420 Mbps have been achieved with error rates lower than 10^{-3} [26, 23]. This makes SiPM orders of magnitude more sensitive than receivers that use PIN photodiodes, and even state of the art APDs. Importantly the maximum data rate achievable by a system depends on the SNR at the receiver's output and the system's bandwidth [27, 28]. SiPMs are equipped with the ability to achieve a high SNR through a high gain at a sufficient bandwidth to enable gigabit per second class communications [29].
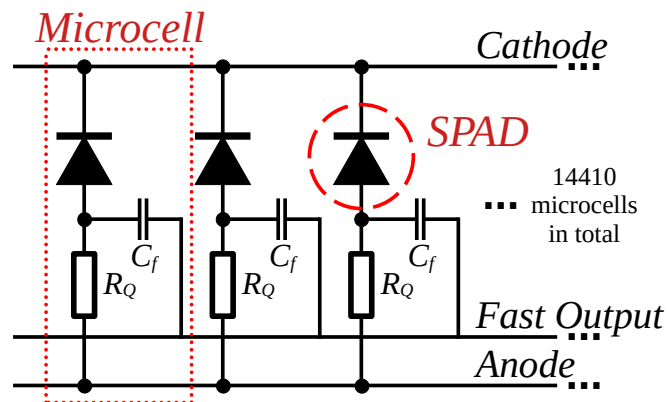
Figure 1.2: A circuit diagram of SiPMs as produced by Onsemi. In this case, a J-Series 30020 is shown as it has 14410 microcells.

The SiPMs used in this thesis are all manufactured by Onsemi, which uniquely has a *fast output*, shown on figure 1.2. This fast output is an electrical output from the SiPM which is capacitatively coupled to each individual microcell. Onsemi SiPMs are also made using through silicon vias (TSV) to create a sensor with minimal dead space, maximising the photon detection probability.

SiPMs are biased above their breakdown voltage V_{br}, which is when
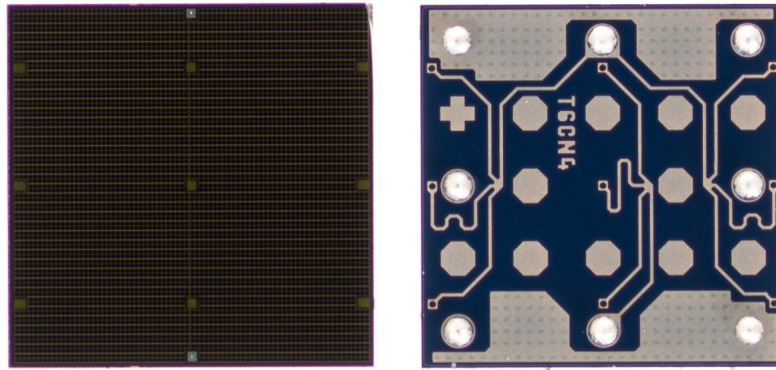
Figure 1.3: A photograph of a commercially available J-30035 SiPM as a surface mount technology (SMT) ball grid array (BGA) package. Left is the top face of the detector, right is the bottom face. [30]

microcells undergo avalanche photomultiplication. This bias above the breakdown voltage is referred to as an overvoltage ($V_{over} = V_{bias} - V_{br}$). On detection of a photon by a microcell, the SPAD undergoes avalanche multiplication, which creates an output pulse and causes current to flow through the SiPM. Once current flows through the microcell and hence the series microcell resistor, the bias voltage for that single microcell is decreased below the breakdown voltage, halting the avalanche, and allowing the device to recharge.

For the J-Series 30035 SiPM, measuring the response of an avalanche through a sense resistor on the cathode yields a FWHM pulse time of 50 ns. When the fast output is used the pulse FWHM time reduces to 1.5 ns, reducing the impact of inter-symbol interference (ISI) from the SiPM, and allowing the data rate to be increased by a factor of more than 30 before ISI occurs.

To achieve a VLC link, careful consideration must be given to the wavelength of light used. Colleagues in the field have previously used 405 nm as a transmitter wavelength, as 405 nm lasers are mass produced for Blu-Ray players [2, 12]. The mass production of these lasers means they are inexpensive, and have a high bandwidth. This choice is primarily driven by the lack of overlap with the emission spectrum of typical WLED domestic luminaries [2]. This characteristic helps reduce

the irradiance of ambient light after filtering. Additionally, the selection of J-Series of SiPMs is based on its peak photon detection efficiency at 405 nm, and its superior performance in terms of a shorter recharge time compared to Onsemi's C-Series SiPMs [31].

Within Onsemi's J series SiPMs there are several options which trade area for bandwidth. The naming scheme used by Onsemi to identify each model of their SiPMs is 'D00PP', where D is the square diameter of the SiPM in millimeters, and P is the pitch of the microcells in micrometers. J-60035 SiPMs are 6 mm square devices, which have a fast output pulse width of 3.0 ns [30]. Additionally, J-30035 and J-30020 SiPMs are also available, which are 3 mm square devices with output pulse widths of 1.5 ns and 1.4 ns respectively [30, 21]. J-60035 SiPMs have larger area, which importantly means that a lower transmitter irradiance is required to support a link. However the larger area on the J-60035 also means a greater capacitance is present on the output, which halves the bandwidth of the device. Previously, focus has been given to the J-30035 SiPM which achieved world record data rates, and set world records in eye-safe irradiance requirements at Gigabit/s speeds [2]. J-30020 SiPMs have also recently became available, and its differences to the J-30035 SiPM requires investigation to determine the consequences for VLC links.

1.6 Comparison to other Receivers

Among receivers based on APDs and PIN photodiodes, APDs built with BiCMOS technology have been reported to be the most sensitive receivers. 3 mm PIN diodes have supported VLC links at 500 Mbps, and 320 Mbps, but required optical powers of -10.5 dBm and 7.8 dBm respectively [32, 33]. This converts into irradiances of 12.6 Wm^{-2} and 852 Wm^{-2} which are prohibitively high irradiances for free space VLC. PIN diodes are typically used for fibre communications, where the optical power density is high due to all the light being constrained within the fibre. Although PIN diodes are able to achieve bandwidths as high as 40 GHz,

they are not suitable for VLC [34].

For links with a data rate of 2 Gbps, two examples of APD BiCMOS receivers were able to support links with a bit error rate of 10^{-3}. These APDs had diameters of 800 μm and 200 μm, and required irradiances of 0.56 Wm^{-2} , and 4.8 Wm^{-2} [35, 36]. Correcting for area, the coupled optical powers were -35.5 dBm, and -38.2 dBm respectively. The higher sensitivity of APDs means that significantly lower irradiances are required than by PIN diodes, and may allow for practical VLC to be performed.

By way of comparison, SiPMs have also been investigated as sensitive VLC receivers [2, 13, 37, 38, 12, 39, 40, 25, 26, 41]. At 2 Gbps, the same data rate used for the above APD studies, a study showed it was possible to use an Onsemi J-30035 SiPM (a square with diameter of 3.12 mm), to support an identical link with an irradiance of 11.5 mWm^{-2} [2]. The coupled optical power for this system was -39.6 dBm, which is a dramatic improvement over the irradiance required by APDs as VLC receivers.

This trend is continued at 2.5 Gbps, where SiPMs again dethrone APDs as the most sensitive receivers, and require a factor of 63 times less irradiance to support a link at a particular datarate and error rate [2]. The most important consequence of this study was showing that SiPMs, due to their larger area, operate with a much lower irradiance. Sensitivity to transmitter irradiance is vital to creating practical VLC links, as it is the quantity limited by eye safety requirements.

At lower data rates, where inter symbol interference has less of an impact, SiPMs have again a considerable lead in sensitivity over APDs. An Onsemi J-30035 SiPM was able to achieve a 1 Gbps with an optical power of -49 dBm (1.34 mWm^{-2}), which is barely above the physical limit in photons required to make the link possible [2]. To contrast this with APDs, the same 800 μm and 200 μm APDs as discussed above

required optical powers of -40 dBm and -38.8 dBm (3.6 Wm^{-2} and 281
mWm^{-2}) [35, 36].

In summary, the best state of the art APDs require irradiances 200
times higher than SiPMs when not limited by inter-symbol interference,
and 48 times higher at 2 Gbps. For all data rates from 400 Mbps to 2.5
Gbps, SiPMs have required lower irradiances than their APD counter-
parts. This key result highlights that for the task of VLC, SiPM based re-
ceivers are significantly better when contrasted to APDs and PIN diodes.

1.7   Poisson Statistics with VLC under ambi-

ent illumination

Since SiPMs have the ability to detect individual photons, they can
be used as optical receivers whose performance is limited by Poisson
statistics. The performance of an optical link depends on the number
of photons detected within a bit period, which depends on the PDE, the
device area, and the transmitter and interference irradiance. The BER of
an optical link is determined by the number of detected signal photons
per bit n_s in the presence of n_a detected ambient photons per bit, with a
decision threshold of n_T photons per bit. The expression for the BER is
calculated using [23]

$$
\text{BER} = \frac{1}{2} \left[\underbrace{\sum_{k=0}^{n_T} \frac{(n_a + n_s)^k}{k!} e^{-(n_s+n_b)}}_{\text{Tx'd 1 detected as 0}} + \underbrace{\sum_{k=n_T}^{\infty} \frac{n_a^k}{k!} e^{-n_a}}_{\text{Tx'd 0 detected as 1}} \right] \tag{1.1}
$$

Using this BER formula a numerical search was performed to find the
required transmitter power to support a BER of $3.8 \cdot 10^{-3}$. Figure 1.4
shows the required detected photons per bit from the transmitter as a
function of the interference photons per bit.

When considering the background detected photons per bit, the re-
quired signal detected photons per bit initially sits approximately flat at
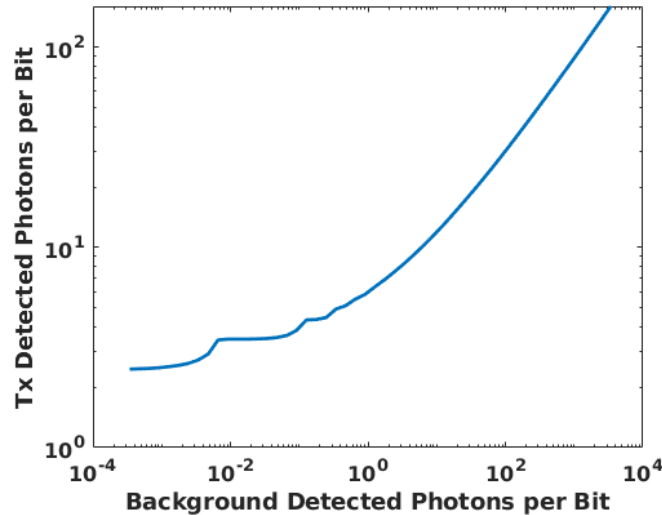
Figure 1.4: Required detected signal photons per bit-time vs background detected photons per bit-time, to support a BER of $3.8 \cdot 10^{-3}$.

background photons per bit less than 10^{-2}. The model then predicts steps in the required number of signal photons per bit, as the background increases. This is due to the Poisson distribution being discrete, and the decision threshold for a bit one or zero only being able to sit at discrete points in the distribution. The flat 'shelf' sets a hard limit on the minimum number of photons per bit required to maintain an optical wireless link [2], however as more interference photons per bit are detected the required detected signal photons per bit line trends to a power law of $L_{background}^{0.5}$.

1.7.1   Impact of Transmitter Extinction Ratio

The previous section shows that to accurately predict the required signal irradiance at a SiPM based receiver, the background irradiance must be known. The transmitter itself may introduce background irradiance, as the extinction ratio (EXR) of the transmitter means there will be an optical DC component. Transmitters require a wide bandwidth to support data rates of several Gbps. For some lasers, this means that when transmitting a zero, the transmitted light becomes dimmer, rather than turning completely off. This is unavoidable as when modulating a laser, it is biased to an operating point within its lasing regime. Leaving, and then re-entering this lasing regime requires time for population inver-

sion to reoccur, and to begin to lase again. The time required to achieve population inversion limits the bandwidth of the transmitter.

The ratio between transmitters' output powers when transmitting a zero, P_0, and when transmitting a one, P_1, is hence characterised by the EXR:

$$EXR = \frac{P1}{P0} \tag{1.2}$$

Using equation (1.1), it is possible to calculate the required number of signal photons per bit as a consequence of the extinction ratio. The results in figure 1.5 show that the EXR can have a significant impact on the number of photons per bit needed to achieve a particular BER. Previously, the EXR of a L405P20 405 nm laser diode used to transmit OOK data rates of less than 2.4 Gbps was found to be 15 [42]. The impact of this EXR had to be taken into account when predicting the performance of a system accurately [2]. However, at lower extinction ratios, for example those less than five, the number of photons per bit increases very rapidly as the EXR reduces. The EXR of a transmitter could therefore play a key role in determining the performance of a system.
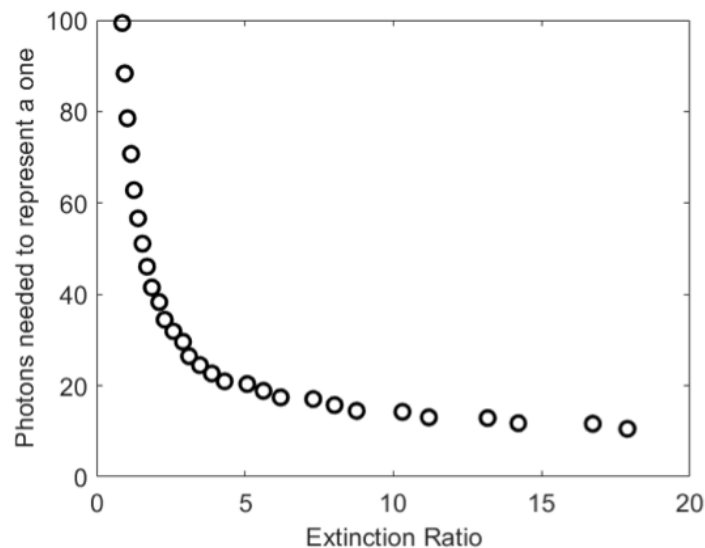
Figure 1.5: The impact of the extinction ratio of the transmitter on the number of photons per bit required to represent a one, and achieve a BER of 3.8×10^{-3} [43].

1.7.2 Forward Error Correction

The previous section shows that the number of photons per bit required to achieve a particular BER is dependent on the background irradiance, and the extinction ratio of the transmitter. However, the number of photons per bit required to achieve a particular BER is also dependent on the FEC code used. FEC codes are used to correct bit errors, and are able to correct a certain number of bit errors per bit. The number of bit errors that can be corrected per bit is referred to as the code's Hamming distance.

The existence of a range of FEC codes [44] means that the performance of VLC systems have previously been reported at a range of BERs including 10^{-3} [45], $2 \cdot 10^{-3}$ [46] and $3.8 \cdot 10^{-3}$ [47, 48]. Of these one of the most popularly reported BERs is the 7% limit for FEC, which is a BER of $3.8 \cdot 10^{-3}$ [44].

In this thesis, different FEC limits are used to compare the performance of different systems, as the FEC limit is a key parameter in determining the performance of a system.

1.8 Thesis Scope and Significance

The main aim of this thesis was to develop visible light communications receivers to create inexpensive, robust communication links to augment existing Wi-Fi infrastructure to handheld devices. Exploiting low power transmitters by using SiPMs is a way to achieving this goal. However the impact of ambient light, and effectively mitigating its impact need to be understood to create practical, eye-safe links. This thesis explores the operation of SiPMs, and develops the understanding of the impact of microcell recovery time on VLC links.

This thesis also selects a suitable Onsemi SiPM as a VLC receiver, as well as making the SiPM's operation in a VLC link robust without restricting the FOV of the system. To achieve this, work in this thesis char-

acterises and compares a SiPM which was used in literature with a new SiPM. During studies toward making the VLC link robust, a newly discovered form of ISI present on SiPMs is presented and investigated.

For realistic deployed links, ambient light will be present and is not completely avoidable. The impact of ambient light is investigated, and the circuitry associated with some SiPM evaluation boards is shown to have a performance detriment. The detection area of SiPMs is an important parameter for device operation, and hence combining multiple SiPMs to increase device area while maintaining the same bandwidth is also investigated to achieve the aim of a more sensitive practical VLC receiver. To use the SiPM a suitable VLC receiver, key understanding is also needed on how individual microcells operate. Numerically modelling the SiPM allows for a better understanding of how individual microcells operate. This sets the scene for the development of a SiPM-specific equaliser, and also designing SiPMs specifically for VLC and predicting their performance in different environments.

Ambient light is not the only form of interference that receivers experience. In particular, to maintain coverage and quality of service, the receiver needs a wide field of view, and transmitters must overlap. Hence sometimes two or more transmitters will be within the receiver's field of view, and will have comparable irradiances. If the transmitters have the same wavelength, this is a far bigger challenge than ambient light, as a SiPM by itself has no way of discriminating which photons come from which transmitter. The thesis concludes with presenting a novel method which solves the problem of transmitter selection, and rejecting ambient interference, which in the future may allow for operation of SiPMs in daylight.

1.9 Thesis Contribution and Structure

The outline of this thesis is as follows:

Chapter 2 contains the theory of operation of SiPMs, and the non-

ideal behaviours which limit their performance. This chapter introduces key SiPM behaviours and parameters which are used throughout the thesis.

Chapter 3 contains initial characterisation work performed on a newly identified SiPM which has a higher maximum count rate than the previous SiPM which achieved a world record data rate. This chapter compares the two SiPMs to determine which is suitable for a VLC system through comparing dynamic range and achievable data rates. Conclusions are made about the selection of future SiPMs. The work in this chapter was published in [37, 38].

Chapter 4 investigates the impact of ambient light on SiPM receivers in VLC links, and shows a direction towards operation in daylight. High incident irradiances are known to cause saturation of the SiPM, which have consequences on VLC links.

Chapter 4 also discusses an unusual eye diagram shape which occurs when the SiPM is exposed to high levels of ambient light. This is presented as a new form of inter symbol interference (ISI) which originates in the nonlinear response of the SiPM at high irradiances. This new form of ISI is investigated and methods of correcting it using conventional equalisation are explored. The work in this chapter was published in [23, 12, 49, 50]

Chapter 5 contains a numerical model of the SiPM, the simulated device is shown to replicate observations made throughout this report. This developed capability hence allows further insight into the SiPM's operation, explaining why the effective PDE of SiPMs roll off at a higher rate than initially expected. The work in this chapter was published in [51, 43].

Chapter 6 presents and explores a newly designed optical system which allows for ambient light to be attenuated, and addresses the problem of the selecting a single transmitters when multiple are within the

field of view.

Chapter 7 concludes the report with discussions about the performed experiments and shows a potential road-map for future work in the field.

Chapter 2

SiPM Theory of Operation

2.1   Overview

This chapter begins with an introduction to the operation of passively quenched SiPMs. Important terminology for SiPMs is introduced, which is important for understanding the mechanisms at work inside SiPMs.

2.2   Theory of Operation & Terminology

2.2.1   SiPM Working Principle

SiPMs (Silicon Photomultipliers) are solid-state photo-detectors that operate based on the principle of Single Photon Avalanche Diodes (SPADs). SiPMs consist of an array of small, individual silicon microcells connected in parallel, each capable of detecting single photons.

The microcells are reverse-biased PN junctions, which are formed by doping a thin layer of silicon with impurities. A bias voltage, typically in the range of tens of volts, is applied across the microcell. This voltage is above the breakdown voltage to create a strong electric field within the microcell. When a photon enters a microcell and interacts with the silicon, it generates electron-hole pairs. These electron-hole pairs are created with low energy and cannot trigger the avalanche multiplication process. If the generated electron or hole reaches one of the microcells' depletion regions and gains enough energy, it triggers an avalanche. The

electric field accelerates the carrier, leading to collision ionisation with other atoms. This collision creates additional electron-hole pairs, resulting in a chain reaction of avalanche multiplication.

During the avalanche process, the microcell experiences a rapid increase in the number of electron-hole pairs and a corresponding increase in the current flowing through the microcell. This gain means that the microcell can detect single photons, which would otherwise be undetectable.

To quickly quench the avalanche process and prepare the microcell for the detection of subsequent photons, a quenching circuit is activated. The quenching circuitry over a matter of picoseconds lowers the voltage across the microcell, suppressing further multiplication and preventing a continuous discharge. SiPMs which have microcells utilising active circuitry to achieve this are referred to as *actively quenched*. However the majority of commercially available SiPMs use the avalanche current flowing through a resistor to reduce the bias voltage over the silicon junction and quench the avalanche, and are known as *passively quenched*.

After quenching, the microcell recharges and is ready for the detection of another photon. Readout circuitry inside the microcells may be present to generate output pulses, and the bias current required to sustain the bias voltage may also be measured to detect individual photons. In J-Series devices by Onsemi, small capacitors are used to couple the microcell to a common readout line. This output, known as the 'fast output' was one of the key reasons why Onsemi J-Series devices where chosen for this work, as competitors such as SensL do not offer this feature. Output pulses on the fast output have a low full width half max time (FWHM), which in turn leads to a lower DFE power penalty at high data rates, as ISI occurs at a higher data rate [2].

The SiPM is a large array of microcells, which are connected in parallel. The operation of the SiPM is the same as a single microcell, however,

the output signal is the sum of the output signals of all the microcells. This means that the SiPM can detect multiple photons simultaneously, and the output signal is proportional to the number of photons detected. The output signal of the SiPM is typically amplified and shaped by external circuitry, and the resulting signal can be digitised and processed by a microcontroller or FPGA.

2.2.2 Bias Voltage and Overvoltage

The breakdown voltage is an important parameter for SiPM operation because it determines the voltage at which the avalanche multiplication process occurs. When the applied voltage across the SiPM (V_{bias}) exceeds the breakdown voltage ($V_{breakdown}$), the electric field within the silicon becomes sufficiently high to trigger electron avalanches. These avalanches generate a significant number of electron-hole pairs, leading to a rapid amplification of the signal, and a detectable output pulse.

The breakdown voltage is typically specified by the PN junction doping concentration, and can vary depending on the specific design and fabrication process. It is crucial to operate the SiPM within the specified voltage range to ensure optimal performance, and avoid damaging the device.

A useful definition when considering SiPM biasing is overvoltage, V_{over} which is defined as the bias voltage over the breakdown voltage ($V_{bias} - V_{breakdown}$). Some benefits of increasing the bias voltage include an increased output pulse amplitude as there is more charge per microcell, and the Photon Detection Efficiency (PDE) is also shown to increase with bias voltage [30].

Both data sheet values and experimental results show that the PDE gradually approaches an asymptotic value [2], which would suggest using the highest possible bias voltage. A consequence of using a high bias voltage is the increased probability that a thermally generated electron-hole pair will create an avalanche event, known as a dark count, or false

detection. The resulting dark counts contribute to the number of background counts per bit and they can, therefore, cause an increase in the number of signal counts per bit. Another risk of increasing the bias voltage is the increased amount of power sunk by the SiPM, which may cause permanent damage.

2.2.3 Photon Detection Efficiency (PDE)

Photon detection efficiency (PDE) quantifies the likelihood of a SiPM successfully detecting a photon. This important metric offers insight into how effectively the SiPM transforms incident light into an electrical signal, with a higher PDE meaning the SiPM is more sensitive to light. The PDE is contingent upon several factors, including the wavelength of the incident light, the design characteristics of the microcells, the bias voltage, and the fill factor, which represents the active area of the SiPM divided by its total area. Generally, SiPMs exhibit PDEs ranging from 20% to 50% [21].

Notably the wavelength at which the peak PDE is achieved depends on the width of the depletion region within the reverse-biased microcell. Manufacturers can strategically adjust this width to target different wavelengths. Figure 2.1 illustrates the wavelength-dependent variation in PDE for an OnSemi J-Series SiPM, with a peak in its PDE at 420 nm.

2.2.4 Dark Count Rate

In SiPMs, the primary mechanism responsible for dark counts is thermal excitation of charge carriers within the silicon. At room temperature, electrons can be thermally excited from the valence band to the conduction band, creating electron-hole pairs. If one of these electrons or holes happens to be near the depletion region of the SiPM, it can trigger an avalanche breakdown, leading to a dark count event. Consequently, dark count rates primarily depend on the overvoltage, and the temperature of the SiPM [30]. The overall design of the SiPM will also affect the dark count rate. For SiPMs, the dark count rate is linearly proportional
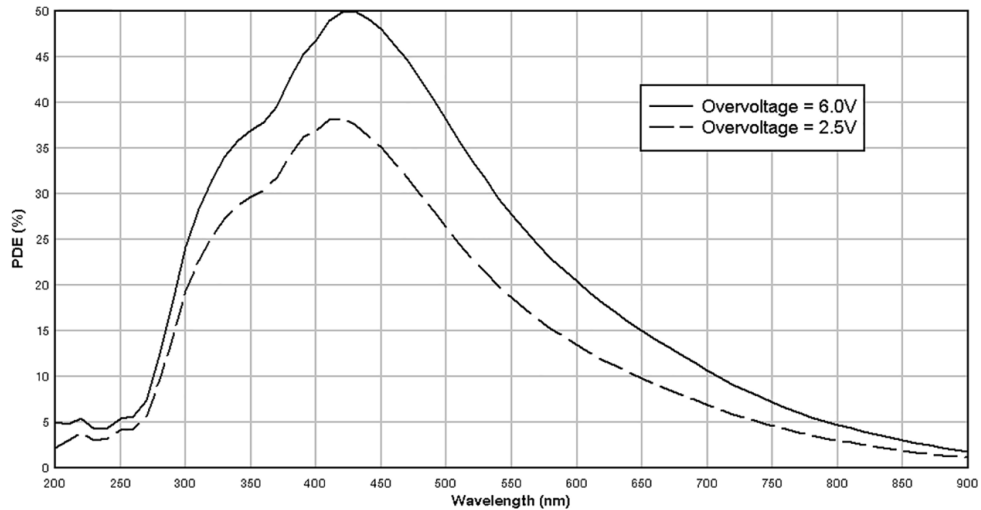
Figure 2.1: J-Series SiPM photon detection efficiency as a function of wavelength. [30]

to the area, and the implementation of the microcell will change the likelihood of a dark count event occurring. The sum of the charges liberated during dark count events generates the 'dark current' of a SiPM.

Dark count, much like photon counts, occur randomly in time. This means that the time intervals between successive dark count arrivals are exponentially distributed in time. When considered over a long period of time, the number of dark counts observed follows a Poisson distribution.

This is a fundamental characteristic of Shot Noise.

The presence of dark counts is undesirable in applications such as VLC because they introduce shot noise into the detection process. When trying to detect and decode optical signals, these false positives can be misinterpreted as valid data, leading to errors in communication. In VLC systems, especially those aiming for high data rates and precision, minimising dark counts is crucial to achieving reliable and accurate data transmission.

The BER of a VLC link, as a consequence of 'background' photons, and signal photons per bit was described in section 1.7. Dark counts directly contribute to the quantity of 'background' photons observed, and hence degrade the SNR of the optical link.

In Onsemi J-Series SiPMs, the dark count rate is 50 kHz mm^{-2} [30]. This means that at 1 Gbps, 0.05% of the bits contain dark count events. When this dark count rate is present figure 1.4 shows the impact on the required number of photons per bit to maintain a target BER is fortunately negligible.

2.2.5 Crosstalk

Crosstalk is a phenomenon where the detection of a photon in one microcell can lead to the unintended generation of secondary signals in neighbouring microcells. This effect can introduce noise, if the amount of crosstalk is sufficiently high. Crosstalk occurs due to several mechanisms, including:

Optical Crosstalk When a photon is absorbed in one microcell, it can generate secondary photons via processes such as scintillation or fluorescence. These secondary photons may escape the microcell and be detected by adjacent microcells, leading to additional avalanches.

Electronic Crosstalk Electronic crosstalk involves the spread of charge carriers, such as electrons and holes, generated by the primary photon detection. These carriers can diffuse or be guided to neighbouring microcells, causing those microcells to also produce signals. This can happen due to the proximity of microcells and the electric fields within the SiPM. To reduce the impact of electronic crosstalk, the microcells are typically separated by a small distance and may have guard rings to reduce the electric field strength.

Capacitive Crosstalk In some cases, charge carriers created by a primary photon detection can induce electrical charges in the electrode structures of neighbouring microcells through capacitive coupling. This induced charge can trigger the neighbouring microcells, leading to crosstalk.

Crosstalk events happen almost simultaneously to a regular detection (tens of picoseconds), giving rise to pulses with an amplitude a multiple of a single detection. Crosstalk in Onsemi J-Series SiPMs, is approximately 2%. For VLC, this crosstalk probability is low enough to neglect, as it does not increase the dark count rate enough to change the number of required photons per bit at 1 Gbps.

2.2.6 Passive Quenching Model

The majority of commercially available SiPMs are passively quenched due to the simplicity of the circuitry involved. To understand the operation of a single microcell, an equivalent circuit is shown in figure 2.2, developed by McIntyre and Haitz [52].

This equivalent circuit consists of a capacitor C_{cell}, a voltage source V_{br} (the breakdown voltage of the APD), and a series resistor R_S, which is the total resistance of undepleted regions in an APD [53]. R_S depends upon the bias applied to the microcell. When no bias is applied, R_S is typically on the order of several hundred ohms, however, when a bias voltage is applied to the SPAD, it reduces to tens of ohms. A bias voltage (V_{bias}) greater than V_{br} is applied, which allows the microcell to avalanche.

In the event when there is no photon incident or avalanche event occurring, the switch in the circuit model will remains open and the cell capacitance is charged to V_{bias}. The charging of the capacitance obeys a simple RC time constant expression, typical for a capacitor recharging.

When an avalanche event occurs, the switch in the equivalent circuit is closed, causing the microcell capacitance to discharge through R_S. The current flowing through the microcell, caused by the avalanche, also flows through a quenching resistor, R_Q. The current through R_Q causes the voltage over the microcell to decrease to V_{br}, and the switch to open, signifying the avalanche has been quenched. The microcell capacitance then proceeds to recharge back to the bias voltage, again obeying a simple RC time constant.
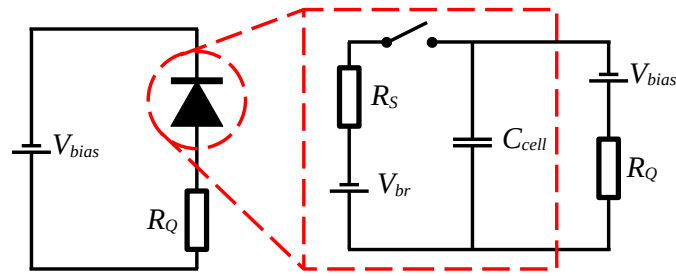
Figure 2.2: A circuit diagram of a single microcell (left), with circuitry giving a first order model of SPAD (right).

2.3 Saturation

SiPM saturation refers to the state where a SiPM reaches its operational limits in terms of photon detection rate, usually due to an excessive number of incoming photons within a given time window. In this state, multiple photons incident on the same micro-cell or different micro-cells may overlap, leading to a nonlinear response. This effect impacts the SiPM's ability to accurately count incident photons.

Before saturation, the I_{bias}-irradiance response of the SiPM is linear. As the irradiance increases, saturation is observed through the bias current asymptotically reaching a maximum value.

Chapter 3

Characterisation and Comparison of J-Series 30020 and 30035 SiPMs

3.1 Overview

This chapter shows a characterisation of Onsemi J-Series 30020 and 30035 SiPMs. Photon detection rate is discussed, and used as motivation for characterising the J-Series 30020 SiPM. Experiments are presented which determine the impact of bias voltage on the SiPM to find the optimal biasing conditions for a J-Series 30020 SiPM. This is followed by a comparison with a J-Series 30035 SiPM to determine which device is more suitable in a VLC system, and to draw conclusions about the selection of future devices.

Observations on the dynamic range and achievable data rates are made, showing the new J-Series 30020 provides the ability to support 405 nm VLC links at high data rates. This chapter proceeds to show the J-Series 30020 achieving a higher data rate as predicted, resulting in a new world-record data rate using SiPMs. Finally, the chapter suggests a utility function for SiPM selection in regimes where low irradiances are present.

3.2 Photon Detection Rate Modelling

The maximum photon detection rate, or count rate, of a SiPM is a factor in determining the irradiance required to support a data rate [37, 38]. The maximum achievable data rate is more strongly influenced by the recharge time and output pulse width, but requires a sufficiently high count rate. Recently, it was reported that despite saturation, when an Onsemi J-Series 30035 SiPM is used the maximum achievable on-off keying (OOK) data rate with a BER of 10^{-3} was 2.4 Gbits/s, which was a world-record data rate using SiPMs [2]. In this work, Ahmed's data rate was limited by the maximum count rate of the SiPM.

The count rate of a SiPM is modelled by [15] [41],

$$\beta = \frac{\eta A_{\text{SiPM}}}{E_p N_{\text{cells}}} \tag{3.1}$$

$$\frac{dD}{dt} = \frac{N_{\text{cells}}\beta(L + L_{\text{dark}})}{1 + \beta\tau_{\text{recharge}}(L + L_{\text{dark}})} \tag{3.2}$$

where $\frac{dD}{dt}$ is the detection rate, η is the photon detection efficiency, E_p is the photon energy, A_{SiPM} is the area of the SiPM, L is the light irradiance, τ_{recharge} being the characteristic recharge time of a single microcell and N_{cells} the number of microcells.

This model captures the effect of microcells recharging, and offers an explanation as to why the SiPM saturates. The count rate as a function of irradiance is especially important to VLC as it defines the maximum achievable data rate. This is because a minimum number of photons per bit are required to support a specific BER. The minimum number of photons per bit is defined through Poisson statistics, introduced in section 1.7. Increasing the maximum count rate would in turn increase the maximum achievable data rate of the SiPM.

In the work performed by Ahmed, the highest achieved data rates occurred at irradiances within the saturated region of the SiPM. Using the

paralysable SiPM count model in equation (3.2), if $\beta\tau_{\text{recharge}}(L + L_{\text{dark}}) >> 1$, then the count rate equation (3.2) of a SiPM simplifies to

$$\frac{dD}{dt} = \frac{N_{\text{cells}}\beta(L + L_{\text{dark}})}{\beta\tau_{\text{recharge}}(L + L_{\text{dark})}} = \frac{N_{\text{cells}}}{\tau_{\text{recharge}}} \tag{3.3}$$

3.2.1 SiPM Count Rate Comparison

Section 1.6 highlighted recent achievements with SiPMs in VLC systems. Specifically, an Onsemi J-Series 30035 SiPM was previously identified and characterised by Ahmed as a promising candidate for use in a VLC system [2]. The J-Series 30035 was then selected due to its high PDE and high fast output pulse rate, and fast output (yielding a smaller pulse width) [2]. which led to achieving a world-record data rate of 2.4 Gigabit/s using SiPMs [2]. The newly available J-Series 30020 SiPM was considered to be a challenger to beat the J-Series 30035's data rate record in a VLC channel. Both the J-Series 30020 and 30035's key device properties for achieving a high speed link were tabulated in table 3.1.

The significant difference between the two SiPMs is the microcell pitch, indicated by the last two digits of the part number measured in microns. By reducing the pitch the number of microcells increases and as the microcell size is smaller, the capacitance and recharge time constant decrease [30]. The gain of the microcell is directly proportional to the amount of charge in the microcell's capacitance. When compared to the J-30035, both the capacitance and the recharge time for a single microcell are three times lower for the J-30020, which corresponds directly to the ratio of the microcell areas. As the J-30020 has more microcells, a greater fraction of the device is used for spacing between active areas for circuitry, and hence the total active area of the J-30020 is lower than the J-30035. This is reflected by the PDE of the J-30020 being 76% of the J-30035's PDE.

In Ahmed's work with the J-30035 SiPM, the maximum count rate

was what hindered the achievable data rate, when a world-record data rate of 2.4 Gbps was achieved [2, 37]. The J-30020 SiPM with its greater number of microcells, was expected to have a higher count rate, and hence that a higher data rate could be achieved. Although the two devices are expected have very different output pulse rates when saturated, they both have very similar output pulse widths (table 3.1). It was therefore expected that any difference between their maximum data rates will therefore arise strictly from very different output pulse rates in saturation.

The maximum count (or detection) rate for a non-paralysable SiPM can be calculated by using the model in equation (3.2). If the incoming irradiance is sufficient such that $\beta\tau_{\mathrm{recharge}}(L + L_{\mathrm{dark}}) >> 1$, the count rate simplifies to

$$\frac{dC}{dt}_{\max} = \frac{N_{\mathrm{cells}}\beta(L + L_{\mathrm{dark}})}{\beta\tau_{\mathrm{recharge}}(L + L_{\mathrm{dark})}} = \frac{N_{\mathrm{cells}}}{\tau_{\mathrm{recharge}}} \tag{3.4}$$

The J-30035 SiPM has a predicted maximum pulse rate of 120×10^9 pulses/s. For the case of the 30020, the maximum output pulse rate is 7.6 times higher than the maximum pulse rate of the J-30035, at 960×10^9 pulses/s.

Table 3.1: Comparison of different properties of the J-30020 and the J-30035 SiPMs [30]

SiPM	J-30035	J-30020
Active Area	3.16x3.16 mm^2	3.16x3.16 mm^2
PDE +5V	0.38	0.5
Dark Count Rate +5V	125 kHz/mm^2	150 kHz/mm^2
Microcells	5,676	14,410
Recharge Time Constant	45 ns	15 ns
Pulse Width	1.5 ns	1.4 ns
Gain +2.5V	2.9 $\times 10^6$	1.0 $\times 10^6$

3.3 Breakdown Voltage Measurement, and Effect of Biasing on Count Rate

The maximum achievable count rate of a SiPM *limits* the maximum possible data rate. The bias voltage of the SiPM is a crucial parameter

as it impacts the performance of the device, including the PDE, and dark count rate. Since the maximum count rate depends upon recharge time, it also may depend upon the overvoltage. If this is the case, the maximum count rate will depend upon the overvoltage.

Experiments were performed to determine if changing the SiPM's bias voltage causes a change in maximum count rate. Since the maximum count rate of a SiPM is is high enough for output pulses to overlap, the SiPM no longer produces discrete Geiger mode pulses, so no photon counting can be performed [21]. The count rate of the SiPM must therefore be investigated through measuring how the bias current varies against bias voltage.

By assuming the bias current is proportional to the cell charge, which in turn is a function of the overvoltage of the SiPM, the following relationship was derived.

$$I_{\text{bias}} = \frac{dD}{dt} Q_{\text{cell}} \left(V_{\text{over}} \right) \tag{3.5}$$

Where $\frac{dD}{dt}$ is the count rate and Q_{cell} is the charge contained on a single microcell. $Q_{\text{cell}} \left(V_{\text{over}} \right)$ is assumed to be a microcell capacitance multiplied by the overvoltage $Q_{\text{cell}} \left(V_{\text{over}} \right) \approx k V_{\text{over}}$. The count rate estimate therefore becomes for some scaling constant k,

$$k \frac{dD}{dt} = \frac{I_{\text{bias}}}{V_{\text{over}}} \tag{3.6}$$

This is because the current is due to discharging the capacitance down to the breakdown voltage to quench the microcell, and hence the charge is CV_{over}. If more avalanches take place, a larger bias current would be observed. If the SiPM is illuminated with an irradiance in the saturation region, the PDE of the SiPM will have no impact, meaning the measurement of a higher bias current corresponds to a greater $k\frac{dC}{dt}$.

To accurately determine the breakdown voltage, the J-30020 SiPM was placed under a sufficiently high irradiance to saturate the device.

V_{bias} was varied from a programmable bench power supply and measured by a Keithley 175 digital multi-meter. The resulting bias current was measured using a Keithely 195A digital multi-meter. The results are shown in figure 3.1a, which shows the bias current increasing linearly with bias voltage when the bias voltage is above a breakdown voltage. These results are consistent with a SiPM undergoing breakdown, and are consistent with the Onsemi datasheet, which states the breakdown voltage is 24.5 V [30]. A linear fit was performed on all data points above 25 V, giving a fitted function:

$$I_{bias} = 11.10 \times V_{bias} - 273.3 \tag{3.7}$$

where I is measured in milliamps. The fit had an R^2 of 0.999, indicating the linear fit was reasonable. From the linear fit, the breakdown voltage was obtained by dividing the coefficients to find the intersect on the x axis, giving an estimate of the breakdown voltage as 24.63 V.

An experiment was then performed to determine if the maximum count rate (determined by the bias current) changes with bias voltage. V_{bias} was varied (above the breakdown voltage), and the irradiance falling upon the SiPM was also varied. To maintain a high accuracy, SiPM bias was measured with a Keithley 175 digital multi-meter to four figures of accuracy. Again, the resulting bias current was measured using a Keithley 195A digital multi-meter. The measured bias current was then corrected by using equation (3.6), and dividing by the overvoltage. To keep heating effects to a minimum, the SiPM was only turned on just before measurement, and switched off immediately after.

When V_{bias} is increased (as visible in figure 3.1a) the higher bias voltage causes the device to output a larger pulse amplitude for each measured photon, which causes an increase in bias current. The pulse amplitude (and therefore microcell charge) must be linear with respect to the overvoltage. Consequently, results in figure 3.1b suggest the *maximum*

count rate does not increase with SiPM bias voltage. There is no statis-

tically significant difference or in $k\frac{dD}{dt}$ as V_{bias} is increased, meaning that

given V_{bias} is sufficiently high there is no difference in maximum count
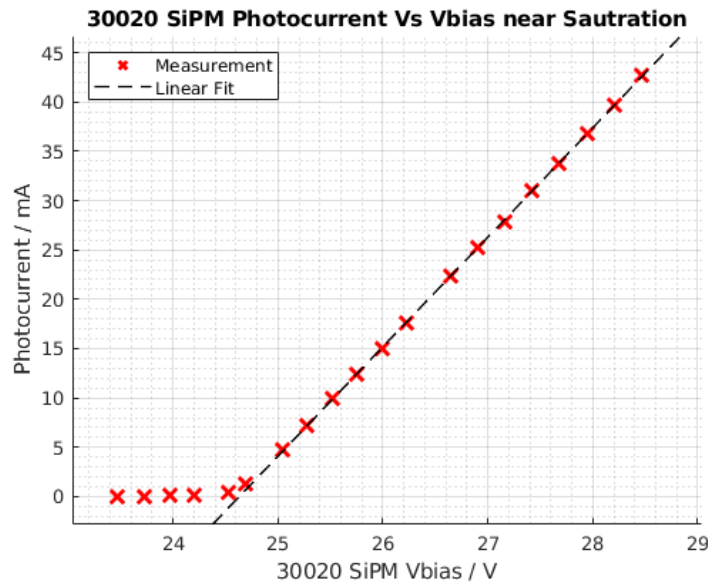
rate.

(a) J-30020 SiPM under an irradiance sufficient to saturate the device. Vbias is
varied and the bias current is observed.
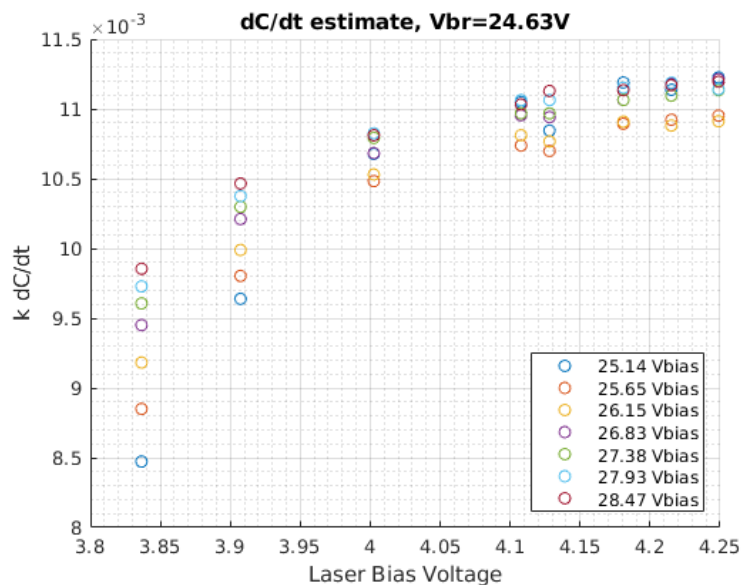
(b) J-30020 SiPM under varying light intensity near saturation. Vbias is varied
and no clear difference in count rate is observed.

Figure 3.1: Maximum count rate experimental results.

3.4   Measurement of DCR and Microcell Charge

The dark current of a SiPM is the resultant bias current from thermally induced avalanches, known as dark counts. This bias current was measured for a J-30020 SiPM against different bias voltages, to determine how the dark count rate changes with voltage. An oscilloscope (Keysight MSOV334A 33 GHz) was used to capture dark pulses, and the bias voltage of the SiPM was provided by a programmable benchtop power supply. The bias voltage was swept from 24 V to 30 V, which corresponds to overvoltages from -0.5 to 5.5 V. The bias current for each voltage was measured with a Keithley 195A digital multi-meter. Waveforms were then captured on the oscilloscope, and were processed to generate timestamps of individual pulses through calculating the prominence of each peak in the signal. The prominence of a peak is a measure of how much a peak 'stands out' due to its height and location relative to other peaks. A low peak in a totally flat signal can be more prominent than a higher peak, among other higher peaks. Prominence allows a method of noise rejection, as peaks emanating from white noise will have a low prominence. MATLAB's peak detection using prominence is performed using the `findpeaks` function.

Figure 3.2b shows the mean pulse amplitude as a function of the applied bias voltage. These results show the pulse amplitude increases proportionally with overvoltage which again demonstrates that microcell charge changes with bias voltage. A larger charge on a microcell improves the signal to noise ratio on the receiver's electrical circuit, which suggests higher bias voltages are preferred. However, the quadratic increase in the dark count rate means that eventually dark counts will introduce excess noise, and limit the sensitivity of the receiver. Although the pulses' mean amplitude was measured, an accurate count rate could not be obtained due to the noise floor being close to the amplitude of the pulses, causing many pulses to be not counted, especially at lower

bias voltages. A different method to determine the dark pulse rate was therefore needed.

Figure 3.2a shows the current resulting from dark counts as a function of the applied bias voltage. The bias current increases quadratically with bias voltage, which is explained by the rate of dark pulses increasing linearly with the bias voltage, and the amplitude of pulses also increasing linearly with bias voltage. The product of the pulse amplitude with the pulse rate results in the SiPM's bias current. These results are consistent with the Onsemi data-sheet, which quotes a typical dark currents of 0.1 μA with a 2.5 V overvoltage, and 0.45 μA at a 5 V overvoltage [30]. Onsemi's literature also describes a quadratic relationship between dark-count current and the bias voltage applied [21], which is consistent with measurements.

Finally, the charge and hence capacitance of a microcell can be estimated. At 2.5 V_{over}, the Onsemi datasheet states the J-30020 has a dark count rate of 50 kHz mm^{-2}. At this bias voltage, the bias current was measured to be 68 nA, meaning that for the 9.98 mm^2 package, the charge contained in a microcell is approximately 140 fC. Assuming the microcell's capacitance behaves linearly ($Q = CV$), the estimated capacitance per microcell is 56 fF. Similarly, at 5 V_{over}, the Onsemi datasheet states the J-30020 states a dark count rate of 125 kHz mm^{-2}. Following the same analysis, and using an interpolated value of the bias current of approximately 400 nA, the microcell charge was 320 fC, meaning the microcell capacitance is estimated to be 66 fF. These two measurements of the microcell capacitance are consistent within the measurement error of the experiment (10%). The limiting factor in the accuracy of the measurement is the dark count rate, which was provided by Onsemi's datasheet, and is only accurate to within 10%.
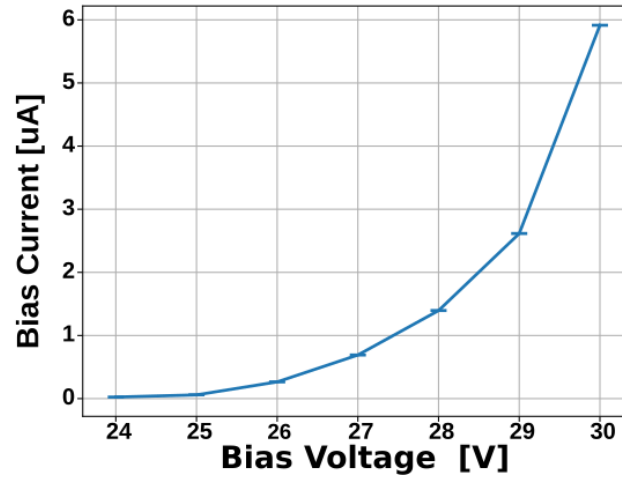
(a) J-30020 SiPM, no ambient light,
bias current vs V_{bias}
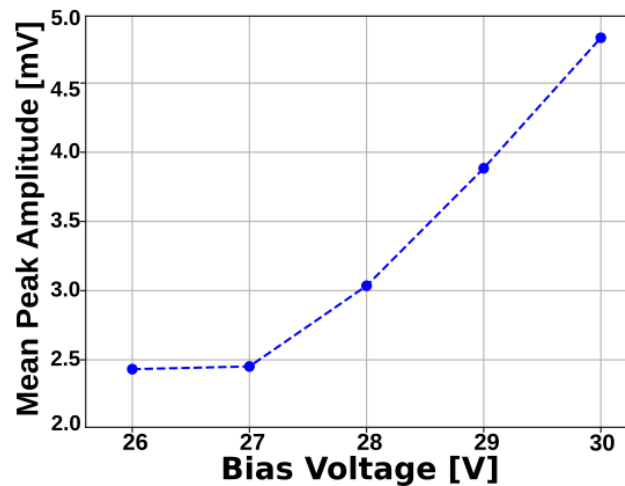
(b) J-30020 SiPM, no ambient light, dark count pulse mean amplitude vs V_{bias}

Figure 3.2: Experimental results showing dark current, and mean pulse amplitude as a consequence of applied bias voltage.

3.5 I_{bias}- Irradiance Response Experiment

After detecting a photon each microcell is recharged by the voltage source used to bias all the microcells above their breakdown voltage. Since each microcell has a capacitance, the current flowing from the voltage source depends upon the rate at which photons are detected and hence output pulses generated. This means that a convenient method of estimating the count rate, and observing the saturation of a SiPMs response, is to measure the relationship between the irradiance falling

onto the SiPM and the current provided by the voltage source biasing the SiPM.

The model in equation (3.5) predicts the bias current as a consequence of the irradiance striking the SiPM. For the J-Series 30020, the I_{bias}-irradiance response was measured at a bias voltage of 27.5 V. A 405 nm source (a ThorLabs L405-P20 laser) was used, and its irradiance was varied by changing the laser bias current. The bias current required to support the bias voltage was then measured with a Keithley 195-A digital multi-meter. A 818-SL calibrated photodiode then replaced the SiPM, and was used to measure the irradiances, which were between 10^{-4} Wm^{-2} and 40 Wm^{-2} .

Figure 3.3a shows the current supplied by the voltage source, as a consequence of the irradiance falling onto the J-30020 or the J-30035 SiPM. As expected, the current supplied to both SiPMs is proportional to the irradiance for low irradiances. The current required by the J-30020 is far lower at low light intensities. A combination of two factors explain this observation, which are a smaller microcell area giving a lower capacitance per microcell, and a reduced PDE meaning fewer photons are detected. By taking the ratio of photon detection efficiency multiplied by microcell area, the predicted current ratio is 4.4.

$$\frac{I_{\text{linear,30035}}}{I_{\text{linear,30020}}} = \frac{\text{J-30035 Microcell Area}}{\text{J-30020 Microcell Area}} \frac{\text{J-30035 PDE}}{\text{J-30020 PDE}}$$
$$= \frac{35^2}{20^2} \frac{0.5}{0.35} \approx 4.37 \quad (3.8)$$

When the ratio of bias current for each SiPM is plotted in figure 3.4, the predicted current ratio suggests the PDE-capacitance product explains the difference in bias current when both SiPMs have a linear response. This result suggests that the J-30020's reduced microcell size (and therefore capacitance of each microcell) in comparison to the J-30035 contributes to the reduced current and hence power required to supply the

J-30020 at a particular irradiance value. This lower current per detected photon means that the similar maximum currents correspond to quite different maximum count rates, shown earlier to be 7.6 times higher for the J-30020 SiPM when contrasted to the J-30035 SiPM.

Furthermore, for the maximum irradiance used in these experiments the J-30020 hasn't reached total saturation. A comparison of the irradiances at which the measured response is 50% of the expected linear response shows that the *J-30020 saturates at an irradiance five times higher than the irradiance at which the J-30035 saturates.* As the irradiance increases the J-30035 saturates at an irradiance of approximately 3 mWm^{-2}, however the J-30020 remains linear until an irradiance of approximately 15 mWm^{-2}. More importantly, despite the smaller capacitance per microcell, this saturation occurs at a higher bias current for the J-30020. These results are therefore consistent with the predicted higher maximum output pulse rate. For a high data rate VLC link, the J-30020 is therefore a promising candidate as it allows for the detection of photons at a higher rate when contrasted to the J-30035 SiPM.

These results are supported by the bias current model in equation (3.5), which was used to predict the count rate of each of the J-30020 and J-30035 SiPMs. This model is shown to be fitted to dynamic range curves in figure 3.3a, by optimising for microcell charge. The data from table 3.1 were inserted into the model and the predicted behaviour observed in figure 3.3b.

The maximum current obtained on the dynamic range curve is 35.65 mA, which when divided by the estimated microcell charge yielded a count rate of 950×10^9 pulses/s. This agrees with the model for the J-30020, which predicts 960×10^9 pulses/s.

3.6 SiPM Paralysability

Previously, the performance of SiPM receivers has been predicted based upon the assumption that *any passively quenched SiPMs*, includ-
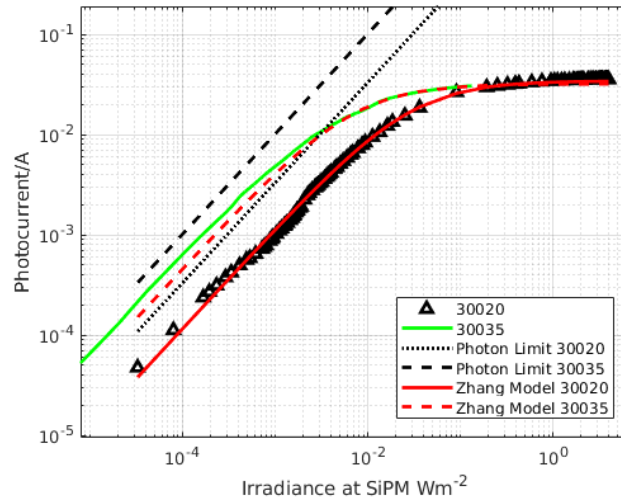
(a) Measured bias current through the J-30020 and J-30035 against measured irradiance. Model fitted by optimising over microcell charge. The 'Zhang Model' is the model in equation (3.5).
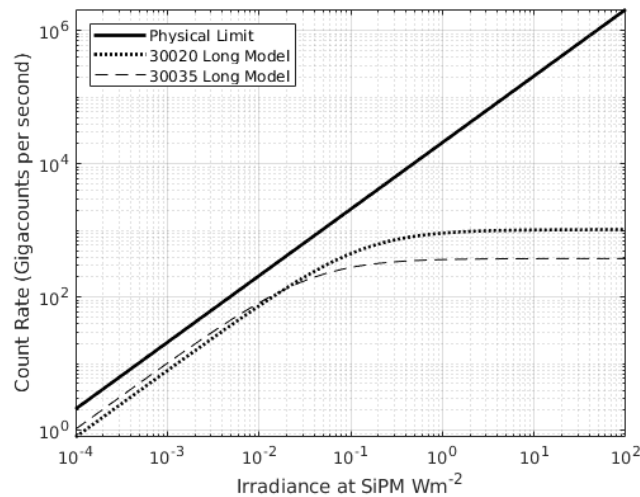
(b) Count rate of the SiPM against irradiance, modelled using equation (3.2). The 'Long Model' is the model in equation (3.2).

Figure 3.3: Measurement and model both showing a saturating effect on SiPM devices.

ing commercially available SiPMs, are paralysable, and when paralysed do not produce output pulses [45, 53, 54]. Since this assumption means that the SiPMs would have a peak performance at a particular total irradiance it has a significant impact on the predicted performance and design of SiPM receivers. However, some designs of microcell are non-paralysable and for these microcells the rate at which photons can be detected saturates to a constant rate at high irradiances. Consequently, their performance at high irradiances is very different from the perfor-
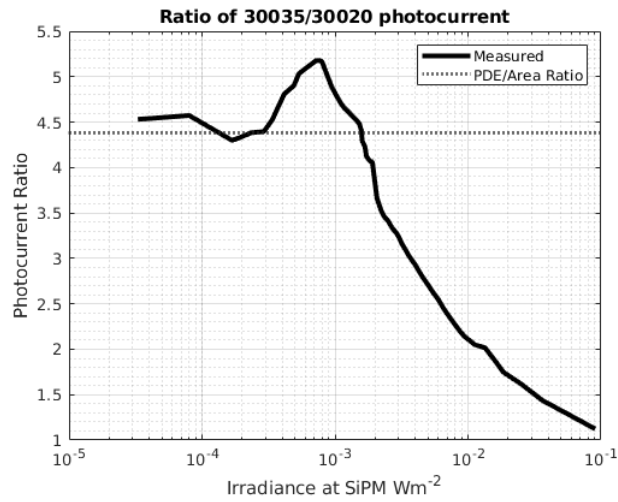
Figure 3.4: Bias current ratio of J-30035 and J-30020.

mance of paralysable SiPMs. When selecting a SiPM for applications in which high photon fluxes may be encountered it is therefore important to determine if the microcells in the SiPM are paralysable or non-paralysable. The performance of a SiPM receiver has therefore been investigated at irradiances that are high enough to differentiate between a paralysable and a non-paralysable SiPM.

The predictions made by other research groups claim passively quenched, including Onsemi SiPMs, are paralysable to the extent that it is not possible to sustain an optical wireless link with sufficiently high irradiances [45, 53, 54]. This is due to the assumption that recharging microcells when struck by a photon discharge, and do not produce an output pulse, the behaviour referred to as being paralysable.

A paralysable model exists to show this behaviour and has previously been used with simulation work to predict the performance of optical wireless links with SiPMs [45, 53, 54]. The model used shows a maximum achievable count rate with SiPM receivers, which is presented below [54]

$$\frac{\mathrm{d}D}{\mathrm{d}t} = N_{\text{cells}}\beta(L + L_{\text{dark}})\exp\left(-\beta(L + L_{\text{dark}})\tau_p\right) \tag{3.9}$$

where τ_p is the paralysable recovery time $\tau_p = \log(2)\tau$ for τ being the recovery time. L and L_{dark} are the irradiance striking the SiPM and the

irradiance required to produce dark counts equivalent to the dark count rate. $\frac{\mathrm{d}D}{\mathrm{d}t}$ is the rate at which photons are detected. Finally, β is defined as

$$\beta = \frac{\eta(\lambda)A_{\text{SiPM}}}{E_p N_{\text{cells}}} \qquad (3.10)$$

where A_{SiPM} is the area of the SiPM, N_{cells} is the number of microcells, E_p is the photon energy and $\eta(\lambda)$ is the photon detection efficiency for wavelength λ.

To test this paralysable claim, an Onsemi J-30020 SiPM was biased at 27.5 V (a 3 V overvoltage), and was illuminated by 405 nm light from an LED ring of eight Bivar UV3TZ-405-15 LEDs placed 45 cm above the SiPM. The current flowing through the LED ring was varied, and the resulting irradiance was measured with an 818-UV calibrated photodiode. The bias current flowing through the SiPM was measured with a Keithley 196 digital multi-meter.

Figure 3.5 shows a comparison between the paralysable and non-paralysable models, plotted with measurements of a J-30020 SiPM bias current. As the J-30020 SiPM is an analog device, whenever an avalanche occurs an output pulse is generated. Current flows through the SiPM when output pulses are generated, meaning that the SiPM bias current can be used to compare the paralysable and saturation models directly. Both a linear model and the paralysable model, fitted using device parameters, closely agree with the measured data until approximately 10^{-2} Wm^{-2} , but fail for higher irradiances. For the linear model, SiPM saturation means the bias current flowing through the SiPM is limited and hence diverges from the linear prediction. When considering the paralysable model however, the model predicts the output pulse rate will decrease after reaching maximum output pulse rate.

This is not the case for Onsemi SiPMs, as the current asymptotically reaches a maximum as irradiance increases. A saturating model, described in detail in equation (3.2) agrees with measurements for the en-

tire range, from dark counts up to saturation. This result means that unlike claims made by other research groups, the J-Series range of SiPMs are not paralysable, and produce output pulses despite device saturation.

In Onsemi SiPMs, the fast output is used for data communications [2]. If the fast output was connected to the global output via an inverter, the fast output could be paralysable when the slow output is not. However, the fast output is connected directly to the global output, so it is not paralysable.
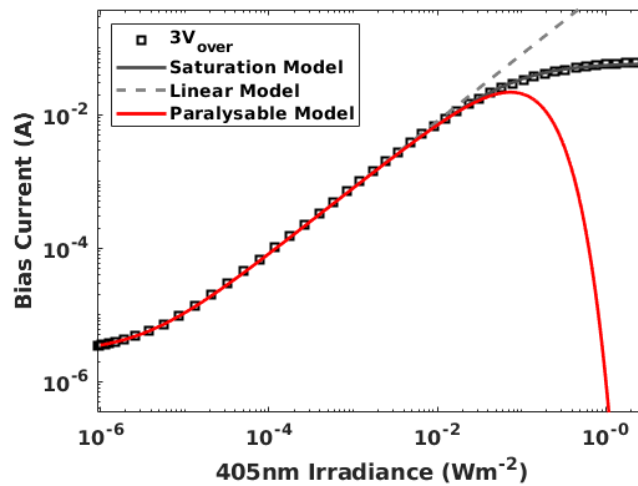
Figure 3.5: J-30020 SiPM I_{bias} vs irradiance curve under 405 nm light, compared with the saturatable model, and the paralysable model.

3.6.1 Bias Current vs Overvoltage Measurements

When the SiPM overvoltage is increased, the bias current consequently increases for the same illuminating irradiance. Figure 3.6 shows experimental results of a J-30020 SiPM's bias current measured against 405 nm irradiance for two different overvoltages. An increase in overvoltage increases SiPM's PDE, but more importantly it increases the charge (and therefore gain) of each microcell. As each microcell can be approximated as a capacitor, the microcell charge follows a standard capacitor charge equation $Q_{microcell} = C_{cell}V_{over}$. This charge is dumped when an avalanche multiplication event occurs, which is the output signal. The ratio of the saturated bias currents in figure 3.6 between the two devices

is 3, which is the same as the ratio of the overvoltages. In the linear region, the ratio of the bias currents between the devices is approximately 4, which is consistent with the PDE increasing with overvoltage.
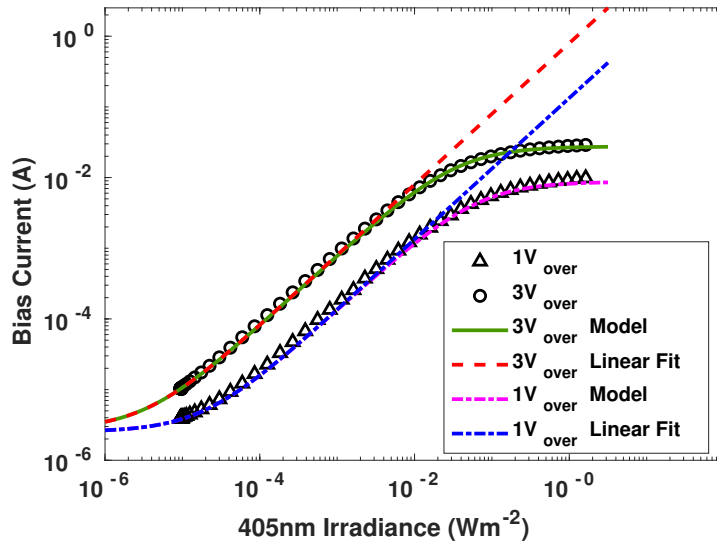
Figure 3.6: J-30020 SiPM Bias Current as a function of applied 405 nm irradiance. Plotted for two different bias voltages.

3.7 Optimal SiPM Biasing Conditions

Since the SiPM's bias voltage is its only practical adjustable parameter, work was performed on optimising the bias voltage for the SiPM's use in VLC systems.

A detrimental impact found during experiments was a higher bias voltage causes faster heating of the device. When the SiPM is operating at its maximum current of $\approx$30 mA when biased at 28 V, the power into the SiPM becomes heat, which consequently has a power of $\approx$0.8 W. From data-sheet values, a +10°C temperature change is expected to give a change of V_{over} of -215 mV, a PDE change of -1%, and a reduced gain of 10%. The heating effect was initially confirmed when a fan was placed adjacent to the J-30020 SiPM under saturated conditions, the bias current and therefore gain increased.

Although the maximum count rate does not change, increasing the bias voltage changes avalanche pulse height, dark count rates, and PDE

which all impact the SNR of the device. Experiments were consequently performed on varying the SiPM bias to achieve the best BER under saturated conditions.

A VLC link was established using a J-30020 SiPM, and V_{bias} was searched to find the bias voltage that gave a BER of 10^{-3} at the highest possible data rate. The amplifiers used were a Mini-Circuits ZFL-1000H+ as the laser amplifier, and a Mini-Circuits ZX60-43S+ for the SiPM fast output amplifier. The bias tee for powering the laser was a Mini-Circuits ZFBT4R2GW+, and the transmitting laser was a 405 nm ThorLabs L405P20. The oscilloscope used was a Keysight MSOV334A 33 GHz, with a Tektronix 70002A AWG. The modulation scheme utilised was OOK with 8b10b encoding, with no pre-equalisation and Decision Feedback Equalisation employed.

The results from the search showed 28.1 V was the most optimal bias under saturated conditions, as it offered the highest transmission rate at a BER of 10^{-3}. This optimum was shallow, and offered a small performance improvement from the previous bias voltage used, 27.5 V [2]. With a target bit error rate of 10^{-3}, using 27.5 V yielded a maximum data rate of 3.30 Gbps, yet using 28.1 V gave a maximum data rate of 3.45 Gbps. This may be due to the higher bias voltage providing a greater gain, and increased PDE without increasing dark counts significantly.

3.8 Data Transmission Experiment

The higher maximum count rate of the J-30020 is expected to allow it to support a higher data rate than the J-30035. In order to test this hypothesis an experiment was performed to compare the required irradiance for the J-30020 and J-30035 SiPMs to deliver a BER of 10^{-3} with DFE in a non-ambiently lit VLC system.

A schematic diagram of the experimental setup described in this section is shown in figure 3.7. The amplifiers used were a Mini-Circuits ZFL-1000H+ for 'Amp 1', and a Mini-Circuits ZX60-43S+ for 'Amp 2'. To com-
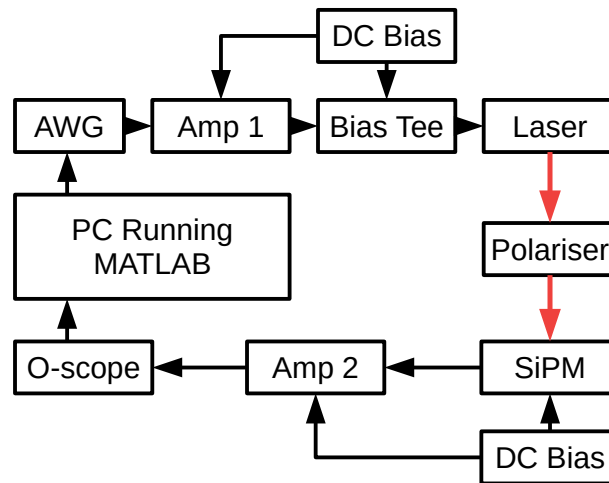
Figure 3.7: Experiment schematic. Red arrows indicate the optical path.

bine DC and RF signals, a laser bias tee, a Mini-Circuits ZFBT4R2GW+, was used, which provided the combined signal to the laser, which was a 405 nm Thor Labs L405P20. The oscilloscope to capture output waveforms was a Keysight MSOV334A 33 GHz, and the AWG used was a Tektronix 70002A. The modulation scheme applied was OOK with 8b10b coding without pre-equalisation. For all experiments a SiPM bias of 28.1 V was used, following from results in section 3.7. 8b10b encoding was used to remove the possibility of a low frequency component being in the signal, this is important as the RF amplifier ('Amp 2') had a passband of 0.5-4000 MHz. The light from the laser diode passed through a collimating lens and into a multi-mode fibre to the transmitter assembly. The transmitter assembly consists of a collimating lens and a ground glass diffuser to create a uniformly illuminated area where the receiver is placed approximately 40 cm from the transmitter assembly.

After capture by the oscilloscope, the waveform was then post-processed in MATLAB. The signal was low pass filtered, aligned using cross-correlation, and then re-sampled to the data rate of interest. Finally, decision feedback equalisation (DFE) was applied to compensate for ISI due to the 1.4 ns fast output pulse width of the SiPM. Recursive least squares were used with a forget factor of 1 and an initial inverse correlation matrix of $20I_{90}$, which is a 90 by 90 identity matrix. For all experiments the DFE

settings used were 70 feed-forward taps and 20 feedback taps. After DFE had been applied, the BER was calculated. With a target BER set at 10^{-3}, eight data rates of interest were identified approximately equis-paced between 500 Mbps and 3.45 Gbps.

For each data rate the intensity of the transmitter was varied by ro-tating a polariser in front of the laser diode. The laser diode outputs a polarised beam, and the polariser, a wire-grid polariser, was used to at-tenuate the beam. The irradiance was controlled such that the BER was approximately 10^{-3}. Since the polariser is imprecise to operate manually, a more accurate result was obtained when the data rate was then varied until the data rate with the required BER was found. Finally, for each data rate the average irradiance of the transmitter at the SiPM was measured by replacing the SiPM with an Newport 818-SL calibrated photodiode.

Figure 3.8 shows the data rates obtained at different irradiances when the BER is 10^{-3} and DFE has been employed. These results show that before either SiPM is saturated the J-30020 SiPM requires a higher ir-radiance, than the J-30035 SiPM to achieve the same data rates. The irradiance ratio to support links at data rates up to 1700 Mbps is the same as the ratio of PDEs. However, for data rates above 2 Gbps, the earlier saturation of the J-30035 means that the J-30020 supports higher data rates at the same irradiance. The most unexpected feature of the results in figure 3.8 is that despite having a maximum count rate that is 7.6 higher than the J-30035, the maximum data rate of the J-30020 is only a factor of 1.4 higher than the J-30035. This indicates the power penalty arising from the bandwidths of all the parts of the system (for instance the laser diode and the SiPM) cause additional ISI.

In situations where higher irradiances can be used, and the data rate must be maximised, equation (3.2) was used in the introduction to cre-ate a simplified metric for SiPM quality. If $\beta \tau_{\text{recharge}}(L + L_{\text{dark}}) >> 1$, the suggested quality metric, $\frac{N_{\text{cells}}}{\tau_{\text{recharge}}}$, maximises the count rate of the SiPM

with no regard to sensitivity. The J-30020's smaller microcell size provides more SiPMs with a lower recharge time, which is more beneficial in this regime. The J-30020's achievement of a higher data rate reflects the importance of this metric when used in environments with high transmitter irradiances. In future VLC links with a high data rate requirement, SiPMs with lower recharge times and a greater quantity of microcells are important to be considered.
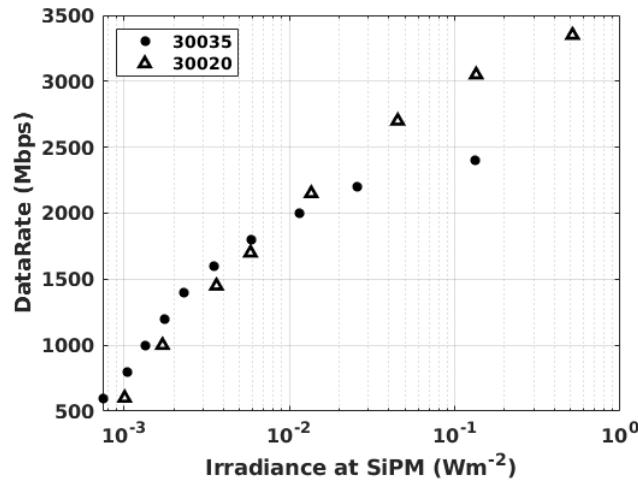
Figure 3.8: Irradiance values achieving a BER of 10^{-3} plotted against data rates.

3.9   Low Irradiance Performance

For low light levels, in the linear region, the SiPM is limited by the count rate it can achieve, which is determined by its area and photon detection efficiency [23]. For irradiances below 10 mWm^{-2} the J-30035 was able to achieve a higher data rate than the J-30020 for the same irradiance. This can be explained through manipulating equation (3.2). If equation (3.2) is assumed to have a low light intensity, such that $\beta \tau_{\text{recharge}}(L + L_{\text{dark}}) << 1$, where β is found in equation (3.1), the count rate simplifies to

$$\frac{dC}{dt} = N_{\text{cells}}\beta(L + L_{\text{dark}}) = \frac{\eta A_{\text{SiPM}}(L + L_{\text{dark}})}{E_p} \tag{3.11}$$

which suggests a 'utility function' of the form ηA_{SiPM}, where η is the PDE of the device, for data rates at which ISI from the SiPM is negligible.

For VLC links restricted to low light levels where the device is in the linear region, maximising this product gives the most sensitive detector. The J-30035 and J-30020 SiPMs both have the same area, but their PDEs differ. This means the J-30035 has a higher count rate in the linear region, and therefore a reduced irradiance requirement for data rates below 1800 Mbps. In future VLC links with a low irradiance requirement, the utility function suggests SiPMs with a large active area may be used, such as Onsemi's J-Series 60035 SiPM as it offers a high PDE and area, increasing the ηA_{SiPM} product. However, a consequence of using larger SiPMs is a wider output pulse width, which introduces ISI and limits the maximum data rate of the device.

Despite achieving a higher count rate than the J-30020 at low irradiances, the J-30035 also consumed more power. The capacitance and recharge time ratio was shown to be three, which is the ratio of the areas (and consequently the capacitance) of the microcell.

$$\frac{C_{30035}}{C_{30020}} = \frac{\text{J-30035 Microcell Area}}{\text{J-30020 Microcell Area}} = \frac{35^2}{20^2} \approx 3.06 \qquad (3.12)$$

This suggests that the J-30020 consumes a third of the power of the J-30035 for the same count rate. When PDE is also considered, the J-30020 consumes only 23% of the power of the J-30035 at a given irradiance, as fewer photons are detected. However for VLC links, Poisson statistics determines the number of detected photons per bit, which changes the required irradiance for the link. This means that for data rates which are not impacted by microcell recharge times, the J-30020 consumes a third of the power relative to the J-30035, but requires a transmitter which is 43% brighter. The J-30020 may therefore be more suitable for systems such as a smart phone, where power consumption is an important factor, or situations where the eye-safe limit can be ex-

ceeded and the data rate of the system is the most important factor.

3.10   Discussion

The newly identified J-Series 30020 SiPM was characterised, which included measurement of breakdown voltage and dark count performance. The maximum count rate of the SiPM was shown to not increase with bias voltage, and its bias voltage optimised to 28.1 V to achieve higher data rates. Typical results were observed, including pulse amplitude increasing with overvoltage and cross-talk probability increasing with overvoltage.

Previously, the performance of SiPM receivers was predicted based upon the assumption that any passively quenched SiPMs are paralysable, and when paralysed do not produce output pulses. J-Series SiPMs are passively quenched, so the claim that they are paralysable was investigated. Measurements of the bias current found that output pulses are still generated under high irradiances, which demonstrated that the J-Series SiPM is not paralysable.

Recently, it was reported that despite saturation when a J-30035 SiPM is used the maximum OOK data rate with a BER of 10^{-3} was 2.4 Gbits/s. Results have been presented which show, that because it has a higher output pulse rate at saturation, and saturation occurring at a higher irradiance, a J-30020 SiPM can achieve the same BER at a data rate of 3.45 Gbits/s. This is a new record for the data rate achieved with a SiPM, however, saturation means that these high data rates occur at irradiances of more than 100 mWm^{-2}. At lower irradiances which are more likely to occur when a VLC system is deployed, the higher PDE of the J-30035 means that it achieves a slightly higher data rate at the same irradiance than the J-30020. The J-30035 SiPM remains the most sensitive receiver for low light levels (below 12 mWm^{-2}).

Chapter 4

Operation in High Ambient Light Environments

4.1 Overview

This chapter focuses on the usage of Silicon Photomultipliers in environments where high levels of ambient light are present. Silicon Photomultipliers have been shown to suffer a performance detriment when exposed to ambient light, which may limit the ability to practically use SiPMs as VLC receivers [2, 12, 55, 25]. In this chapter, the impact of ambient light is investigated, and a new form of ISI, caused by the history of the irradiance at the SiPM is presented.

In recent work, SiPMs have also achieved excellent data rates up to 3.4 Gbps with OOK [38], however all the research presented has been performed on evaluation boards with a series readout resistor for the 'slow output'. This series resistor, which is unnecessary for VLC receivers which use the fast output, is shown to cause detrimental effects to the performance of the SiPM. In this chapter, this performance penalty is examined for the existing J-30020 SMA evaluation board, and a newly identified J-30020 evaluation board.

Receiver performance prediction with Poisson statistics motivates combining multiple SiPMs together, which is initially characterised.

4.1.1 Impact of Ambient Light on SiPMs

SiPMs have no mechanism to discriminate the origin of photons and therefore either ambient light or an optical communications signal can trigger an avalanche. Detection of ambient photons causes a penalty to optical communications links as it adds noise power to the output waveform. Additionally, as the ambient illumination's irradiance increases, the rate of photons arriving at the SiPM means that microcells will avalanche while they are recharging after detection of a photon. This additional penalty is unknown and may have a significant impact on SiPM receiver based optical wireless links in ambiently lit environments.

4.2 Microcell Recharge ISI

Ahmed minimised the impact of ambient light using a bandpass interference filter which negatively restricts the receiver's FoV [2]. The band which is filtered depends on the angle of incidence of the light, which means that the receiver's FoV is limited to a cone of a few degrees. The performance of a SiPM has therefore been investigated without an optical filter to increase the FoV and quantify the penalty of operation in ambient light. It was observed that when a SiPM is used in a VLC system, DFE improved the performance of the system at lower data rates than expected from the ISI caused by the width of output pulses.

At 100 Mbps, and under high levels of background light, it was observed that not using DFE meant high transmitter irradiances were needed, and still a bit error rate below 10^{-3} could not be achieved, even with transmitter irradiances up to 100 mWm^{-2} . Interestingly when DFE was used in this case, a data rate far below the point at which ISI caused by output pulse width has impact, the required transmitter power was reduced. This phenomenon was hence explored through setting up VLC systems with no ambient light, and under ambient light to explore the effect. The usefulness of DFE suggests a new type of ISI, and this possibility was

investigated. Decision Feedback Equalisation and Linear Equalisation (LEQ) were applied to attempt to correct the phenomenon. A performance benefit of using LEQ under conditions of the newly observed ISI being present are also presented and discussed.

4.2.1 Data Transmission Results with Ambient Light

Excellent results have previously been obtained when a FB405-10 optical band-pass filter was incorporated into a SiPM receiver [2]. Experiments were hence performed in 500 lux of ambient light from the warm white LED with and without a FB405-10 filter in place to investigate the impact of ambient light on the SiPM receiver. The required mean transmitter irradiance to support a link at a BER of 10^{-3} was gathered at data rates from 100 Mbps to 1 Gbps, in 100 Mbps increments, both with and without DFE.

The same experimental setup as described in section 3.8 was used, with the addition of a WLED lamp to provide ambient light on the SiPM. A schematic diagram of the experimental setup used for all experiments described is shown in figure 4.1. The WLED bulb used was an 8 W Philips IBRS 10461 domestic lighting bulb, whose spectrum is shown in figure 4.2. For all experiments a SiPM bias of 28.1 V was used, following results in section 3.7. A wire-grid polariser was used to vary the optical power from the transmitting laser, which changed the irradiance falling upon the SiPM, and hence the BER.

The results in figure 4.3 show that with the filter in place, applying DFE only has an impact on data rates of 500 Mbps or higher, where the output pulse width of the SiPM's fast output begins to cause ISI. However, when the receiver is operated without a filter in 500 lux WLED ambient light, applying DFE has significant impact on data rates less than 400 Mbps. This benefit is due to DFE correcting the new ISI present in the system. When the filter is removed from the receiver, the current needed to maintain the SiPM bias voltage increases from 0.27 mA to 31 mA,
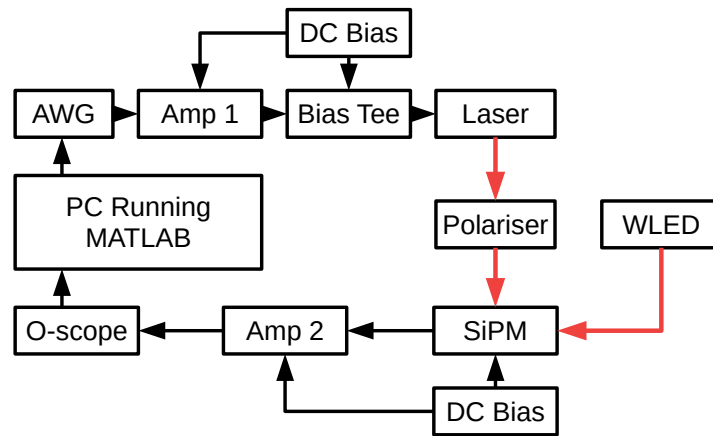
Figure 4.1: Experimental Setup. Red arrows indicate optical signal paths. This setup is similar to that described in section 3.8, with the addition of a WLED lamp to provide ambient light on the SiPM.
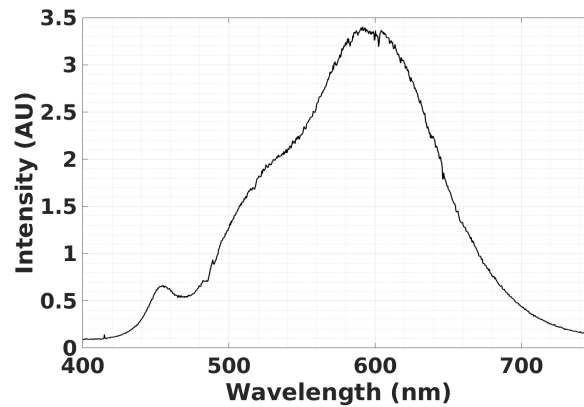
Figure 4.2: White LED spectrum from the 8 W Philips IBRS 10461 domestic lighting bulb, used as background illumination.

which when compared with figure 3.6 means the SiPM is operating in its linear region for when the filter is present, and near saturated region without the filter.

4.2.2 Eye Diagram Form and Comparison

When establishing a communications channel with no ambient light, and using the SiPM's fast output, the eye diagram from the system is typical. An experiment was performed to capture an example typical eye diagram, before DFE, at 100 Mbps. The transmitter irradiance was varied until the BER reached 10^{-3} when DFE was applied. Figure 4.4a shows the typical resultant eye diagram, which has open eyes and visible pulses for each symbol. The differing pulse heights for each symbol are a result of Poisson noise, through different numbers of photons arriving
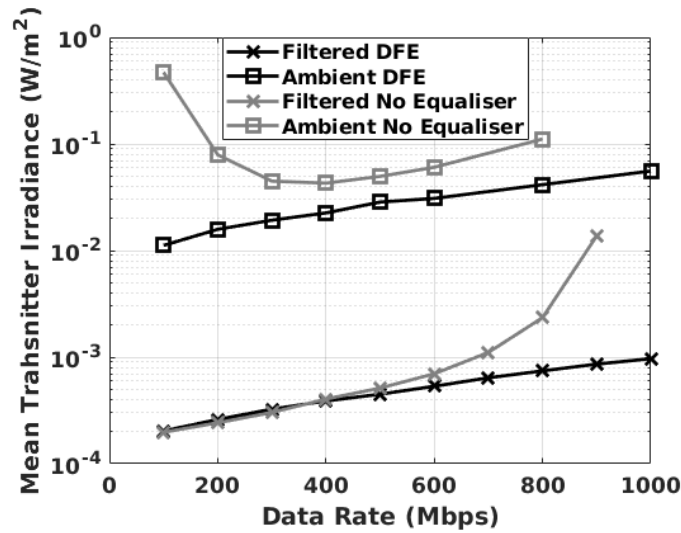
Figure 4.3: Transmitter irradiance required to achieve a BER of 10^{-3} when a FB405-10 filter is in place and after removal. In both states experiments were performed with and without DFE.

and being detected for each bit.
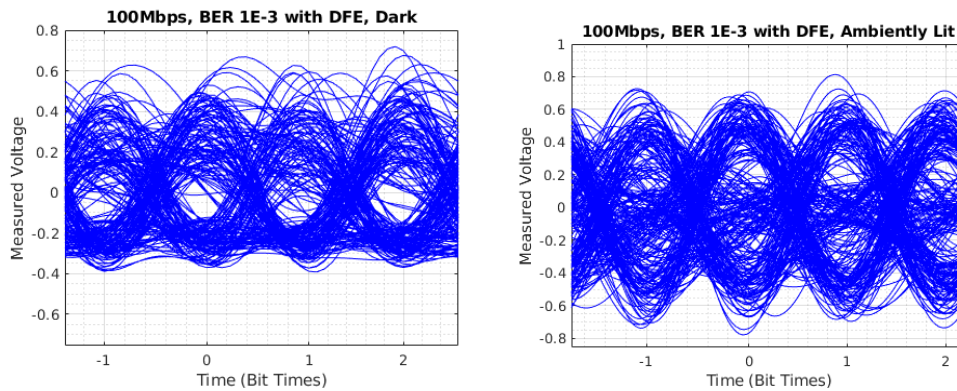
(a) VLC link eye diagram with no ambient light. This eye diagram is *typical* for the SiPM, note that eyes are open.

(b) VLC link eye diagram in an ambiently lit channel. This eye diagram is *atypical* due to the signal appearing to pass through the centre of each eye.

Figure 4.4: Bit shape of the SiPM's fast output under non-ambiently lit (left) and ambiently lit (right) conditions, achieving a bit error rate of 10^{-3} using DFE (70 feed-forward, 20 feedback) at 100 Mbps. 10,000 samples are shown in each plot, at 20 samples per bit.

An experiment at the same data rate was then performed to capture the case where ambient light is present. At this data rate, not equalising the signal did not require a higher transmitter power compared to when DFE was employed. The WLED bulb was turned on, providing 500 lux of WLED light, and a VLC link established. A bias current of 31 mA was measured, confirming the SiPM was deep into the saturation region.

The transmitter irradiance of the 100 Mbps link was adjusted such that a BER of 10^{-3} was achieved when DFE was applied. Eye diagrams such as figure 4.4b were then observed in multiple experiments. When the amount of ambient illumination was varied, the eye diagram's shape changed from figure 4.4a to figure 4.4b as the SiPM became saturated. This eye-diagram under ambient light has an unexpected shape, with a level appearing in the middle, which appears to show a new form of ISI.

Figure 4.4b shows an eye is visible but appears to be obscured by an additional level at 0 V, pulses seem to not be able to maintain their high or low voltage for a series of repeated ones or zeroes. The low and high levels (representing bits 0 and 1) converged in the middle of the eye as the ambient irradiance increased. The presence of the additional level is more visible in figure 4.5a, which uses a higher transmitter power transmitter to exaggerate the phenomenon. This results in SiPM output voltages at 12×10^{-8} and 16×10^{-8} seconds are identical despite having different symbols. When DFE is applied, the required transmitter irradiance is lower, which results in similar but more noisy bit shapes, shown in figure 4.5b. Another view of the new form of ISI can be found in figure 4.6, which shows a specific pattern of bits (0,0,1,1,1,1) and its complement, captured from a PRBS data stream. This new ISI is clearly visible in the differences between the two plots, where the capture with ISI present rapidly returns to a DC mean, no matter if ones or zeros are sent.

The strange form of ISI in the eye diagram has its origins in the the non-linear response of the SiPM from the non-linear curve in figure 3.3a. The history of the irradiances at the SiPM will determine the proportion of the microcells which are recharging, and hence the effective PDE of the SiPM, leading to a response which is nonlinear in time. The RC time constant on bit shapes in figure 4.6a, where the new ISI is not present, is due to the laser amplifier and bias tee forming a bandpass filter which

has a 3 dB cut in at 0.1 MHz.

When bits of data are transmitted a the SiPM near saturation, the effective PDE during a symbol time then depends upon the preceding bits. At 400 Mbps, where the new form of ISI doesn't occur, the bit time is 2.5 ns which means that there are 26 bits during the J-30020's 66 ns recharge time. Consequently, with 8b10b coding, each bit suffers from a similar reduction in PDE. In contrast, at 100 Mbps there are fewer than 7 bits in the recharge time and the reduction in PDE will vary between bits. This data rate dependence of the variability of the effective PDE for different bits possibly explains why DFE has a larger impact at data rates less than 400 Mbps in figure 4.3. The most important conclusion from figure 4.3 is that conventional DFE has a significant impact on this new form of ISI. Despite the benefits of DFE, the results in figure 4.3 show that in 500 lux of ambient light, removing the filter increases the irradiance required to support data rates between 100 Mbps and 1 Gbps by a factor of approximately 60. Removing the filter increases the receiver's field of view but at the cost of significantly increasing the irradiance required to transmit data. Consequently, without a filter the J-30020 SiPM requires an average transmitter irradiance at the receiver of 55.7 mWm^{-2} to support 1 Gbps at a BER of 10^{-3}.

4.2.3   Comparison of Equalisers

DFE is typically used with SiPM receivers, as the required irradiance to achieve a target bit error rate is greatly reduced when contrasted to not using any form of equalisation [25]. To benchmark DFE, a comparison to LEQ and using no equalisation was attempted.

Data were captured from 100 Mbps to 900 Mbps, with a target BER of 10^{-3}. Each BER was calculated from 327,680 symbols, the number of errors for a BER of 10^{-3} is 327. The system's BER was set through controlling the transmitter's irradiance, by manually adjusting the optical polariser until the target BER was reached within a range of 8×10^{-4} to

(a) High transmitter power to exaggerate the effect

(b) Low transmitter power, typical to experimental data
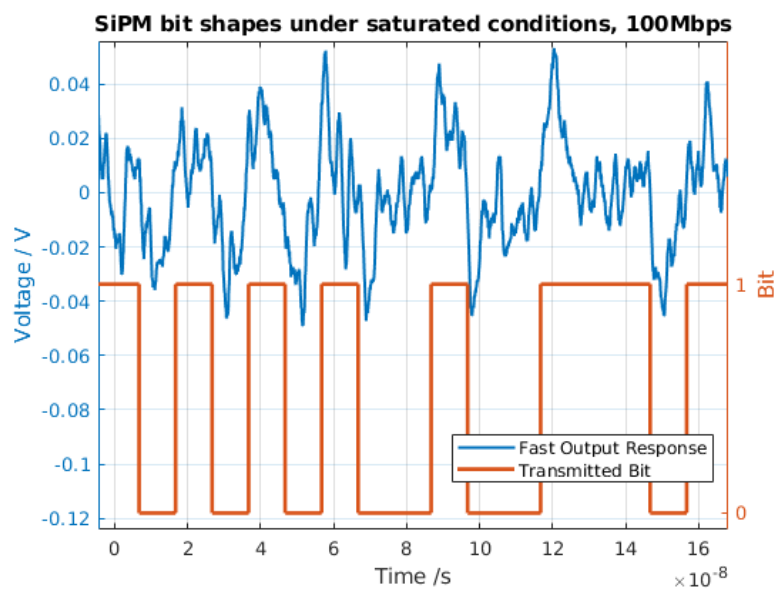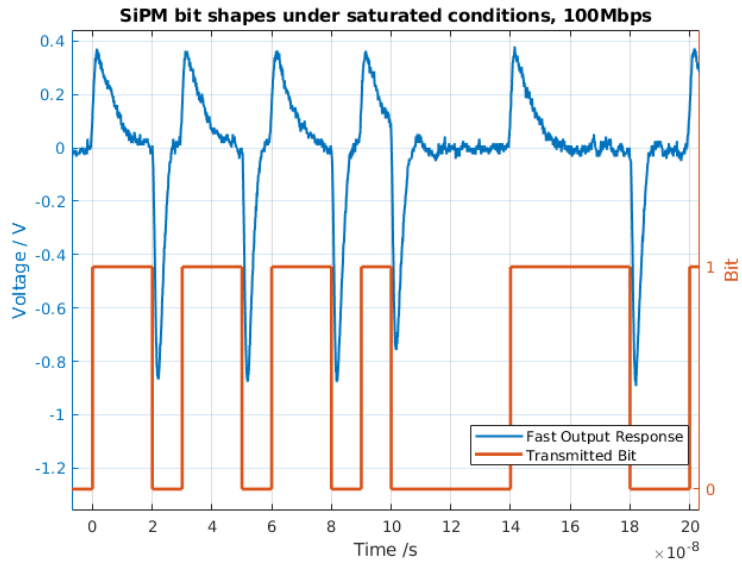
Figure 4.5: Bit shapes due to the newly observed ISI, note the decay towards 0 V for a series of repeated bits

(a) Bit shapes at 100 Mbps with no ambient light. No ISI is visible.

(b) Bit shapes at 100 Mbps under 500 lux of ambient light causing ISI.
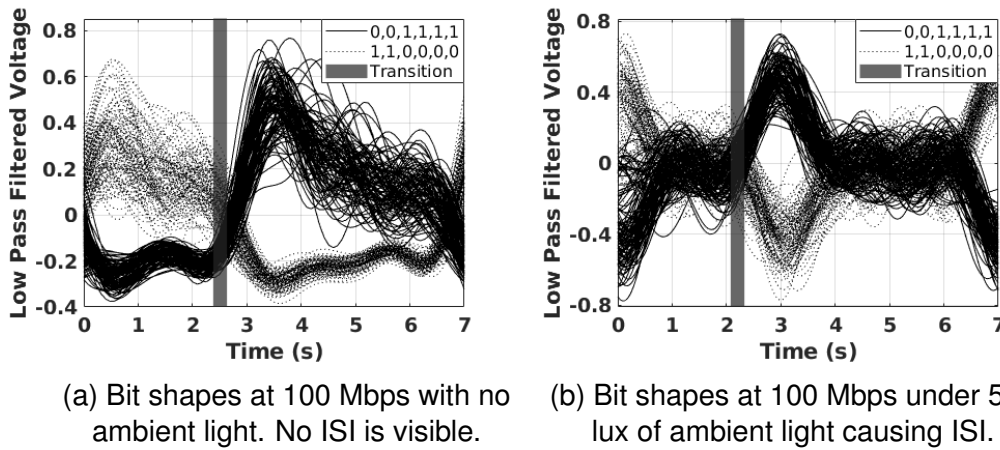
Figure 4.6: A selected pattern of bits (0,0,1,1,1,1) and its complement with and without the newly observed ISI at a rate of 100 Mbps.

2×10^{-3}. The captured wave-forms were then post-processed using both DFE and LEQ.

For DFE, 70 feed-forward and 20 feedback taps with two samples per bit was used. To ensure DFE was optimised, combinations of number of feed-forward taps were varied from 2 to 200, and the number of feedback taps were varied from 1 to 100. Going beyond 70 feed-forward and 20 feedback taps showed no improvement.

For LEQ, 20 feed forward taps were used, and a reference tap position of 11 was used. The reference tap position defines how many taps in the past, and therefore the future are being used from the signal. As with DFE, these parameters were varied to confirm the LEQ was optimised.

Experiments were initially performed for the case where no ambient light was present. Table 4.1, documents the BERs for each equaliser. Not using an equaliser has an expected detrimental effect, with the bit error rate increasing by an order of magnitude at higher data rates, where the bit time and pulse width are comparable. This suggests a small quantity of conventional ISI is present with no ambient light at all data rates, however a rapid increase in conventional ISI occurs once the bit period is shorter than the pulse width. The results also suggest DFE has an comparable performance to LEQ when using a link with no ambient light, as the ratio of the BERs between the two decoding schemes is approxi-

mately one for all data rates.
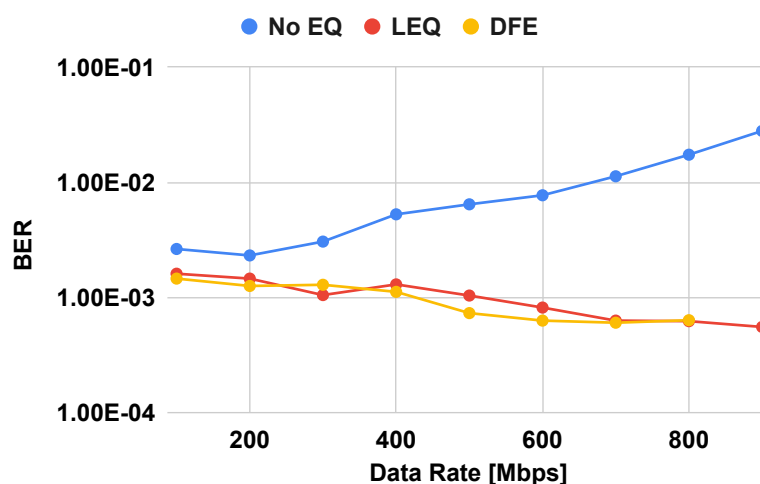
Figure 4.7: Results in table 4.1 plotted to show BER vs Data Rate for different equalisers. No ambient light present.

It was unexpectedly observed at low data rates that DFE seems to be able to correct the newly observed ISI and reduce the bit error rate. Experiments were performed to repeat the comparison of DFE with LEQ, but with 500 lux of ambient WLED light.

Table 4.2 documents the resultant BERs of the different equalisers for this experiment, and figure 4.8 plots these results. Not using an equaliser again has an expected detrimental effect, worsening at higher data rates. The results interestingly suggest a trend of LEQ having an improved performance over DFE, as the ratio of the BERs is almost always below one. The only outlier was 300 Mbps, where the BER of achieved by LEQ was

Table 4.1: BERs achieved under non ambiently illuminated conditions for No Equaliser, LEQ, and DFE

Data Rate (Mbps)	No EQ BER	LEQ BER	DFE BER	LEQ/DFE Ratio
100	2.64E-3	1.61E-3	1.14E-3	1.41
200	2.32E-3	1.46E-3	1.46E-3	1.00
300	3.06E-3	1.05E-3	1.26E-3	0.83
400	5.28E-3	1.30E-3	1.29E-3	1.01
500	6.45E-3	1.04E-3	1.12E-3	0.92
600	7.73E-3	8.18E-4	7.32E-4	1.12
700	1.13E-2	6.30E-4	6.30E-4	1.00
800	1.74E-2	6.23E-4	6.04E-4	1.03
900	2.80E-2	5.55E-4	6.35E-4	0.88

1.1 times that achieved by DFE. At a data rate of 100 Mbps, the largest difference between LEQ and DFE occurs, where LEQ beats DFE by a factor of two.

When compared to the results for the link with no ambient illumination (table 4.1, figure 4.7), the results suggest that this non-conventional ISI is more adequately suited to LEQ than DFE. This result may be due to DFE only tracking the assigned symbol, and discarding information on the number of fired microcells, whereas LEQ has access to that information, and is using it to its advantage to achieve an improved BER performance. The results for not using an equaliser, visible in figure 4.9 suggests that the newly observed ISI is more dominant at lower data rates, which suggests data points at even lower data rates should be investigated in the future where the effect may worsen.

Table 4.2: BERs achieved for a 500 lux Ambiently illuminated SiPM with the application of No Equaliser, LEQ and DFE

Data Rate (Mbps)	No EQ BER	LEQ BER	DFE BER	LEQ/DFE Ratio
100	1.00E-1	9.28E-4	1.86E-3	0.50
200	2.93E-2	7.62E-4	8.06E-4	0.95
300	1.42E-2	1.16E-3	1.05E-3	1.11
400	9.67E-3	1.59E-3	2.37E-3	0.67
500	7.35E-3	1.25E-3	1.34E-3	0.93
600	1.00E-2	1.33E-3	2.00E-3	0.67
800	2.52E-2	1.25E-3	1.73E-3	0.72
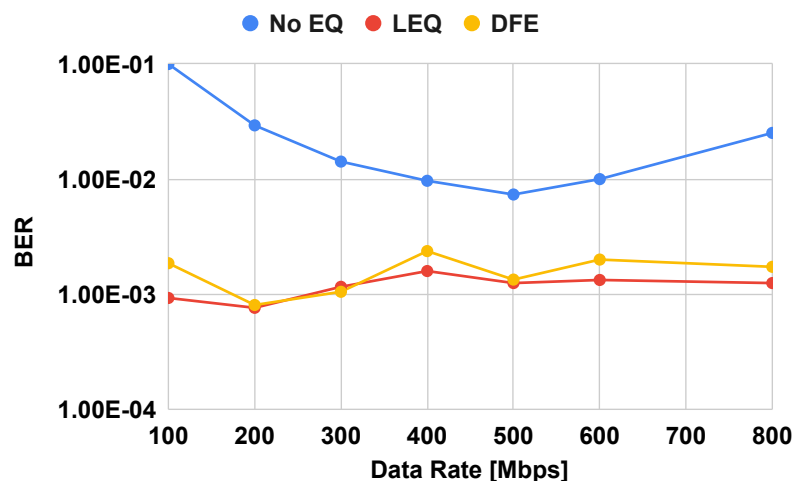
Figure 4.8: Results in table 4.2 plotted to show BER as a function of data rate for different equalisers. 500 lux of ambient light present.
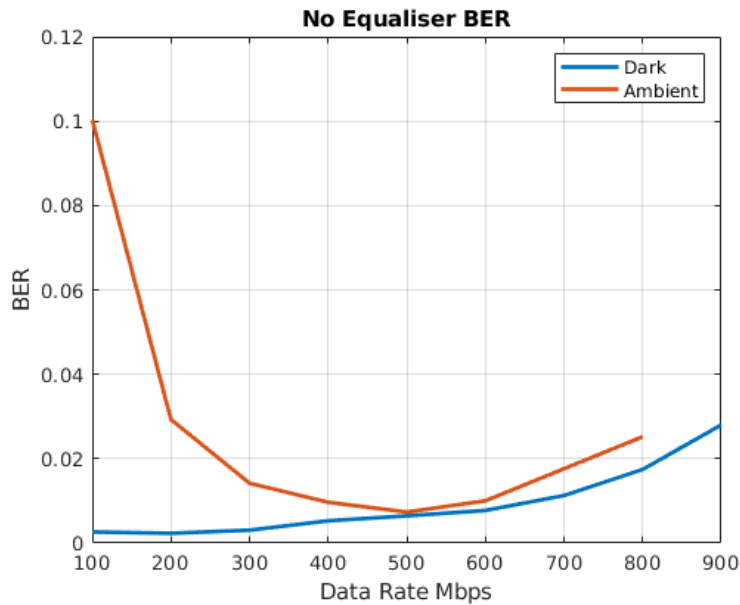
Figure 4.9: Link BER with no equaliser in ambiently lit and non-ambiently lit conditions for data rates between 100 Mbps and 900M bps.

4.3 Comparison of SMA and SMTPA Evaluation Boards

Onsemi produces two different evaluation boards for J-Series SiPMs. One evaluation board, named after its Subminiature A (SMA) connectors, has been used extensively in previous chapters, as it provides a convenient package for rapid experiments. The other evaluation board manufactured by Onsemi is a Surface Mount Technology Pin Adaptor (SMTPA), evaluation board, which connects the surface mount (SMT) SiPM to header pins. These evaluation board were compared to determine what performance differences there are between the two.

4.3.1 SMA Evaluation Board

The SMA evaluation board exposes the fast output, but also an output which measures the total bias current through the SiPM. Unfortunately, the evaluation board uses a 50 Ω resistor in series with the SiPM's anode, which may impact the performance of the SiPM. As a J-30020 SiPM in saturation draws a current of approximately 30 mA, 1.5 V of overvoltage
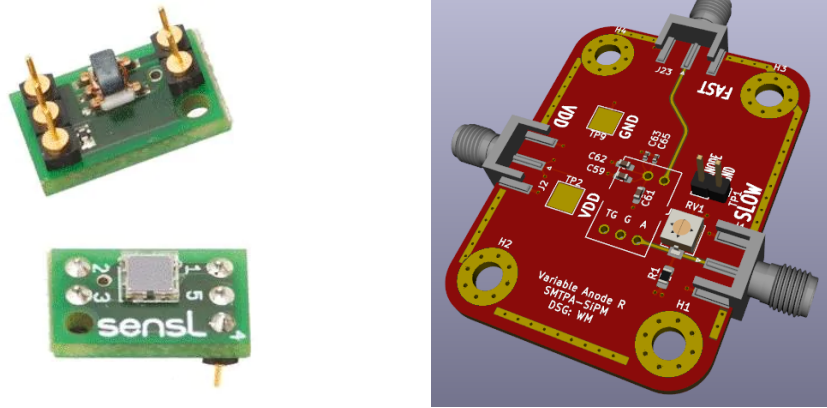
(a) SMTPA evaluation board [30].

(b) 3D render of the SMTPA host PCB (SMTPA board excluded).

Figure 4.10: Computer aided design images of the SMTPA receiver PCB.

would therefore be lost, which reduces the gain, and the PDE of the device.

4.3.2 SMTPA Evaluation Board

The SMTPA evaluation board provides the ability to connect the SiPM directly to the power rails, which removes the 50 Ω series resistor [30]. Removing this anode resistance also reduces the recharge time of the microcell, which has been shown to be beneficial in achieving a high data rate in section 3.2.1. The SMTPA evaluation board is also interesting, as it allows for the development of more tightly integrated SiPMs into a receiver.

A four-layer printed circuit board (PCB), shown in figure 4.10 was designed to host the SMTPA evaluation board, with a maximum design frequency of 5 GHz, and 50 Ω traces on the fast output. Decoupling capacitors to ensure a stable power supply up to 5 GHz were were also included.

The SMTPA evaluation board has a significantly smaller area than the SMA evaluation board and hence required cooling from a 40 mm fan. This cooling was included by mounting the SMTPA host board inside a 3D printed structure, with a duct from the fan channelling the airflow directly to the SiPM.

4.3.3   Saturation Current

A ring of eight Bivar UV3TZ-405-15 LEDs was placed 45 cm above the SiPM under test. The optical power from the LEDs was controlled by changing the current through the LEDs with a Keithley 224 source measure unit. The resulting irradiance at the SiPM was measured by a Newport 835 irradiance meter with a 818-UV calibrated photodiode head. The SiPM under test was biased by an Agilent e3631A programmable bench power supply, which was measured by a Keithley 175 multi-meter. The Agilent e3631A provided inconsistent voltages when the bias current through the SiPM changed, causing a drift of $\pm$ 200 mV. A feedback loop was hence incorporated in MATLAB to ensure the correct bias voltage was applied.

By assuming each microcell behaves as a capacitor, microcell charge (Q_{cell}) and hence cell capacitance (C_{cell}) can be measured. When the SiPM is deeply saturated ($\alpha \tau L >> 1$), the maximum count rate of the SiPM is reached $\dot{D}_{max} = \frac{N_{cells}}{\tau}$. Combination of these assumptions results in a measure of cell capacitance as

$$C_{cell} = \frac{I_{bias}\tau}{N_{cells}V_{over}} \tag{4.1}$$

The microcell capacitance was measured to be 42 fF through observing the saturation current at 34 overvoltages from 0.5 V to 3.9 V and fitting a line with least squares.

Irradiances provided by the LED ring at 405 nm were varied between 10^{-5} Wm^{-2} to 1 Wm^{-2} , and the resulting bias current was measured. The measurements are consequently shown in figure 4.11, where a linear model was fitted along with the SiPM bias current model. The model for bias current as a consequence of irradiance (equation (3.5)) is repeated below in equation (4.2), which was hence fitted for each of the evaluation

Table 4.3: Fitting Parameters to compare J-30020 SMA and SMTPA boards. Only τ_{recharge} changes between the two devices.

Variable	SMA	SMTPA
η	0.34	0.34
Q_{cell}	42 fF	42 fF
L_{dark}	3.4 μWm^{-2}	3.4 μWm^{-2}
τ_{recharge}	30 ns	15 ns
A_{SiPM}	9.42 mm^2	9.42 mm^2
N_{cells}	14410	14410

boards.

$$I_{\text{bias}} = \frac{Q_{\text{cell}} N_{\text{cells}} \beta (L + L_{\text{dark}})}{\beta \tau (L + L_{\text{dark})}} \tag{4.2}$$

where Q_{cell} is the mean charge per fired microcell, N_{cells} is the number of microcells, the characteristic time τ is 2.2 times the recharge time of a microcell, L is the 405 nm irradiance on the SiPM, and L_{dark} is the equivalent 405 nm irradiance causing dark counts. Finally, β is defined as

$$\beta = \frac{\eta A_{\text{SiPM}}}{E_p N_{\text{cells}}} \tag{4.3}$$

where η is the PDE of a microcell and A_{SiPM} is the area of the SiPM. When fitted for both receiver evaluation boards, the model equation (4.2) provided a very good agreement with measured data. The parameters used for the fit are detailed in table 4.3 where the only change between the two evaluation boards was the recharge time. The SMTPA evaluation board has a recharge time half that of the SMA board, which implies the maximum count rate is double that of the SMA board. Being able to detect photons at a higher rate means that the SMTPA board is more suited to operation in ambiently lit environments.

When the J-30020 SMA and SMTPA were exposed to 1 Wm^{-2} of 405 nm light, at 3 V_{over} the resulting bias currents were 28.0 mA for the SMA and 56.7 mA for the SMTPA evaluation boards respectively. This difference is explained by the change in the recharge time of a microcell. When a microcell recharges, the avalanche diode becomes a capacitor. Inside the microcell is a resistor which quenches avalanches, which is in
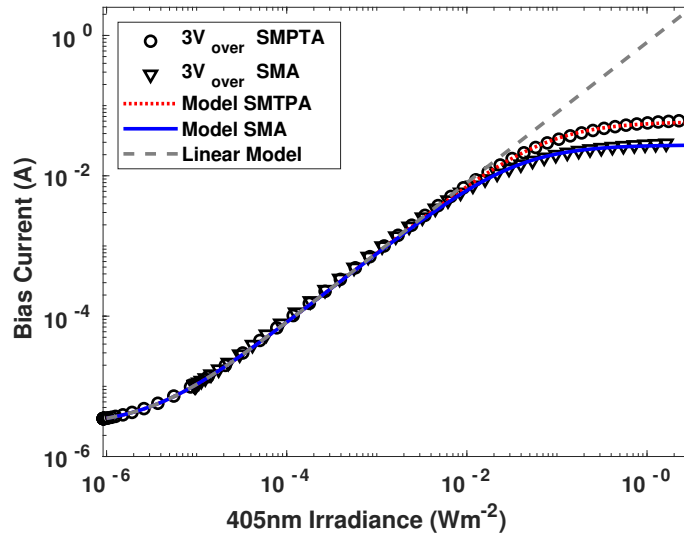
Figure 4.11: I_{bias} as a consequence of irradiance for SMA and SMTPA evaluation boards. Illumination at 405 nm by eight Bivar UV3TZ-405-15 LEDs at a bias voltage of 3 V_{over}.

series with the avalanche diode. This means that the recharge time of the microcell is a RC time constant. Introducing the 50 Ω resistor doubles the effective resistance in series with the microcells, which doubles the RC recharge time.

When the recharge time is measured for the SMA board, the recharge time is 30 ns [2], however for the SMTPA evaluation board this cannot be measured due to the lack of a readout resistor to measure over. The data-sheet value for a 1 Ω anode resistance the recharge time is 15 ns [30] was hence used which provided a high quality fit, and explaining the difference between the two evaluation boards.

4.3.4 Comparison of PDE Measurements

The PDE as a function of overvoltage when the irradiance from the 405 nm LED ring was 2.4 mWm^{-2} was also measured. 2.4 mWm^{-2} is within the linear region of the device, so the method for measurement of effective PDE in equation (4.5) becomes a measurement of the PDE. The overvoltage was varied between 0.5 V to 3.9 V in 100 mV increments, and the bias current was measured for both SMA and SMTPA evaluation boards. An empirical model was hence fitted for the PDE as a function

of the overvoltage V_{over},

$$\eta(V_{over}, \lambda = 405 \text{ nm}) = 0.46 \left(1 - \exp \left(\frac{-V_{over}}{0.083 \cdot V_{br}} \right) \right) \qquad (4.4)$$

where V_{br} is the breakdown voltage of the SiPM, and coefficient of 0.46 is specific to 405 nm light. When The SMA and SMTPA evaluation boards are compared, they show identical PDE-overvoltage characteristics. When measured for a particular irradiance in the linear region, as the overvoltage increases, the PDE rises. Figure 4.12 shows both the measured PDEs of the evaluation boards and the model as a function of the SiPM overvoltage. Both evaluation boards have an approximately identical bias voltage to PDE relationship, which is expected as both SiPMs are operating in their linear regions.
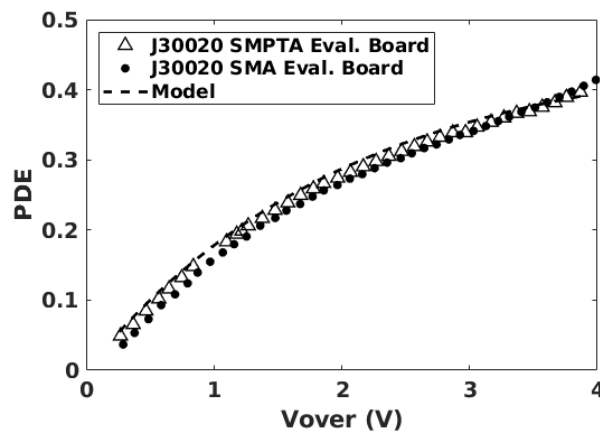
Figure 4.12: J-30020 SMA and SMTPA PDE vs Bias Voltage

4.3.5 Measurement and Comparison of Effective PDE

The effective PDE of a SiPM macroscopically quantifies the impact of microcells recharging on the overall output pulse rate. The average PDE of the SiPM is reduced at high irradiances, because the microcells are detecting photons while recharging. Figure 4.11 shows a difference in the bias current between SMA and SMTPA evaluation boards in the saturation region. This difference can be interpreted as a difference in the *effective PDE*, which assumes the SiPM has no recharge effects, and all saturation effects are explained as a change in the PDE. Effective PDE

was measured by modifying equation (4.2) to express PDE as a function of device measurements under the assumption that the denominator is 1. The effective PDE is hence defined as

$$\eta_{\text{eff}}\left(V_{\text{over}}, \lambda\right) = \frac{E_P(\lambda) I_{\text{bias}}\left(V_{\text{over}}, L\right)}{C_{\text{cell}} V_{\text{over}} A_{\text{SiPM}} \cdot \left(L + L_{\text{dark}}\right)} \tag{4.5}$$

A J-30020 SiPM on an SMA evaluation board was exposed to irradiances between 0.1 mWm^{-2} and 1 Wm^{-2} from the 405 nm LED ring, and the bias current was measured with a Keithley 196 digital multi-meter. Bias voltages were measured over the SiPM and series resistor. Figure 4.13a shows the impact of varying the bias voltage, where in the linear region of the device an increased bias voltage causes a higher bias current. The roll-off in effective PDE begins at approximately 10 mWm^{-2} for all tested bias voltages, and rolls off at 20 dB per decade. This change in effective PDE arises from microcells recharging, meaning they are less likely to detect a photon.

Finally, the SMA and SMTPA evaluation boards were compared at an overvoltage of 3 V. As the irradiance falling upon the SiPM increases, a higher bias current flows through the SiPM and hence the 50 Ω series resistor on the SMA evaluation board. This current causes a significant drop in bias voltage on the SiPM, as much as 1.5 V, which in turn causes an additional penalty on the effective PDE. The results in figure 4.13b show for an overvoltage of 3 V, the SMTPA board has a higher effective PDE than the SMA evaluation board for 405 nm irradiances above 10 mWm^{-2} , when saturation occurs. At an irradiance of 1 Wm^{-2} , the SMA evaluation board's effective PDE was 0.012 and the SMTPA evaluation board's effective PDE was 0.023, giving a ratio of approximately two, which agrees with the measurement of saturation currents above. Importantly this result shows that for the J-30020 SiPM the effective PDE rapidly decreases as the device saturates, which must be taken into consideration as it may cause significant performance penalties on optical

(a) Effective PDE of a J-30020 SMA evaluation board.

(b) Comparison of SMA and SMTPA evaluation boards. An overvoltage of 3 V is applied, and the result of correcting the impact of the 50 Ω resistor is shown.
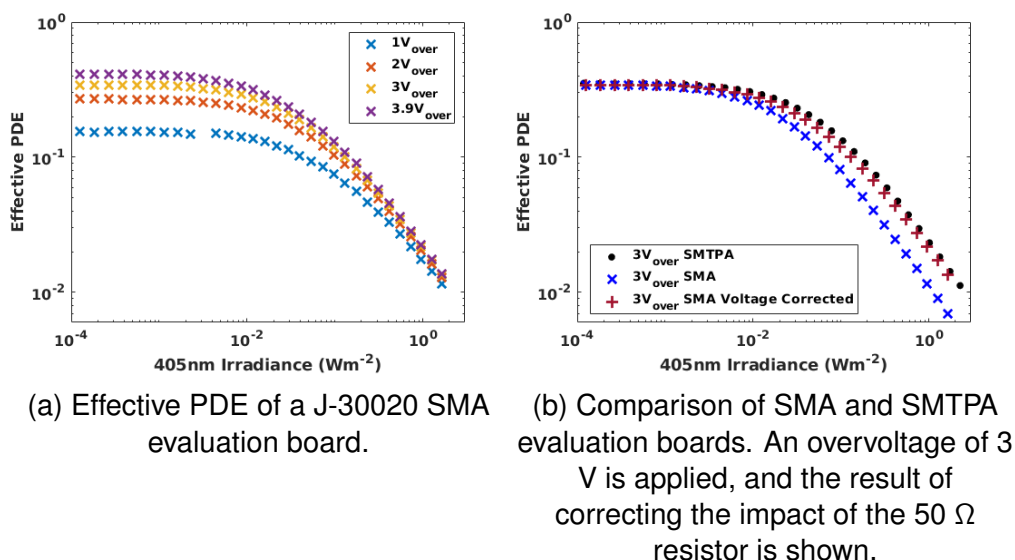
Figure 4.13: Effective PDE measurements using a 405 nm UV3TZ-15 LED ring irradiance source.

wireless links.

Correcting Effective Overvoltage

On the SMA evaluation board, the series 50 Ω resistor causes the SiPM's overvoltage to decrease. This is due to bias current from the SiPM causing a voltage drop over the series resistor. As the overvoltage on the SiPM determines (and is positively correlated with) the PDE and the charge for each microcell, any reduction in the overvoltage means the effective PDE will in turn decrease.

To remove the effect the resistor introduces, a negative feedback loop in MATLAB was used to keep the effective overvoltage on the SiPM constant. Figure 4.13b shows a comparison of the SMA board's effective PDE measurements, with and without the overvoltage correction. When the effect of the 50 Ω resistor was removed, the effective PDEs of the SMA and SMTPA boards closely agreed. This experiment shows the removal of the anode series resistor gives improved effective PDE performance. For operation in ambiently lit environments, this performance improvement is important and allows for the usage of a SiPM closer to an ideal device.

4.3.6 Comparison of Required Transmitter Irradiances for a VLC Links

SMA and SMTPA evaluation boards have been shown to have significant performance differences owing to the presence of a 50 Ω resistor in series with the SiPM. To understand the impact of the 50 Ω resistor on the transmitter power required to support a VLC link, experiments were performed to measure the required transmitter irradiance as a consequence of the ambient irradiance.

Experimental Setup

The same setup experimental as section 3.8 was used to perform data transmission experiments, with a some modifications. The signal from the AWG was amplified by a Fairview FMAM3269 amplifier to produce a 2 V_{pp} signal at the L405P20 laser diode. Since this amplifier has a band-pass beginning at 10 MHz, 8b10b coding was used to frequency shift the signal. This RF signal was combined with a DC bias of 35.5 mA in a Mini Circuits Bias-Tee ZFBT-4R2GW+, which was applied to a L405P20 laser diode. The light from the laser diode passed through a computer-controlled polariser. A ring of eight UV3TZ-15 LEDs was used as a background 405 nm irradiance source, which were controlled by a Keithley 224 source measure unit. The irradiance at the receiver was measured with an 818-UV calibrated photodiode. The receiver consisted of a SiPM, biased by a programmable bench power supply, and was cooled with a fan. The fast output was connected to a Mini Circuits ZX60-43-S+ 4 GHz amplifier, which was then connected to a Keysight MSO64 4 GHz oscilloscope. Finally, the BER was calculated and used as feedback to adjust the transmitter irradiance through automatically moving the polariser to achieve a target BER.

Figure 4.14: Schematic diagram of the experimental setup. Red arrows indicate optical paths. The significant difference to previous experimental setups is the ability to control through software the ambient light (provided by the LED) and transmitter irradiances (controlled by the polariser).

A computer-controlled polariser was designed to enable long experiments which search for a transmitter irradiance to support a given BER. Before this, no such method to regulate transmitter irradiance other than manually moving a polariser existed in the research group. Identifying the need for an automated high precision polariser, an assembly (visible in figure 4.15) was designed to finely control the power from the transmitter laser. Using a Overview Titan iBLDC motor with a step angle of $0.05°$, fine setting of the TX intensity was achieved. The Overview Titan motor required a I2C control signal and a fused power supply, these requirements were fulfilled by creating a circuit board to control the motor, visible in figure 4.15a.

The circuit board is simple, it routes a 12 V_{DC} power supply through a slow blow fuse to a flexible circuit board connector. Two I2C lines were also run to the connector (Clock and Data, SCL and SDA), which originate from an inexpensive ESP8266 evaluation board. These I2C lines are pulled high with 1.5 kΩ resistors. An ESP8266 micro-controller runs software written in C to interface with a computer over a serial connection. MATLAB code was then written to allow non-intrusive addition into existing scripts. To set an irradiance a binary search is performed while measuring the output of the transmitter with a 818-UV calibrated pho-

todiode. The addition of the polariser allowed for significant time to be saved as experiments manually adjusting a polariser to achieve a target BER typically take upwards of an hour to find a single desired irradiance. As Wi-Fi and telecommunications interference was a challenge for this experiment, the addition of the polariser allowed experiments to be automated for overnight running which mitigated the impact of RF interference. Additional information on the RF interference can be found in appendix A.

The assembly was designed to house the laser diode, which is fixed in place, followed by a static polariser, and then the motor controlled polariser. It was necessary to fix the laser diode in place, as the laser is polarised in its output, and any rotation of the laser would make the system not repeatable.
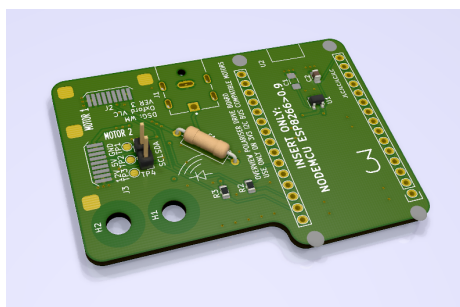
(a) Polariser driving board. Board uses I2C protocol to interface with the Overview Titan iBLDC motor.
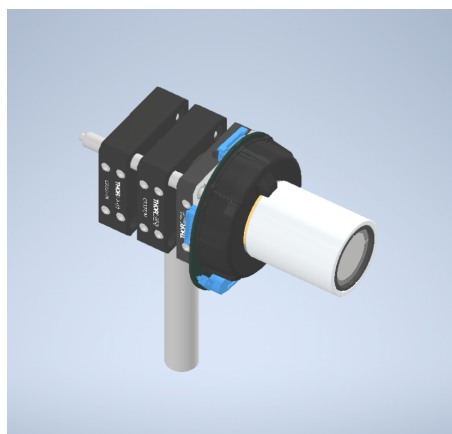
(b) Polariser assembly.

Figure 4.15: Polariser electronics and assembly.

Data Transmission Results

Data transmission experiments were performed over a distance of 40 cm, with a data rate of 500 Mbps. At this data rate, the SiPM experiences conventional ISI as each microcell has a FWHM pulse width of 1.4 ns. The presence of ISI required the use of DFE, before the BER was calculated, using 164,000 bits.

Ambient 405 nm light from the LED ring was used to illuminate the

SiPM at irradiances between 2 mWm^{-2} and 1 Wm^{-2} . The transmitter irradiance was then varied using a polariser, until the target BER of 3.8×10^{-3} (the 7% FEC limit [44]) was achieved for each ambient irradiance. To converge quickly on a solution, two trials are performed at transmitter irradiances a fifth of and identical to the background irradiance to gain information on the relation between BER, and transmitter irradiance. A third 'measurement' is granted by the assumption an infinitely small transmit irradiance causing a BER of 0.5. These measurements were fitted using a three-parameter complementary error function. The complementary error function was selected as it is the RF equivalent of the bit error rate (BER) for an OOK link [56]. Generalising this function allowed for the BER of VLC links to be approximated.

$$BER = a\mathrm{erfc}\left(b \cdot 10^L\right) + c \tag{4.6}$$

After fitting, the parameters a, b and c were used with the rearranged form of this model

$$L_{\mathrm{target}} = \frac{\mathrm{erfcinv}\left(\frac{\log_{10}(BER)-c}{a}\right)}{b} \tag{4.7}$$

to obtain the predicted transmitter irradiance (L_{target}) to support the link at the target BER of 3.8×10^{-3}. After L_{target} was calculated, the system varied the polariser to achieve the target transmitter irradiance at the SiPM. At this new irradiance, the BER was then measured, and this additional information was used to improve the fit on equation (4.6). The improved fit then provided a better estimate of the irradiance required to support the target BER. This process was repeated until the BER was $3.8 \times 10^{-3} \pm 0.3 \times 10^{-3}$. This fitting method sometimes failed as inverting the complementary error function provided no solution, so Newton-Raphson was used in place to iterate towards a solution.

On an initial experimental run, the results varied more between each
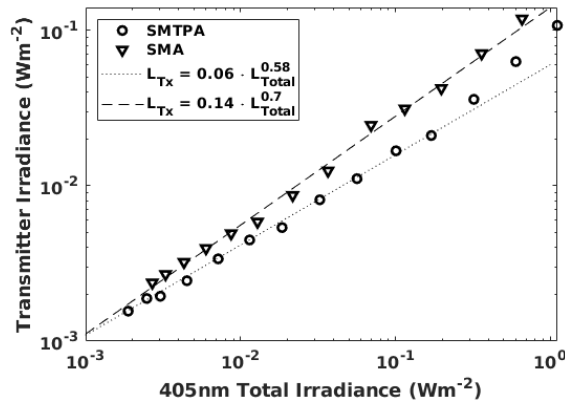
Figure 4.16: SMA and SMTPA evaluation boards supporting a 405 nm link at 500 Mbps with a BER of $3.8 \cdot 10^{-3}$

run than was expected by Poisson statistics. Detailed, careful examination of the frequency spectrum of the receiver output when the BER was unexpectedly high revealed the presence of Industrial scientific and medical (ISM) band, and mobile telephony RF signals. This demonstrated that the unexpectedly high BERs observed was due to coupling of RF signals into the SMTPA host PCB. An RF interference detector was written in MATLAB to determine if RF power was present on the receiver output, and if it was, the capture was discarded and the BER measurement performed again. More detail on this method and a deeper investigation of the interference are available in appendix A.

Figure 4.16 shows the SMA and SMTPA evaluation boards' performances under variable background irradiances. The required transmitter irradiance to support a link at a BER of 3.8×10^{-3} is plotted against the total irradiance falling upon the SiPM. The total irradiance is the sum of the ambient irradiance, and the irradiance from the transmitter. In the SiPM's worldview, it cannot distinguish between a photon from the transmitter and a photon from the background illumination source [50]. At 500 Mbps, the SMTPA board required a lower transmitter irradiance than the SMA board for all tested irradiances. This evidence of a higher performing receiver motivated using the SMTPA evaluation board as the receiver to use going forward.

4.3.7 Investigation of Fast Output Paralysability

Device saturation limits the performance of SiPM receivers, however little is known about the direct impact of device saturation on the required transmitter irradiance on VLC links. Passively quenched SiPMs have previously been assumed to be paralysable by other research groups [45]. However, the bias current flowing through the SiPM indicates that detections still occur, indicating the slow output wasn't paralysed in section 3.6. For the case of J-Series SiPMs, the fast output has been used for VLC, and so the possibility that it is paralysable was investigated.

The paralysable model in equation (3.9) predicts that a J-Series 30020 SiPM will achieve its maximum output pulse rate at 70 mWm^{-2} . With increasing irradiance, the predicted pulse rate then rapidly falls. An irradiance of 400 mWm^{-2} is predicted to have the same output pulse rate that 1 mWm^{-2} would stimulate. Surpassing 400 mWm^{-2} striking the SiPM would imply a link would not be able to be supported above 500 Mbps.

An experiment was performed where the SiPM was driven deep into its saturated region, by applying ambient interfering irradiances between 100 mWm^{-2} and 500 mWm^{-2} . The transmitter irradiance was fixed at 100 mWm^{-2} , and the data transmission rate was varied from 500 Mbps to 2 Gbps. These particular irradiances were selected as the paralysable model in section 3.6 predict that a link below the FEC limit would not be possible. For each data rate, the BER was measured. The same equipment setup as in section 4.3.6 was used, however using a J-30020 SMTPA SiPM.

Figure 4.17a again shows optical wireless links being supported under conditions that the paralysable hypothesis prohibits. Additionally, table 4.4 shows the selected background irradiances, the corresponding inter-photon times for a single microcell ($\tau_{\mathrm{interphoton}}$), and the paralysable model's equivalent detected irradiance. The mean detected inter-photon time for each microcell (also shown in figure 4.18) for all configurations

is below the microcell recharge time (approx. 2.2 τ_{recharge} periods. This means that these irradiances are high enough to cause paralysis if the fast output is paralysable. As VLC links could reliably be achieved, the J-30020 is non-paralysable, and output pulses are still generated on the fast output despite the detection of photons while the microcell is still recharging.

The results in figure 4.17a show that for a fixed transmitter irradiance, the minimum bit error rate that can be achieved increases with background irradiance. If a target bit error rate of $3.8 \cdot 10^{-3}$ (the 7% FEC limit [44]) is chosen, the maximum data-rate that can be supported decreases with increasing background irradiance. Despite this, with 100 mWm^{-2} transmitter irradiance and a 300 mWm^{-2} background irradiance, 1.35 Gbps can be supported, whereas the paralysable model claims this should not be possible. The conclusion of this experiment and those is section 3.6 is therefore that neither the slow or fast outputs of these passively quenched microcells are paralysable.

Table 4.4: Transmitter and Background Irradiance configurations for figure 4.17a

Tx Irrad.	Bg. Irrad.	$\tau_{\text{interphoton}}$	Equiv. Para. Irrad.
100 mWm^{-2}	100 mWm^{-2}	16 ns	16.7 mWm^{-2}
100 mWm^{-2}	300 mWm^{-2}	8 ns	1.9 mWm^{-2}
100 mWm^{-2}	500 mWm^{-2}	5.36 ns	0.0163 mWm^{-2}

4.3.8 Investigation of the Impact of SiPM Saturation on VLC Links

To quantify the impact of ambient light, another experiment was performed by fixing the target bit error rate to $3.8 \cdot 10^{-3}$, and setting a link data rate of 1 Gbps. The ambient interfering irradiance was varied, and the required transmitter irradiance to achieve the required BER was measured. Again, the same equipment setup as in section 4.3.6 was used. Figure 4.17b shows results for the 1 Gbps link, where the required transmitter irradiance, L_{Tx}, as a function of the total incident irradiance irradi-
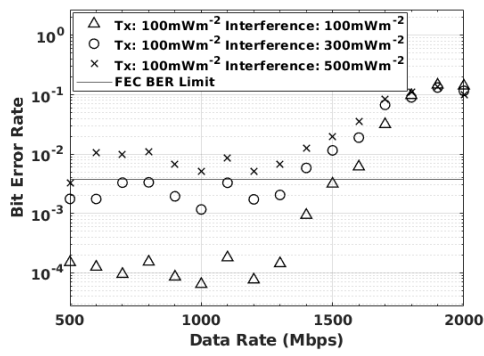
(a) Optical link at high irradiances.
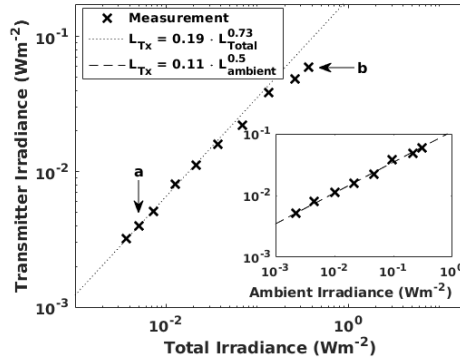
(b) Tx irradiance required to maintain an optical link with a BER of $3.8 \cdot 10^{-3}$ at 1 Gbps.
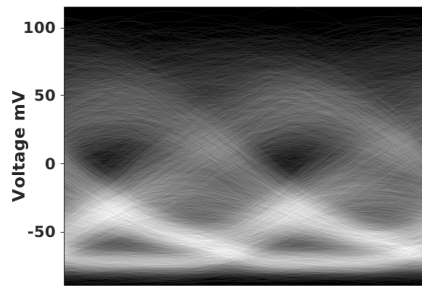
(c) Eye Diagram (Pre DFE) at Point A. Total of 6 mWm^{-2} of 405 nm irradiance.
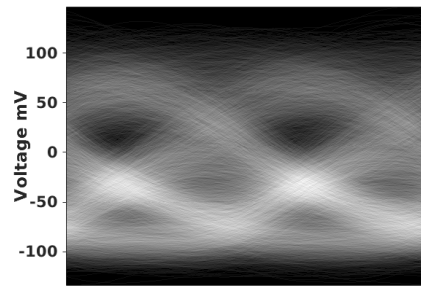
(d) Eye Diagram (Pre DFE) at Point B. Total of 470 mWm^{-2} of 405 nm irradiance.

Figure 4.17: J-30020 SMTPA optical links under high irradiances. $V_{\text{bias}} = 3$ V

ance, $L_{\text{Total}}(= L_{\text{Tx}} + L_{\text{Background}})$ was measured.

For total irradiances lower than 50 mWm^{-2} , the relationship between the transmitter irradiance and the total irradiance, L_{Total} is

$$L_{\text{Tx}} = 0.19 \cdot L_{\text{Total}}^{0.73} \tag{4.8}$$

At higher total irradiances, the irradiance from the transmitter becomes a significant part of the total and this relationship is no longer valid. The inset in figure 4.17b shows results for the 1 Gbps link, where the required transmitter irradiance as a function of background irradiance, $L_{\text{Background}}$, follows a power law,

$$L_{\text{Tx}} = 0.11 \cdot L_{\text{Background}}^{0.5} \tag{4.9}$$

For any communications link, to maintain a specific BER, the SNR
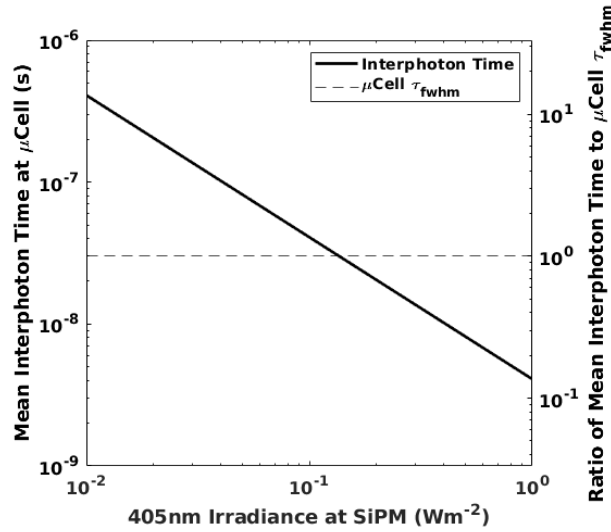
Figure 4.18: Inter-photon arrival times at a single microcell on a J-30020 SiPM against 405 nm irradiance.

must remain constant. Incident photons introduce shot noise, due to the fact their inter-arrival time is exponentially distributed. For photons, the shot noise scales as the square root of the incident irradiance. Consequently, the SNR from shot noise is proportional to

$$SNR \propto \frac{L_{Tx}}{(L_{Tx} + L_{Background})^{0.5}} \tag{4.10}$$

When the measured power law relation is substituted into the SNR equation,

$$SNR \propto \frac{L_{Tx}}{\left(L_{Tx} + \left(\frac{L_{Tx}}{0.11}\right)^2\right)^{0.5}} \propto L_{Tx}^{0.5} \tag{4.11}$$

This observation is consistent with the dominant noise source being shot noise in the number of detected photons. This power law, is the one that would be expected if the dominant noise source in the SiPM receiver is shot noise from the ambient light. More surprisingly, this relationship applies in both the linear and the saturated regions of irradiance.

Despite the non-linearity present at total irradiances above 10 mWm^{-2}, the SiPM does not suffer a performance detriment as irradiance increases. This is due to the effective PDE decreasing and affecting both the interfering ambient, and signal photons equally. The results pre-

sented show the J-30020 SMTPA SiPM can support a 1 Gbps link when exposed to a total irradiance of 470 mWm^{-2} in figure 4.17b, with a clear eye diagram visible in figure 4.17d.

Interestingly, when eye diagrams are compared for two vastly different irradiance configurations, the diagrams change very little. Eye diagrams of points 'a' and 'b' on figure 4.17b, corresponding to 6 mWm^{-2} and 470 mWm^{-2} of total 405 nm irradiance, are shown in figure 4.17c and figure 4.17d. Despite having a signal power over an order of magnitude higher, the peak to peak voltage does not change proportionately, changing from 125 mV$_{pp}$ to 200 mV$_{pp}$ which is a ratio of 1.6. Additionally, no significant changes in bit shape occur, only a higher level of noise is present on the 470 mWm^{-2} eye diagram most clearly seen in the zero level. This lack of significant change of peak to peak voltage is explained by the change in effective PDE. The ratio of transmitter powers between points 'a' and 'b' is $\frac{L_a}{L_b} \propto \frac{4Wm^{-2}}{60Wm^{-2}} = \frac{1}{15}$. When predicting the effective PDE of points 'a' and 'b' using figure 4.13b, the ratio of PDEs $\frac{\eta_{eff_a}}{\eta_{eff_b}} \approx \frac{0.34}{0.042} \approx 8.1$ when multiplied by the ratio of transmitter powers gives an expected peak to peak voltage ratio of 1.8.

4.4 Poisson Statistics with VLC Under Ambient Illumination

SiPMs are limited by Poisson statistics. Section 1.7 detailed a formula for the BER of a link as a consequence of the detected signal and background photons, which is repeated here for convenience:

$$\text{BER} = \frac{1}{2}\left[\underbrace{\sum_{k=0}^{n_T} \frac{(n_a + n_s)^k}{k!}e^{-(n_s+n_b)}}_{\text{Tx'd 1 detected as 0}} + \underbrace{\sum_{k=n_T}^{\infty} \frac{n_a^k}{k!}e^{-n_a}}_{\text{Tx'd 0 detected as 1}}\right] \quad (4.12)$$

where n_s and n_a are detected signal and ambient photons per bit, with a decision threshold of n_T photons per bit.

To maintain a constant BER of $3.8 \cdot 10^{-3}$, equation (4.12) was used to determine the required transmitter power for different numbers of background photons per bit. Figure 4.19a (repeated from figure 1.4) shows the required detected photons per bit from the transmitter as a function of the interference photons per bit. More importantly the total detected photons per bit is shown in figure 4.19b. This is the SiPM's worldview as it cannot distinguish between a photon from the transmitter and a photon from the background irradiance. As more interference photons per bit are detected, the required detected signal photons per bit line trends to a power law of $L_{background}^{0.5}$.

In the SiPM's worldview of total detected photons per bit, the required signal photons begins at the minimum number of photons per bit to support the link, where the total detected photons per bit equals the signal photons per bit. As the background photons per bit increases, the slope of the line also trends to a power law of $L_{background}^{0.5}$, as the background becomes dominant over the signal when considering the total irradiance.

To investigate how the J-30020 SiPM compares to this Poisson-theory model, results were gathered for a fixed BER of $3.8 \cdot 10^{-3}$ where the ambient irradiance was swept between 0.1 mWm⁻² and 200 mWm⁻² , and the required transmitter irradiance to support the link was measured. Three data rates were selected, 500 Mbps, 1 Gbps and 1.5 Gbps. Again, this experiment was performed using the same experimental setup as section 4.3.6. The transmitting laser configuration was not able to produce a perfectly dark LOW symbol The ratio between a HIGH and a LOW symbol's irradiance was measured to be approximately 4, and the DC irradiance present from the laser's LOW symbol was hence added to the ambient irradiance. Figure 4.20 shows measurements of the optical link, after incorporating the impact of the transmitter extinction ratio. Figure 4.21 shows these same results, but in terms of detected photons per bit. The results in figure 4.21a show that links at 1.5 Gbps required
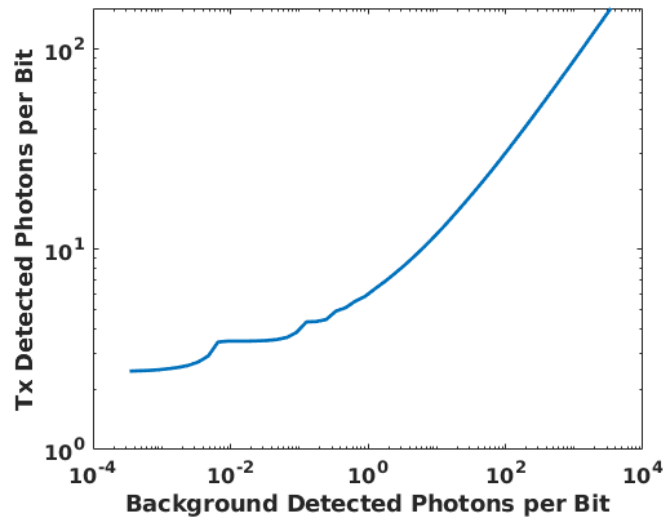
(a) Required detected signal photons per bit-time vs
background detected photons per bit-time.
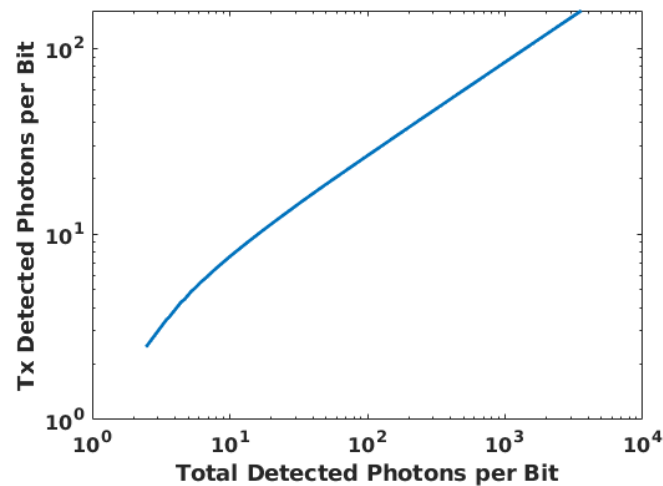
(b) Required detected signal photons per bit-time vs
total detected photons per bit-time.

Figure 4.19: Poisson Statistics model to support a BER of $3.8 \cdot 10^{-3}$.

a greater number of detected photons per bit than the other lower data-rates. This requirement may be explained as a decision feedback equal-isation power penalty, as the fast output pulse width is approximately 2.1 times the bit-time. For these experiments the transmitter design, rather than the J-30020 SiPM receiver, limits the lowest irradiance that can be achieved. For data rates of 500 Mbps and 1 Gbps, the required number of detected signal photons per bit as a function of the ambient detected photons per bit closely agrees with the Poisson-theoretical model until approximately 100 photons per bit. When the number of background de-

tected photons per bit increases above 100, there is a penalty on the transmitter, requiring more photons than Poisson theory predicts. This penalty may be due to the effective PDE (described in section 4.3.5) decreasing at higher transmitter irradiances. Despite these considerations, the Poisson-theory model agrees with measurements and holds predictive power for data rates without a significant DFE power penalty, until the total number of detected photons per bit is 100.

In section 4.3.5, it was shown that the effective PDE of a SiPM begins to deviate from the PDE as the irradiance increases. For data rates of 500 Mbps and 1 Gbps, the irradiances corresponding to 100 photons per bare 10.4 mWm^{-2} , and 5.2 mWm^{-2} . For each of these irradiances, the reduction in effective PDEs are 14% and 11%. The reduction in effective PDE means that fewer photons per bit are detected. Any decrease in the number of detected photons means a higher transmitter power is required such that enough photons per bit are detected to achieve the same signal to noise ratio. Therefore it is sensible that the Poisson statistics driven model begins to break down, when the change in effective PDE becomes significant.

4.4.1 Eye-Safe Transmitters and Improving Receiver Performance

Ali et al. describe an eye-safe array of transmitters in a typical office environment, at a wavelength of 405 nm. An eye-safe (Risk Group 0) transmitter has been described in previous work with a 3 m diameter of coverage. This transmitter delivers 3 mWm^{-2} of 405 nm irradiance to a user, which sets a target optical irradiance to work within for SiPM receivers.

Figure 4.20a shows for a transmitter power of 3 mWm^{-2} , the maximum ambient irradiance that can be tolerated is 15 mWm^{-2} for 500 Mbps, 8 mWm^{-2} for 1 Gbps, and 2 mWm^{-2} for 1.5 Gbps. These irradiances set constraints on the maximum permissible 405 nm equivalent irradiances
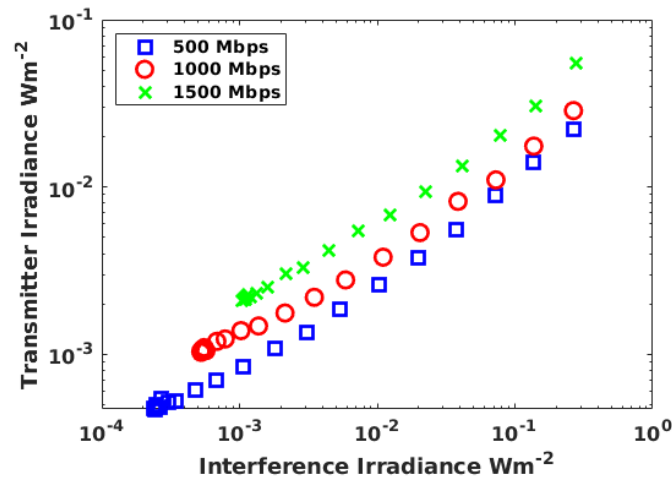
(a) Required 405 nm transmitter irradiance against ambient irradiance.
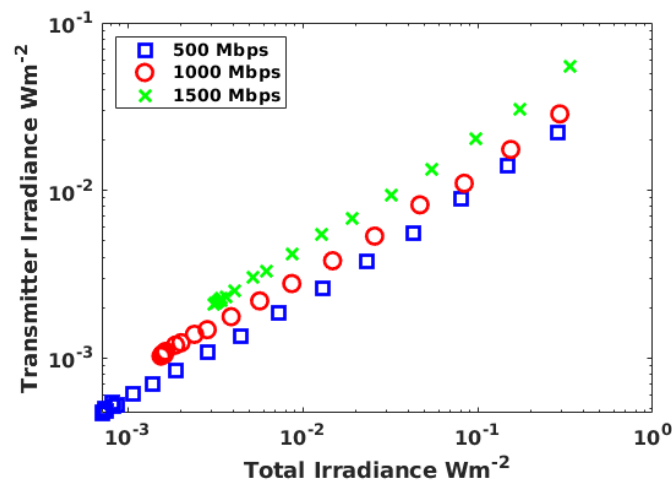
(b) Required 405 nm transmitter irradiance against total irradiance.

Figure 4.20: Required 405 nm transmitter irradiance as a consequence of ambient and total interference striking a J-30020 SMTPA, at a BER of $3.8 \cdot 10^{-3}$.

that can be present when operating a link. This result shows that background light must be carefully considered and controlled when using a SiPM as an optical receiver in a real environment, in order to support a high-speed optical wireless link.

The Poisson-theory model shown and validated above also allows for device parameters to be changed, and transmitter irradiance requirements predicted. The number of detected photons per bit is a limit that is identical for any Poisson-limited detector, but the transmitter irradiance is limited by eye safety standards and practical transmitter design to 3 mWm^{-2} [12]. One possible way of detecting more photons per bit at the
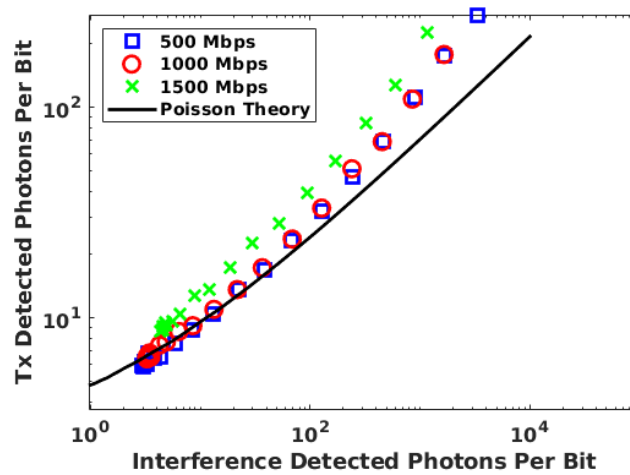
(a) Detected signal photons per bit measured against detected interference
photons per bit.
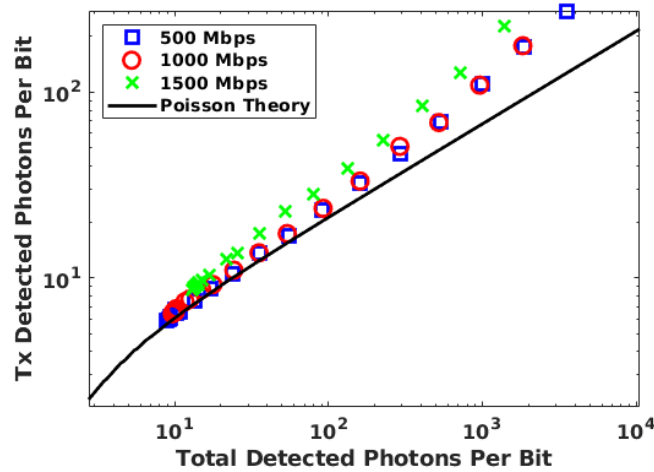
(b) Detected signal photons per bit measured against total detected photons
per bit.

Figure 4.21: Photons per bit required for 405 nm VLC links compared
with Poisson statistics model for a J-30020 SMTPA, at a BER of
$3.8 \cdot 10^{-3}$.

same irradiance is by increasing the area of the detector.

Using SMTPA evaluation boards, it is possible to combine multiple
SiPMs together on a circuit board and add their output signals together.
This creates a receiver, which has a larger area without changing the
output pulse width. The Poisson-theory model was hence used to pre-
dict the performance improvement of adding eight SiPMs together, and
comparing them to a single unit.

Under the assumption eight SiPMs are added together in parallel, fig-
ure 4.22 shows the predicted required transmitter irradiance as a function

of the interfering background irradiance when operating at a data rate of
500 Mbps. The ratio of required signal irradiances for each background
irradiance is also plotted.

In the case that ambient light cannot be avoided, and by using a
stricter 1 mWm^{-2} transmitter limit, a single SiPM can tolerate 1.5 mWm^{-2}
of background irradiance while maintaining a VLC link at a BER of $3.8 \cdot$
10^{-3}. However when summing eight SiPMs together, the Poisson-theory
curve in figure 4.22 suggests a background irradiance of 20 mWm^{-2} can
be tolerated, which is a ratio of 13 to that of a single SiPM. This im-
provement motivates adding together multiple SiPMs to have a receiver
with a larger area, which allows for tolerating higher irradiances of back-
ground light, or in the case of low background irradiance, the possibility
of achieving higher link rates from the increased maximum count rate.

At low background irradiances (below 10^{-8} Wm^{-2}), the ratio of re-
quired transmit irradiances between one and eight SiPMs is $\frac{1}{8}$. As the
background irradiance increases, this ratio increases towards $\frac{1}{\sqrt{8}}$. This
low background irradiance requirement for the greater performance ben-
efit means that additional filtering, and a transmitter with a low EXR is
required to achieve this benefit. While the performance benefit at higher
background irradiance is less favourable than the performance benefit at
lower background irradiances; the combination of multiple SiPMs may al-
low for SiPMs to operate in environments of high background irradiances
with an eye-safe transmitter.

Circuit Board Design

Onsemi provide an application note which suggests a method of adding
multiple SiPM receivers together using *Signal Driven Multiplexing* (SDM)
[57]. Figure 4.23 shows a schematic diagram of this idea, where Sky-
works SMS7621 24 GHz Schottky diode pairs are used to combine the
outputs of four SiPMs. In this circuit, the SiPMs are biased by connect-
ing a bias voltage, Vbias, to their cathode. The fast output of each SiPM
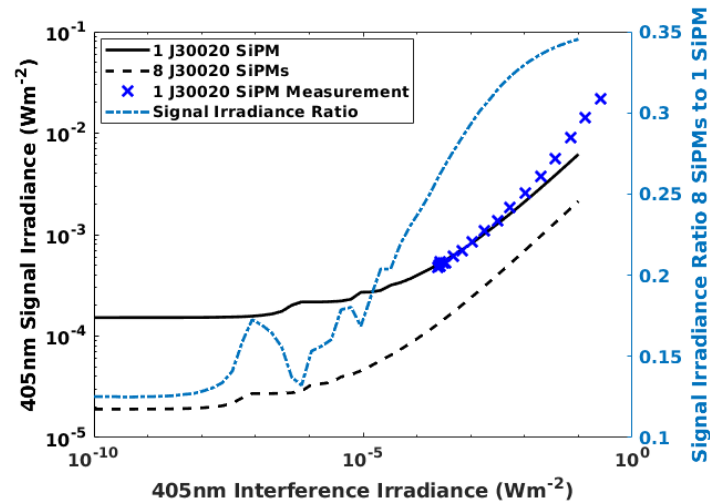
Figure 4.22: Poisson-theory model showing irradiance requirements of
a single SiPM, and eight SiPMs added together at 500 Mbps.

connects to the middle of a Schottky diode pair, which are forward biased
by the bias source, Vss, such that a current of approximately 1 mA flows
through each schottky pair. An output pulse on the fast output causes the
voltages on each side of the diode pair to change, which consequently
changes the diode pair's bias current. By injecting signal currents onto
a common readout line, each SiPM's response is added together. This
approach means a single SiPM's fast output is unable to affect the fast
outputs of other SiPMs connected to the common readout line, as the
currents add together. Any variation in this total current is converted into
a voltage by the resistor connected to Vss. The high-frequency content
of this voltage passes through a capacitor to Fast+, which is the shared
output from all of the SiPMs. The resistor allows for gracefully setting
Vss to achieve the 1 mA per diode pair by creating an operating point.

A four-layer printed circuit board (PCB), shown in figure 4.24 was
designed with the goal of implementing SDM with the SMTPA evaluation
board, with a maximum design frequency of 5 GHz and 50 Ω traces on
the common readout line. The same electrical principle in figure 4.23
was used, but expanded up to nine SiPMs. Decoupling capacitors were
included to to ensure a stable power supply up to 5 GHz for each SiPM
at the RF connector. The SiPM detectors required cooling which was
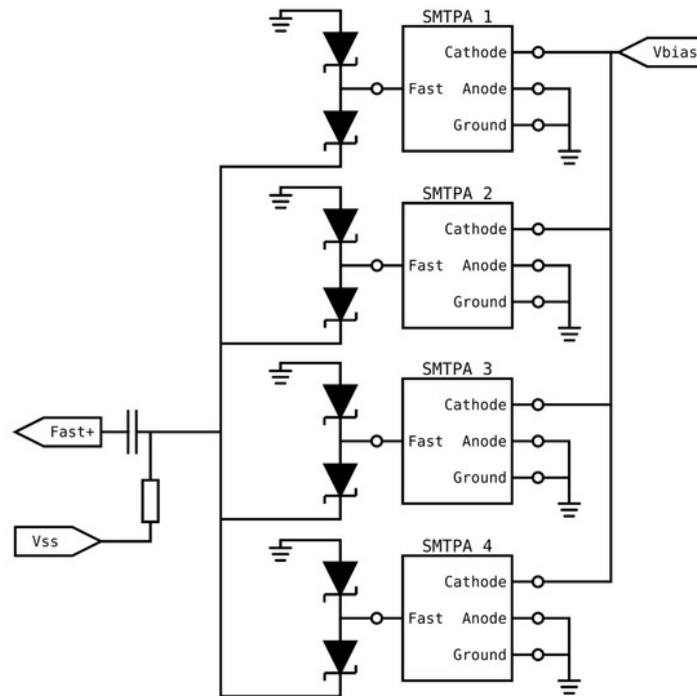
Figure 4.23: Signal-Driven Multiplexing of SiPMs schematic.

supplied by a 40 mm server fan, whose airflow was directed by a 3D
printed duct.
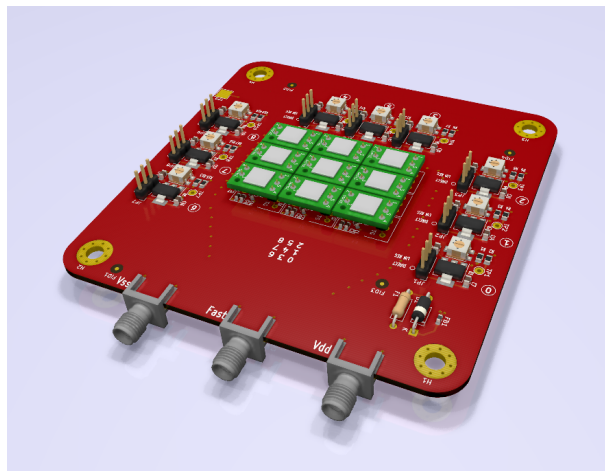
Figure 4.24: The designed receiver which allows for the addition of
multiple SMTPA SiPMs.

Experimental Setup and Results

Due to one of the detectors becoming damaged, the receiver, which
was designed to host nine SiPMs, was only used with eight SiPMs. The
same equipment setup as in section 4.3.6 was used, with an additional
power supply added to provide the forward diode bias for the SDM cir-
cuitry. To test the SDM circuit, a 500 MHz sine wave was output from the

laser diode and illuminated the SiPM at 5 mWm^{-2} . As the current flowing through the SDM circuit increased, the peak to peak voltage measured consequently increased until approximately 5 mA, where an increase in bias current did not change the peak to peak voltage. The current-controlled supply was consequently set to supply the recommended 1 mA per diode pair (9 mA total) to the SDM circuit, and an optical wireless link was established. The same experiment as in section 4.4 was performed to have comparable results and the irradiance correction used in section 4.4 was also applied to this experiment.

The results shown in figure 4.25 show that a larger area is beneficial in terms of a lower irradiance to support a data rate, and the maximum tolerable background irradiance when the transmitter power is limited. However, the predicted benefits were not achieved with the particular implementation. By fitting a line by least squares for measurements between 1 Wm^{-2} and 30 Wm^{-2} , the ratio of irradiances required (1 vs 8) is 2.32, however the worst-case predicted ratio is $\sqrt{8} \approx 2.82$.

For the case where the transmitter power is limited to 3 mWm^{-2} , the single SiPM was able to accept 15 mWm^{-2} of ambient irradiance. Eight SiPMs summed together were able to accept a maximum of 48 mWm^{-2} , which is a factor of 3.2 improvement. This important result shows a how larger receivers can be constructed from multiple SiPMs, which allow for operation in harsher environments, within eye safe limitations.

4.5 Discussion

Ambient light has a significant penalty on the performance of SiPMs as optical wireless receivers. A new form of ISI was documented, which is caused by the irradiance falling on the SiPM over the period of a micro-cell's recharge time in the past. The history of the irradiance impacts how many microcells are recharging, and hence changes the effective PDE of the SiPM with time. A change in the effective PDE means the number of detected photons will change, which causes the newly observed non-
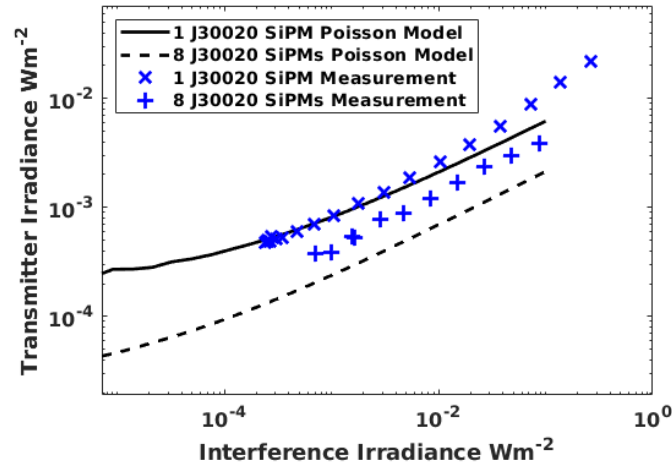
Figure 4.25: Comparison of transmitter irradiance required to support 500 Mbps with 1 J-30020 SiPM with and 8 J-30020 SiPMs added using SDM.

linear behaviour. DFE and LEQ were shown to be able to mitigate the impact of this effect.

The 50 Ω series anode resistor present on the most commonly used evaluation boards for SiPMs has detrimental effects. The presence of the resistor increased the recharge time, which had a negative impact on the max count rate. The effective PDE was also negatively impacted at high irradiances. In addition, any voltage drop across the resistor reduces the maximum effective overvoltage and hence the max PDE. The performance benefit of removing the resistor was reflected in measurements taken, which showed a power law reduction in the required transmitter power to support a particular total irradiance $L_{\text{Tx}} \propto L_{\text{Total}}^{0.7}$ to $L_{\text{Tx}} \propto L_{\text{Total}}^{0.58}$.

This leads to requiring higher transmitter powers to maintain the same signal to noise ratio than a device without the resistor present. The effective PDE of SiPMs was investigated, and applied to explain peak to peak voltages of eye diagrams. Microcell paralysability was investigated, which showed that the J-Series 30020 SiPM is *not paralysable on the fast output*, backing up initial results from section 3.6. The voltage-dependant PDE of SiPMs was also measured, and a model was fitted.

A Poisson-statistics model was compared with measurements of an optical wireless link using a SiPM receiver. This model was also used

to predict the performance of a theoretical receiver which adds together multiple SiPMs to have a larger detection area, allowing for performance improvements. SiPMs were then demonstrated to able to be added together to form a detector with a larger area, and consequently be robust to higher irradiances of ambient light when limited by a fixed transmitter irradiance. Since SiPMs are able to operate in the Poisson-limited regime, higher irradiances cause a performance penalty which should be avoided for the highest performance possible. Operation of SiPMs in ambiently lit environments is not a solved problem. However, a greater understanding of the impacts of ambient light on SiPMs, and the realisation of versatile SiPM receivers which are robust to higher levels of ambient light paves the way towards using SiPMs as VLC receivers in ambiently lit environments.

Chapter 5

Monte-Carlo Modelling of SiPM Receivers

5.1 Overview

Current SiPMs are giving promising results as VLC receivers. However, optimising their design for VLC experimentally would be a long, expensive programme. Furthermore, experiments are difficult to perform, as environmental conditions must be controlled to ensure repeatability. These factors mean that modelling will have an important role. However, current models assume that these microcells are paralysable [45] and this has been shown to be an invalid assumption in section 3.6 and section 4.3.7. To avoid making any assumptions, a Monte Carlo (MC) simulation model was developed. This has the additional advantages in all parameters being observable, allowing for the ability to measure key parameters under saturation.

This model is shown to agree with bias current measurements, displaying emergent SiPM saturation, and is further verified by replicating previous observations [51]. The model then is used to explain why the effective PDE as a consequence of incident irradiance rolls off at 20 dB per decade. Data transmission simulations are hence performed and the model is shown to closely agree with measurements. A correction factor

is found to predict the required transmitter power to sustain a link when the SiPM is saturated. With the key understanding of how microcells operate demonstrated, this work shows a pathway towards the development of specific pre- or post-equalisers for SiPMs as VLC receivers.

5.2 SiPM MC Simulation

Simulations in this work were implemented using a combination of MATLAB script and a C++ program. The C++ program generated a simulated SiPM fast output and bias current, when provided a list of expected number of photons arriving per time step.

This MC simulation allowed access to internal, typically hidden variables which included:

- The proportion of microcells that are fully charged.

- The mean PDE of the entire array for each time step.

- The mean cell charge for any microcells that fire on that time step.

- A time domain store of a microcell's charge.

The simulation code listings for the photon detection event logic and microcell recharge logic are available in appendix B, along with complexity analysis and additional implementation detail.

This simulation is able to simulate the fast output of a SiPM, and the bias current under irradiance which varies with time. This makes the simulation useful for predicting the performance of SiPMs in VLC links, as well as understanding the mechanics behind SiPM saturation. VLC links are not the only application for SiPMs, and the simulation is also useful for understanding the performance of SiPMs in other applications, such as medical imaging. Situations where the output of a SiPM is required to be known, and only the incident expected photon rate is known, are suitable for this simulation, meaning the simulation is fairly general.

5.2.1 MC Simulation Description

Before simulation occurs, the simulation is initialised through arguments which define device parameters. Once a simulated SiPM object is initialised, an array of expected number of photons per time step is passed through a function call (`SiPM.simulate(lightArray)`) to begin simulation.

A flow chart of the simulation is shown in figure 5.1, and photon detection event logic is shown in figure 5.2. For each time step, the simulation takes the input *expected* number of photons striking the detector, and Poisson samples it to randomly determine the number of photons actually striking the SiPM. To determine which microcells are struck, the Poisson sampled number of photons striking the SiPM is then used to determine how many random uniform samples are drawn. Photons are uniformly distributed over the entire SiPM, each microcell is equally likely to have a photon striking it (this process is still Poisson). The samples drawn dictate the indexes of the microcells which are struck by a photon. The same microcell may be struck multiple times in a single time step.

When a microcell is struck, the time since the last detection is calculated. The time since the last detection is then utilised to determine the microcell's voltage (and hence charge), and PDE. A uniform random distribution between zero and one is sampled, and is compared against the photon detection efficiency to determine if a detection occurs.

If a detection occurs, the current charge of the microcell is added to the output, and the time when a detection occurred is set to the current simulation time. Once all struck microcells have been considered, the simulation continues with the next time step, repeating the process until the input array of expected photons per time step has been depleted.

Finally, once the simulation has concluded and an array of output charge per time step has been generated, the output is convolved with a Gaussian kernel with a width of 1.4 ns, which is consistent with the

output pulse width of the J-30020 SiPM's fast output. The parameters used for the simulation can be found in table 5.1.

Table 5.1: Simulation Parameters for a J-30020 SiPM

Parameter	Value
N_{cells}	14410
$\tau_{recharge}$	$2.2 \cdot 14$ ns
A_{SiPM}	9.98 mm^2
C_{cell}	$4.6 \cdot 10^{-14}$ F
$\eta(\lambda, V_{over})$ (PDE)	Equation (4.4)
$V_{breakdown}$	24.5 V
V_{bias}	27.5 V
Timestep (dt)	$\min(0.1$ ns$, \frac{T_{Bit}}{20})$

5.2.2 Microcell voltage and PDE in Simulation

Calculating the microcell voltage (and hence charge) and PDE involve exponentials which are computationally expensive, so the simulation is initialised with lookup tables, which convert the time since last detection to voltage and PDE. The voltage is calculated using a standard RC time constant capacitor recharge equation.

$$V_{microcell} = (V_{bias} - V_{breakdown}) \cdot \left(1 - \exp \left(\frac{t - t_{last\ detection}}{\tau_{recharge}} \right) \right) \qquad (5.1)$$

where $V_{microcell}$ is the voltage of the microcell, V_{bias} and $V_{breakdown}$ are the bias and breakdown voltages, t is the current simulation time, $t_{last\ detection}$ is the last time a photon was detected for a specific microcell, and $\tau_{recharge}$ is the microcell recharge time. The microcell voltage can be converted to a charge through $Q = CV$, from knowledge of the microcell capacitance.

The PDE is calculated using the model from equation (4.4) in a more general form,

$$\eta(V_{over}) = \eta_{max} \left(1 - \exp \left(\frac{-V_{over}}{V_{chr}} \right) \right) \qquad (5.2)$$

where η_{max} is the maximum possible PDE achievable by the APD at a specific wavelength, and V_{chr} is a characteristic voltage for the APD.

Figure 5.3 shows how the microcell overvoltage and PDE evolve with time. These quantities are stored in individual lookup tables.
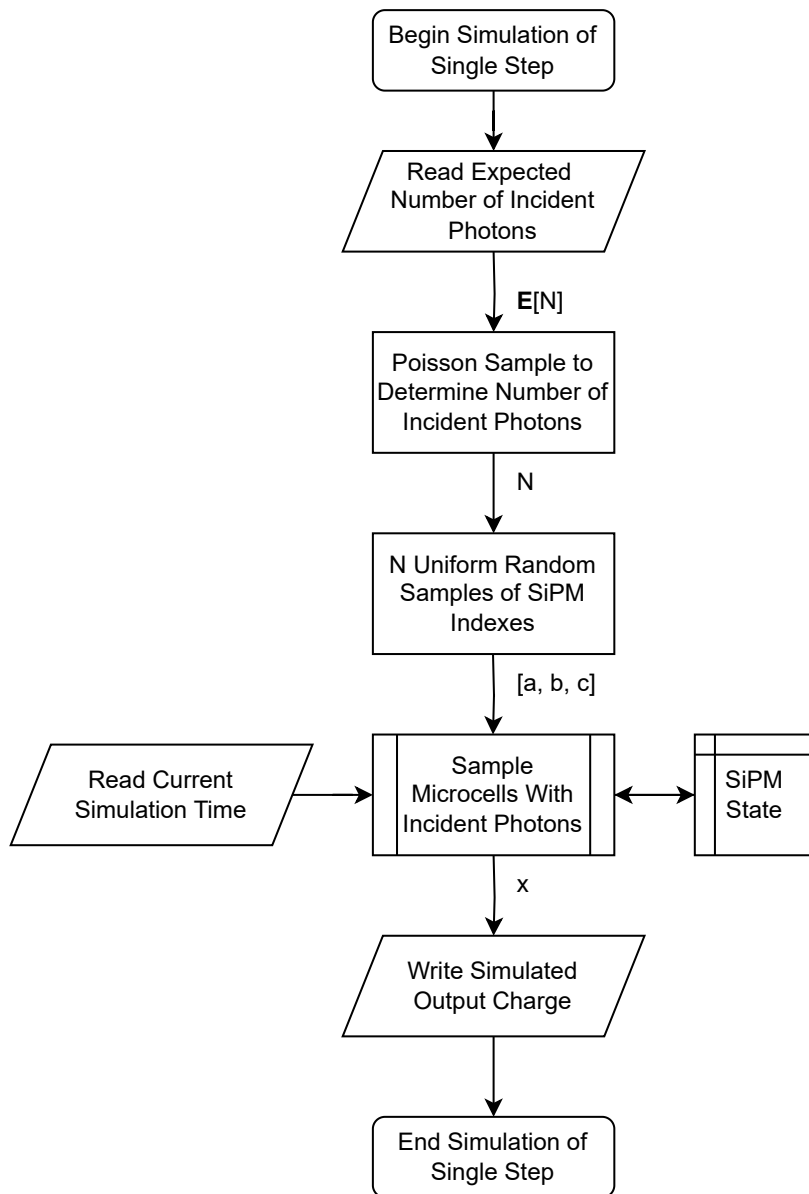
Figure 5.1: Flow chart of the MC simulation.
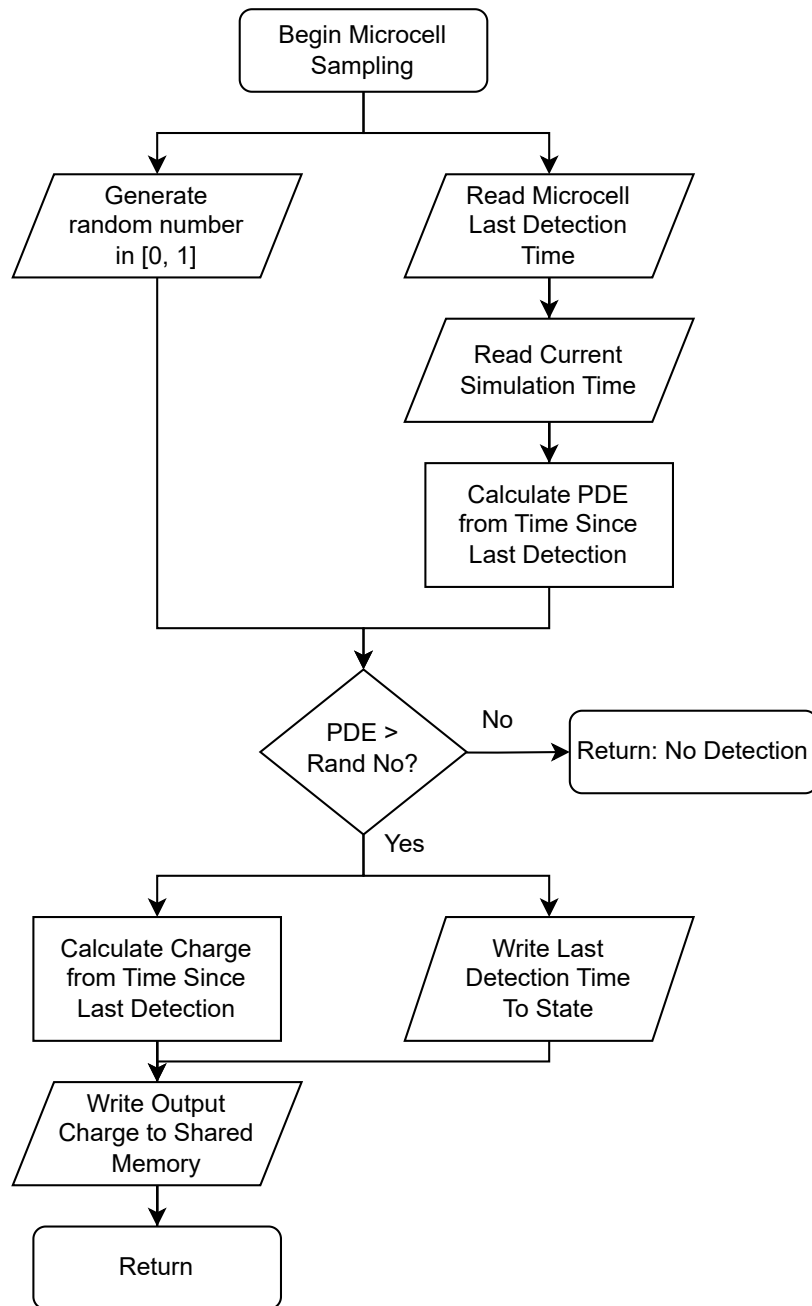
Figure 5.2: Flow chart of the photon detection event logic inside the microcells.
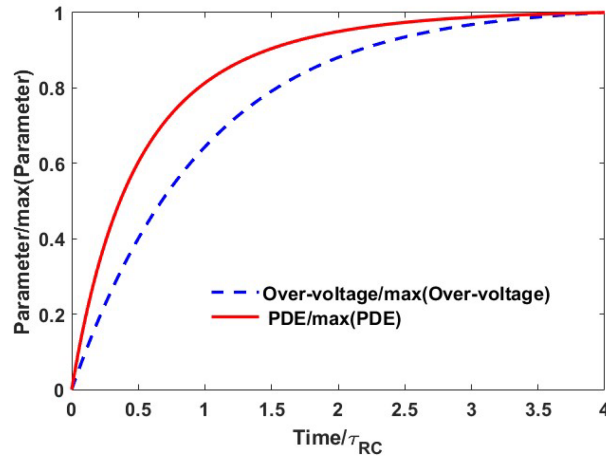
Figure 5.3: Recovery of overvoltage and PDE when determined by equations equation (5.1) and equation (4.4).

5.2.3 Simulation Initialisation

To initialise the SiPM simulation, the times since the last detection of a photon must be initialised for each microcell. In order to find reasonable random time samples to initialise with, the distribution of times since the last photon was detected was required.

The time between photon arrivals at the detector are exponentially distributed, which has the probability density function (PDF):

$$f_\gamma(t; \Lambda) = \Lambda e^{-\Lambda t} \tag{5.3}$$

where Λ is a rate parameter for the expected number of photon events per second, t is time in seconds, and f_γ is the probability density function for inter-photon times.

Given that microcells must recharge after detection, and that immediately post-detection the photon detection efficiency $\eta = 0$ means that the probability density function of the microcell inter-detection time must has a boundary condition at zero time $f(0; \Lambda) = 0$. This boundary condition means that the PDF for inter-detection times must be a different to an exponential distribution.

As shown in equation (4.4), the photon detection efficiency depends on the microcell overvoltage, which further depends on the time since

last detection. $\eta(V_\mu(t))$ modifies the shape of exponentially distributed inter-photon arrival times to form a new distribution of the inter-detection times, which is a renewal process. The renewal process PDF of inter-photon detection times was derived in appendix C, and is repeated here for convenience

$$f_\mu(x; \Lambda) = \eta(V_\mu(x))\Lambda e^{-\Lambda x p_\mu(x)} \tag{5.4}$$

where

$$p_\mu(t) = \frac{1}{t} \int_0^t \eta(V_\mu(t))dt \tag{5.5}$$

While useful, this distribution does not enable drawing samples for some random stopping point in time, to initialise the simulation. For some random stopping point in time, the probability density function for time since last detection (rather than inter-detection) can be calculated by the following:

$$f_s(t) = \frac{\int_t^\infty f_\mu(t)dt}{\int_0^\infty \int_t^\infty f_\mu(t)dtdt} \tag{5.6}$$

$f_s(t)$ is sampled at simulation initialisation, using the mean Λ for all the light input.

A method to check if this approximation is valid is providing a constant photon input rate and observing the output if any transients exist.

To check this analytically derived distribution, simulations were run using an incoming photon rate of 1.44 GCps on a J-30020 SiPM, and the inter-detection times were recorded. For this simulation, the SiPM was initialised with a time since last detection of zero for all microcells. Figure 5.4 shows results of comparing an exponential distribution, and the renewal process f_μ against simulation results. This figure shows strong agreement between the simulation and the renewal process, and further agreement between the solution for a random stopping point f_s and the simulation.
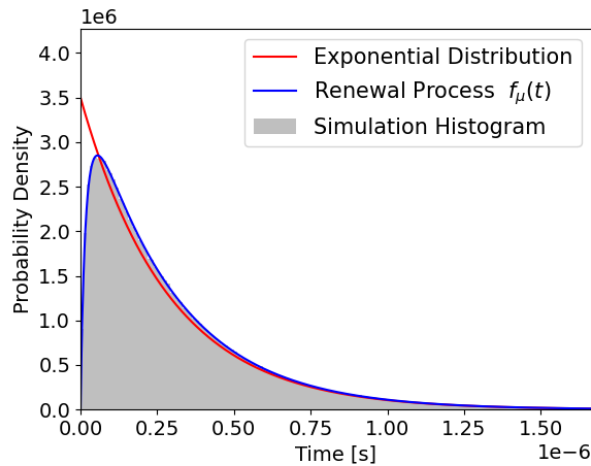
(a) Inter-detection time probability density function $f_\mu(t)$ compared to simulation and an exponential distribution.
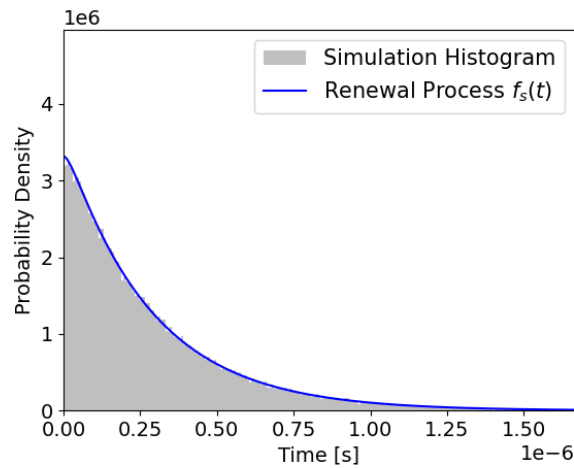
(b) Time since last detection for a random stopping time probability density function $f_s(t)$ compared to simulation.

Figure 5.4: Analytically derived functions compared to simulation. Both cases use SiPM parameters for a J-30020 SiPM (detailed in table 5.1), and a DC light source with 144 billion photons per second striking the detector.

5.3 Simulation Verification

5.3.1 Replicating SiPM Recovery Behaviour

The MC simulation was used to simulate a single 20 μm microcell, and the microcell voltage was recorded. A simulation was run for 1 μs, with a constant irradiance of 0.1 mWm^{-2} of 405 nm light. Results in figure 5.5 show that the microcell voltage recovers exponentially, as expected. This is a useful result, as it shows that the simulation is able

to replicate the recovery behaviour of a single microcell, which is a key aspect of SiPM operation. SiPM instantaneous bias current (the slow output) is proportional to the change in microcell charge (cell voltage multiplied by capacitance), and hence the recovery behaviour of a single microcell is important for understanding the slow output of a SiPM. The fast output of the SiPM is proportional to the fired microcell charge, and hence the recovery behaviour of a single microcell is important for understanding the fast output of a SiPM.

By using the MC model to 'see inside' a microcell, the simulation provided the ability to understand the mechanics behind SiPM operation under saturated conditions. An immediate consequence of this is shown in figure 5.5, which shows a simulated time domain response of a single microcell, highlighting the fact that a microcell can detect a photon while it is mid-recharge. This is equivalent to the microcell being biased with a lower overvoltage, which has a PDE and gain detriment. The microcell voltage and PDE are plotted, which shows the PDE recovering faster than the microcell charge.
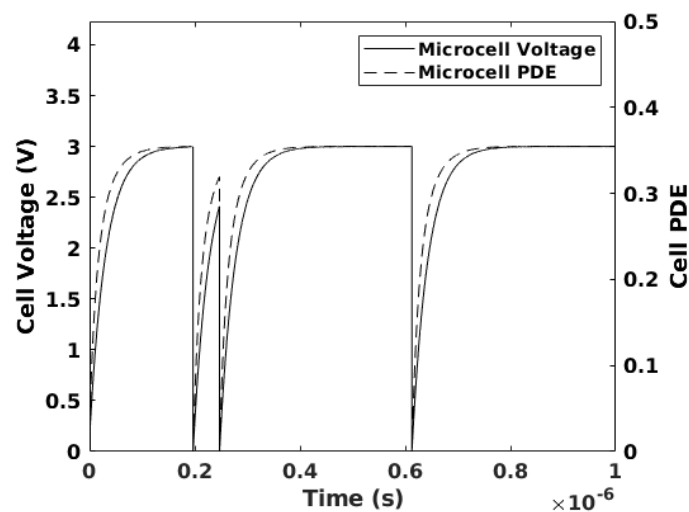
Figure 5.5: Simulated time domain response of a single microcell under 5 mWm^{-2} of 405 nm light.

5.3.2 Replicating SiPM Saturation

SiPM saturation is a macroscopic effect, measured by observing the bias current as a consequence of optical irradiance striking a SiPM and causing individual microcells to fire. As each microcell must recharge within a finite time, the inter-photon arrival time eventually is lower than the recharge time of a single microcell, and hence saturation occurs. This effect is extremely important when predicting SiPM performance as a VLC receiver, as it determines the output pulse rate. Therefore, it is crucial that the simulation agrees with measurements of the bias currents of the SiPM at different irradiances.

The current needed to sustain over-voltages of 2.0 V, 3.0 V and 3.5 V were measured from the simulation for irradiances between 0.1 mWm^{-2} and 4 Wm^{-2} , and compared to experimental results. The bias current was calculated by summing the charges of the microcells which fired during the simulation, and dividing by the total simulation time. The results in figure 5.6 show an excellent agreement between these simulated currents and the experimental results. The saturating behaviour of the SiPM is accurately replicated in the MC simulation presented, using only device parameters and the fitted PDE model in equation (4.4). The ability of the MC model to re-create this macroscopic effect from an elemental model validates it, and means insight can be drawn from it to explain in detail the mechanics behind the saturation effect, and why the effective PDE rolls off at 20 dB per decade.

5.3.3 Estimating Maximum Count Rate

The maximum count rate of SiPMs is assumed to be dependant only on the number of microcells, and the recharge time constant of the microcells. In section 3.3 the maximum count rate was investigated to determine if it varies as a function of bias voltage however there was insufficient evidence to suggest there was a relationship.

The expression for the SiPM bias current (which is proportional to the
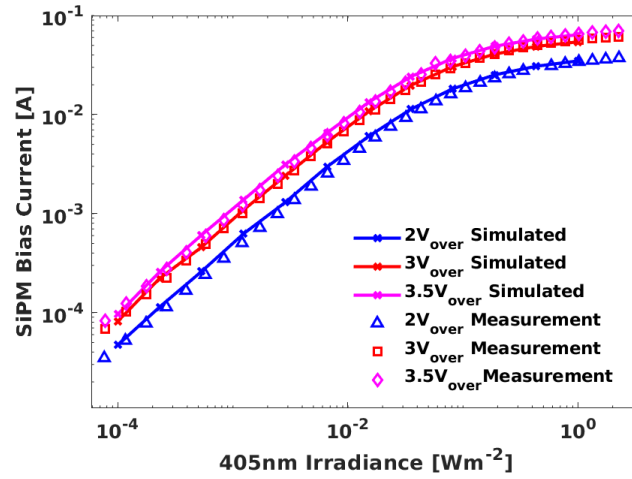
Figure 5.6: Measured and simulated bias SiPM current as a function of 405 nm irradiance.

count rate), equation (3.5), is repeated here for convenience.

$$I_{bias} = \frac{C_{cell}V_{over}N_{cells}\alpha T(L + L_{dark})}{1 + \alpha\tau_{recharge}(L + L_{dark})} \tag{5.7}$$

where α is defined as

$$\alpha = \frac{\eta A_{SiPM}}{E_p N_{cells}} \tag{5.8}$$

In its original derivation, equation (5.7) was calculated with the inaccurate assumption of a 'dead time' where a microcell is unable to detect incident photons [15] [41]. Despite this, equation (5.7) has been shown to agree well with measured and simulated bias current data. An important aspect of the derivation of equation (5.7) was the assumption of a minimum time between photons that a microcell could detect, τ_p. This parameter was not related to the recharge time of the microcell, and therefore was used to fit equation (5.7) to a specific set of experimental data. The experimental data used were for a J-Series 30020 SMTPA SiPM, where the SiPM was biased to 100 mV increments of overvoltage from 0.5 V_{over} to 4 V_{over}, and the saturated bias current was measured.

The reason why equation (5.7) agrees with experimental results can be understood by considering the bias current flowing when the SiPM is saturated. SiPM saturation occurs when the denominator of equa-

tion (5.7) is dominated by the second term $\alpha\tau_{\text{recharge}}(L + L_{\text{dark}})$. This means that the bias current is

$$I_{\text{sat}} = \frac{N_{\text{cells}}C_{\text{cell}}V_{\text{over}}}{\tau_{\text{recharge}}} \qquad (5.9)$$

which means that when considering two different bias voltages,

$$\frac{\frac{I_{\text{sat}}(V_1)}{V_1}}{\frac{I_{\text{sat}}(V_2)}{V_2}} = \frac{\tau_{\text{recharge}}(V_2)}{\tau_{\text{recharge}}(V_1)} \qquad (5.10)$$

Consequently, the ratio of characteristic times required to fit equation (5.7) to bias currents measured at different overvoltages can be determined from equation (5.10). This ratio of characteristic times was hence determined for overvoltages between 0.5 V and 4 V. The results in figure 5.7 show that, once the overvoltage is more than 1.5 V, the characteristic time is approximately constant, and changes by only 5% up to a overvoltage of 4 V. This means that, for the range of over-voltages that are typically used, the maximum count rate of a SiPM can be estimated using

$$\frac{dD}{dt}_{\text{max}} = \frac{N_{\text{cells}}}{\tau_p} \qquad (5.11)$$

Where τ_p is approximately 2.2 times the RC time constant of the microcells [43]. For the simulation, this small effect can be neglected.

5.3.4 Microcell Capacitance

Another assumption critical to the simulation is that the microcell capacitance does not vary with bias voltage. Confirming this assumption required measurement of a J30020 SiPM's bias current as a function of 405 nm irradiance for multiple bias voltages. Figure 5.8 shows the bias current measured at different overvoltages, divided by the product of the overvoltage and the PDE at each overvoltage (as measured in section 4.3.4). The important conclusion from these results is that microcell capacitance is independent of overvoltage.
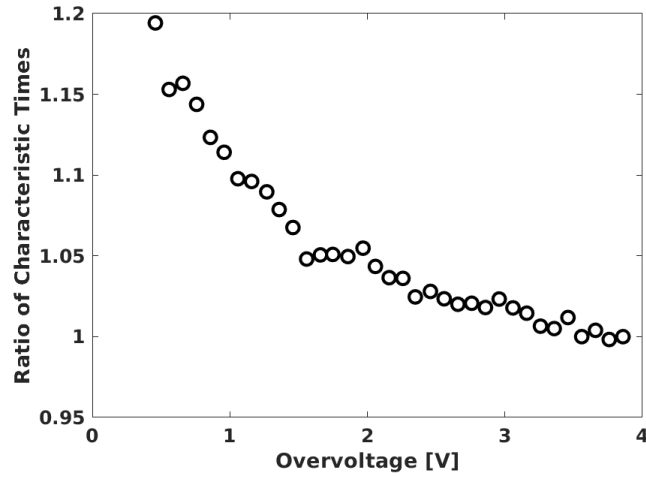
Figure 5.7: The ratio between the characteristic time obtained from the saturated current at each overvoltage to the characteristic time for 3.85 V. [43]

The bias current for irradiances which saturate the SiPM can be approximated by

$$I_{\text{bias}} = \eta(V_{\text{over}}, \lambda) A_{\text{SiPM}} C_{\text{cell}} \frac{V_{\text{over}}}{E_p} \tag{5.12}$$

which when used in combination with the measured bias current at low irradiances, the capacitance of each microcell can be determined. The resulting microcell capacitance, 46 fF, was one of the parameters used in MC simulation, which was also confirmed by earlier measurements in chapter 3.
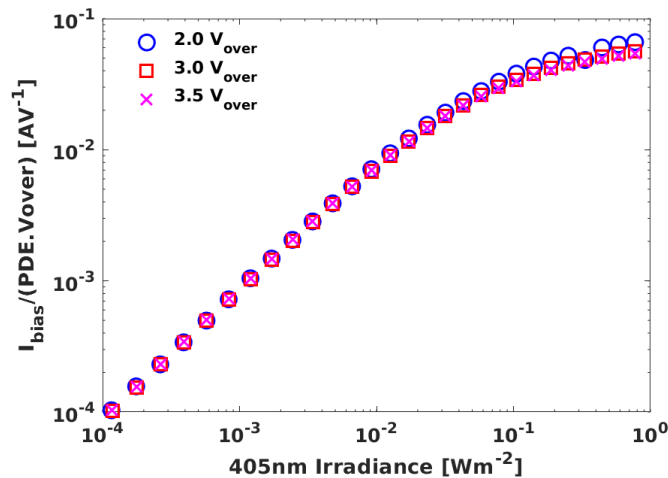
Figure 5.8: Measured bias current required to sustain a bias voltage on a J30020 SiPM at different irradiances of 405 nm light, divided by the product of the PDE and the overvoltage. [43]

5.3.5 Replicating and Explaining Effective PDE

The effective PDE of a SiPM arises from microcells being struck with and detecting a photon while they are recharging. When a microcell detects a photon during its recharge phase, an avalanche still occurs but with a reduced charge on the microcell, and hence gain. In section 4.3.5 the roll-off in effective PDE was measured to be 20 dB per decade, beginning at approximately 10 mWm^{-2} of 405 nm irradiance. The MC model was run again for this case, for 405 nm irradiances from 0.1 mWm^{-2} to 2.5 Wm^{-2} . The temporal mean microcell PDE was recorded, as was the mean fired microcell charge. Figure 5.9 shows experimental results overlaid with the outputs of the MC model, which provides an explanation for the effective PDE rolling off at 20 dB per decade. 10 dB per decade is contributed by the temporal mean PDE decreasing, as more microcells are recharging and hence have a lower microcell voltage than fully-recharged. The temporal mean PDE is important, as this determines how probable the SiPM in its entirety is to detect a photon. The mean PDE of the microcells which fire cannot be used, as this biases the measurement of the PDE by increasing it, as microcells which are more recharged are more likely to detect a photon. Another 10 dB per decade in the roll-off is contributed from the mean fired microcell charge (which can also be thought of as gain) decreasing. The mean fired microcell charge decreases with lower inter-photon times, as each microcell is more likely to detect one of the many photons striking it at a lower state of charge.

By taking the product of the mean fired microcell charge, and the temporal mean PDE, the effective PDE can be estimated. When compared to measured data in figure 5.9, this again validates the MC model as accurate.
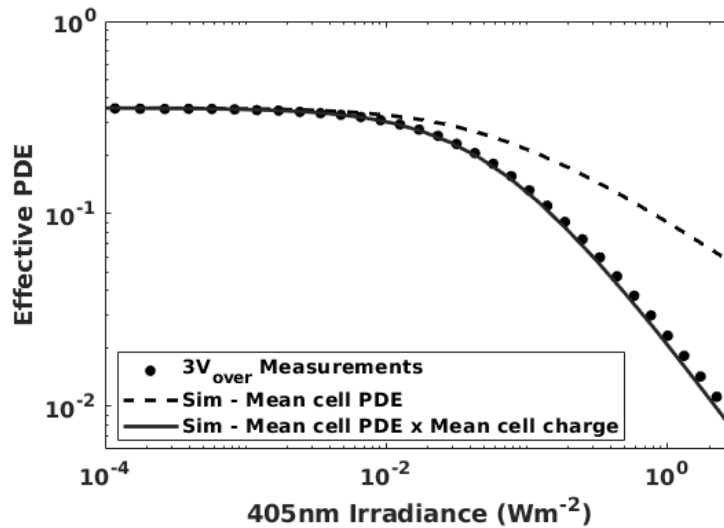
Figure 5.9: Measured and simulated SiPM effective PDE as a function of 405 nm irradiance.

5.4 Data Transmission Experiments

To validate time domain accuracy in communication channels, the simulation was used to investigate the required photons per bit for optical wireless links with no ambient light. The same signal processing chain as with measurements in chapter 4 was used with the simulator.

After amplification, the peak-to-peak voltage resulting from a single avalanche on a J30020 SiPM was 15 mVpp. Other than shot noise from the SiPM receiver, thermal white noise from the RF amplifier was present in all experiments. With the beam from the transmitter blocked, a 5 mVpp (three standard deviations) white noise signal was observed. This noise source was significant enough to include in the MC model, therefore, Gaussian white noise with a peak-to-peak amplitude of one-third of the peak-to-peak amplitude of an avalanche event was added to the output of the simulator before decoding.

While the saturation effect and effective PDE can be replicated and explained, the RF performance of the SiPM is critical to accurately replicate. To understand how optical wireless links impact SiPMs as receivers, the simulation was used to perform optical communications experiments to validate that time domain performance can be accurately

replicated. The MC model simulated the arbitrary waveform generator, oscilloscope and all bench hardware. Identical MATLAB code used to perform data transmission experiments on the real SiPM was utilised for an accurate comparison. As the fast output pulse has a FWHM time of 1.4 ns, and the data rates tested were 500 Mbps, 1 Gbps and 1.5 Gbps, DFE was used. The interfering background irradiance was varied from 1 mWm^{-2} to 120 mWm^{-2} at six equispaced points.

Figure 5.10 shows a comparison of results from the SiPM MC model with measurements of a single SiPM on a SMTPA evaluation board. When considering the number of detected photons per bit (the bottom two figures), both the 500 Mbps and 1 Gbps measurements agreed closely with the MC model. At the highest data rate tested of 1.5 Gbps, the required detected signal photons per bit diverges from the 500 Mbps and 1 Gbps measurements. The MC model predicted this divergence, but slightly under-estimates the performance relative to experimental results at 1.5 Gbps. In conclusion, the MC simulation presented gives confidence to being able to simulate optical wireless links with a SiPM receiver in new environments, or even with new SiPM designs.

5.4.1 Replicating Previously Observed ISI

A new form of ISI was described in section 4.2, and its origin was determined to be due to the change in effective PDE during multiple bit periods. The MC model described in this chapter must be able to replicate observations in order to be used to explain the response of SiPMs.

Four different points on the bias current-irradiance curve were simulated, one in the linear region, two on the roll-off portion where the device becomes nonlinear, and one deep into the saturated region, with their precise location on the saturation curve visible in figure 5.12. These four points on the saturation curve were also gathered experimentally by capturing a data transmission at a specified bias current.

When the simulation is directly compared against measured data in
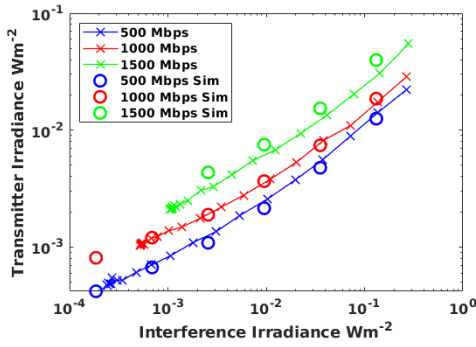
(a) Required transmitter irradiance against interference irradiance.
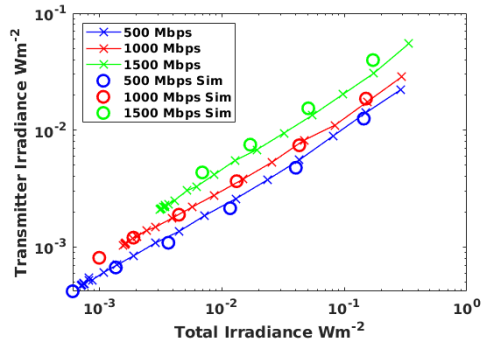
(b) Required transmitter irradiance against total irradiance.
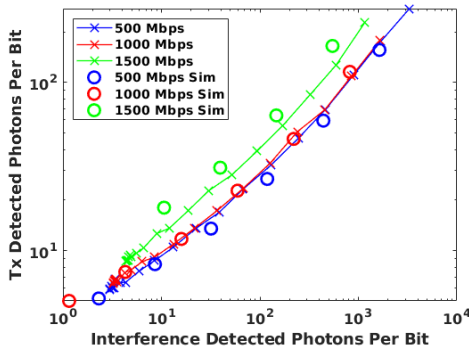
(c) Detected signal photons per bit measured against detected interference photons per bit.
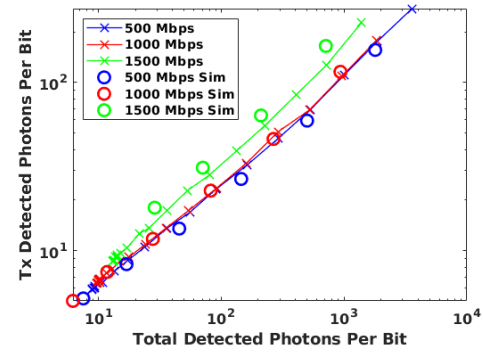
(d) Detected signal photons per bit measured against total detected photons per bit.

Figure 5.10: J-30020 SMTPA optical links compared with simulation results, and Poisson statistics models for a BER of $3.8 \cdot 10^{-3}$. Top row shows measurements in irradiances, bottom row show measurements in photons per bit-time.

figure 5.13, the development of the new ISI as bias current increases (as the SiPM saturates as per figure 5.12) is both predictable and visible. These results show the simulation was able to generate the emergent behaviour of the new ISI.

A benefit of the simulation is that it allows insight into what the effective PDE of the device is, and how this effective PDE changes between symbols. Figure 5.11 shows an example simulation for 31.2 mA bias current where new ISI occurs (which has an eye diagram visible in figure 5.13g). Using the simulation gives access to the typically hidden variable of the recharge status of the array, the 'available microcells' fraction on a SiPM device. In the case of the 31.2 mA bias current simulation, the fraction of available microcells varies between 36% and 47%,
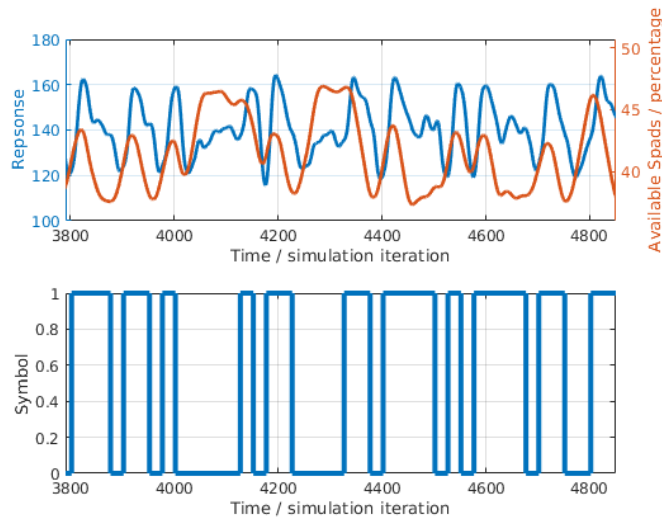
Figure 5.11: Example plot of a simulation at 31.5 mA, showing how the new ISI is caused by previous symbols changing the effective PDE of the SiPM

meaning over half of the microcells are recharging at any given time. The effective PDE is more extremely reduced or increased with long runs of transmitted 1s or 0s.

With the change in number of available microcells, the effective PDE of the device changes. In the simulation, this was the only parameter which could change the response over time, as all components were assumed as ideal, which gives credibility to the initial hypothesis.

When the irradiance (over the period of a pulse for a bit) is constant, this process creates a non-linear bit response. When data is transmitted the number of microcells available to detect a symbol depends upon the symbols in the past in a time comparable to the recharge time, as well as ambient lighting. The created model has been created to explore of this mechanism might cause the observed eye diagrams.

These experiments conclude that the simulations support the hypothesis that it is the variations in PDE arising when the SiPM is exposed to a high photon flux which cause the new form of ISI. The simulation revealed that the effective PDE changes within a bit time causes the emergent new ISI and produces eye diagrams which are comparable to experimentally obtained ones.
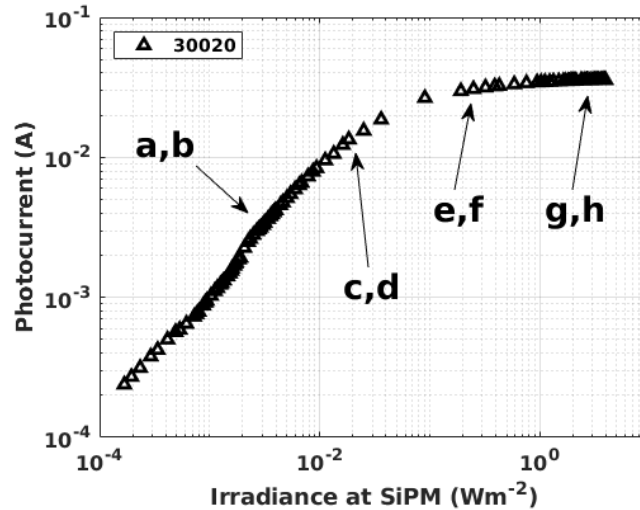
Figure 5.12: Plot showing where on the saturation curve samples were taken.

5.4.2 A Heuristic Model for Predicting the Impact of Ambient Light

The results in figure 5.10 show that the results of the MC simulation can be used to accurately predict the results of data transmission over a wide range of ambient light conditions. However, if deployed in a practical system, simulating a link to determine the required optical power is computationally expensive and requires a significant amount of time. A heuristic model was developed to predict the required transmitter power to support a link in the presence of ambient light. This model is based on the undersanding of the SiPMs response to ambient light, including the non-linear response of the bias current and the effective PDE.

Experimental results for two data rates, 500 Mbps and 1000 Mbps, for which the VLC systems performance is determined by the SiPM alone, are shown in figure 5.14. This figure also includes the performance of these systems predicted using the SiPM parameters and equation (1.1),

(a) Simulation, No ambient light

(b) Experimental, No ambient light

(c) Simulation, 12.5 mA bias

(d) Experimental, 12.5 mA bias

(e) Simulation, 20.5 mA bias

(f) Experimental, 20.5 mA bias

(g) Simulation, 31.2 mA bias

(h) Experimental, 31.2 mA bias
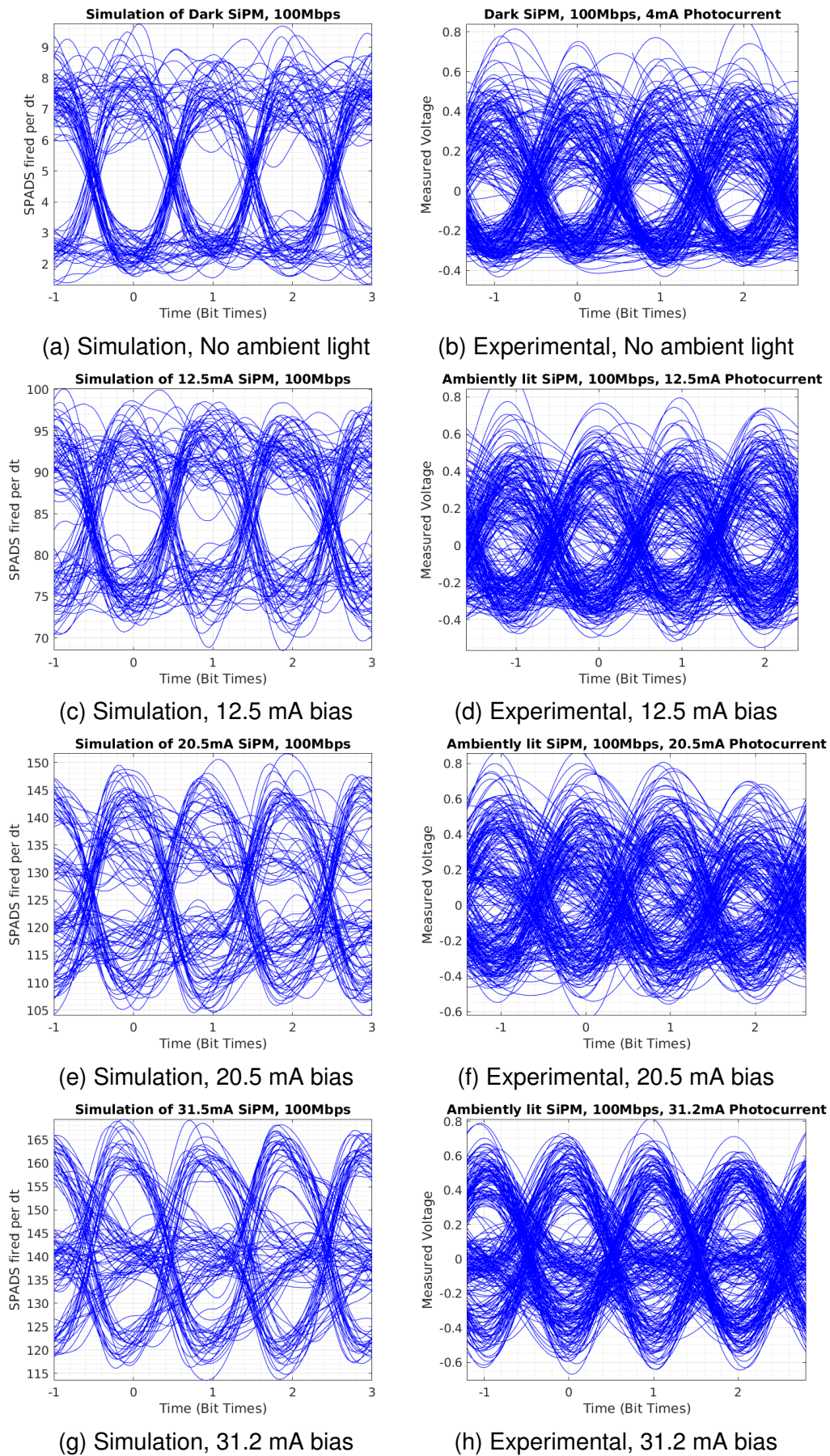
Figure 5.13: Simulation compared to experimental results, showing how the new ISI develops as the bias current increases. Sample points are shown in figure 5.12.

repeated here for convenience:

$$\text{BER} = \frac{1}{2}\left[\underbrace{\sum_{k=0}^{n_T}\frac{(n_a+n_s)^k}{k!}e^{-(n_s+n_b)}}_{\text{Tx'd 1 detected as 0}} + \underbrace{\sum_{k=n_T}^{\infty}\frac{n_a^k}{k!}e^{-n_a}}_{\text{Tx'd 0 detected as 1}}\right] \tag{5.13}$$

The results in figure 5.14 show that the performance of the SiPM receiver at 500 Mbps and 1000 Mbps can be predicted using Poisson statistics until approximately 100 detected ambient light photons per bit. However, by 1000 detected ambient light photons per bit (78 mWm^{-2} for a J-30020), there is an error of a factor of approximately two in the prediction.

A key assumption of the simulation is that the magnitude of the fast output pulse generated when a photon is detected is proportional to the charge on the microcell when that photon is detected. This means that a detection of a photon before a microcell is fully recharged will result in a smaller pulse, and as a consequence may contribute to the non-linear response of both the bias current and the fast output. The irradiance dependant effective PDE of the SiPM, shown above in figure 5.9 encapsulates this effect, and shows that the array average PDE falls to half its maximum value at 193 mWm^{-2} . In contrast, the bias current falls to have the value expected from a linear response at 78 mWm^{-2} , meaning that the array average PDE alone cannot explain the non-linear response, and the microcell charge must be considered.

Effective PDE may explain why the irradiance at which the transmitters sensitivity is half the expected value, 73.6 mWm^{-2} , is similar to the irradiance at which the measured bias current is half the expected value. The results in figure 5.9 show that this effect is as significant as the change in the array average PDE when a photon is detected. When the two processes are simultaneously taken into account, the average signal per incident photon falls to half its maximum value at an irradiance of 65 mWm^{-2} , which is much closer to the irradiance at which the bias current

is half the value expected from its linear response. The origin of the fast output pulses and the results in figure 5.9 suggest that the non-linearity in the bias current should also have an impact on the performance of the SiPM as a receiver. In this case, the impact of the non-linear SiPM response on the performance of a VLC system can be predicted by multiplying the predictions from Poisson statistics by a correction factor

$$1 + \alpha \tau_p L \tag{5.14}$$

The results in figure 5.14 show that with this correction, the experimental results for 500 Mbps and 1000 Mbps can be predicted accurately under a wide range of ambient light conditions.
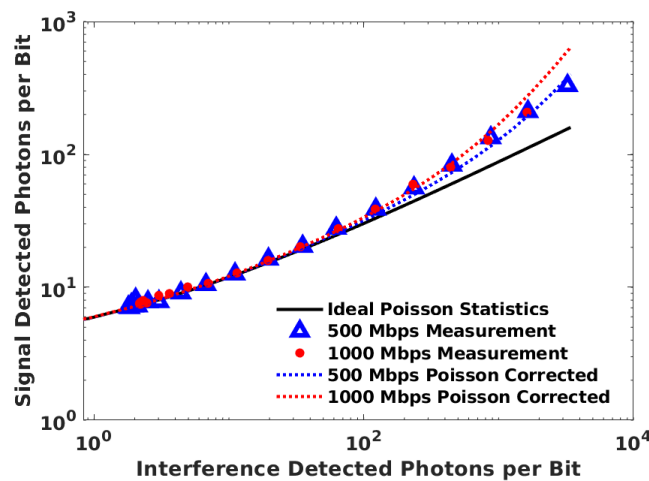
Figure 5.14: Experimental results for 500 Mbps and 1000 Mbps compared to the results expected from Poisson Theory. These results are then combined with the correction, equation (5.14). The x axis is the equivalent 405 nm irradiance that generates the same count rate and hence bias current as the incident ambient light. Fixed BER of $3.8 \cdot 10^{-3}$ used.

5.5 Discussion

Ambient light has a severe penalty on SiPMs as optical wireless receivers. The work in this chapter has outlined the beginnings of an investigation towards the understanding of the subtle impacts of device saturation on SiPMs. A MC model has been presented, which allows

for interrogation of previously hidden device variables, such as the microcell PDE as a function of time. The MC model was able to replicate macroscopic effects such as SiPM saturation, as well as provide insight on why the effective PDE rolls off at 20 dB per decade. Furthermore, the model was demonstrated to closely agree with measured data when used as a VLC receiver, which more deeply validates the model and the assumptions made on the operation of non-paralysable SiPMs. Using this simulation, more results such as the newly observed ISI have been replicated, and fully explained through the observation of previously obfuscated parameters. Additionally, a correction factor was found to accurately predict the required transmitter power to sustain a link when the SiPM is saturated. The validated MC model allows for future work designing complete VLC systems for different applications, and allows for SiPMs to optimise the design of SiPMs for VLC.

Chapter 6

Transmitter Selection, and Mitigation of Ambient Light with Selective View Optics

6.1 Overview

As highlighted in chapter 4 and chapter 5, ambient light interference causes a penalty on VLC performance with SiPMs, mandating a higher signal irradiance to maintain a VLC link. This means that reducing the interfering background irradiance is key to achieving practical optical wireless links. Previous work has shown coloured glass filters, which offer a wide field of view, offer a good remedy to this problem for WLED luminaries [12].

However, these colour filters alone are not enough to mitigate the ambient light from an outdoor scene. Initial experiments showed that when exposed to daylight (overcast, 20,000 Lux), the SiPM saturates even while protected by a combination of BG3, BG39, and B370 coloured glass filters, previously used to attenuate WLED light [12].

In office settings, coloured glass filters have been shown to be effective at mitigating ambient interference. However, they will not prevent interference from other transmitters using the same wavelength. This

interference will occur because areas covered by different transmitters must overlap. To guarantee quality of service, there must be a sufficient overlap between transmitters such that the entire area is covered by at least one transmitter. When a square grid array of transmitters is used, the worst case would occur when a receiver receives signals from four transmitters simultaneously. Any receiver without additional optics could detect light from multiple transmitters, and be unable to support a link.

Multiple transmitters will cause problems for any detector without additional optics. This, coupled with the drive to work in settings with high ambient light levels, motivates the creation of a new receiver. The new receiver should maintain a wide field of regard (FoR), to increase the probability an optical link can be received. Importantly, the new receiver should also be able to limit its field of view (FoV), such that all irrelevant light to the optical link can be blocked.

6.2 Recent Developments in the Field

He et al. have described Angular Diversity Aperture (ADA) receivers for indoor optical wireless communications, specifically to tackle the problem of multiple transmitters [58]. This device, shown in figure 6.1, uses multiple detectors each offset from an aperture, such that transmitters are occluded depending on their angle. The design choice of having multiple detectors for the ADA systems allows it to support multiple input multiple output (MIMO) communications. However, each detector adds to the cost and power consumption of the system.

The feature of the ADA which is interesting for this work is angular selection. As the FoR is split into a small number of FoVs, as many as there are detectors present, the angular resolution is poor. The poor angular resolution also means a large amount of excess ambient light reaches the detectors even if coloured glass filters are used. In addition, photo-detectors and their associated electronics are the dominant cost and power consumption elements of the system. This means that es-

pecially for mobile devices, only a few detectors should be used. Using fewer detectors carries as a consequence a lower performance in terms of angle selection, as each FoV increases, allowing more ambient light through to the detector and worsening angular resolution.
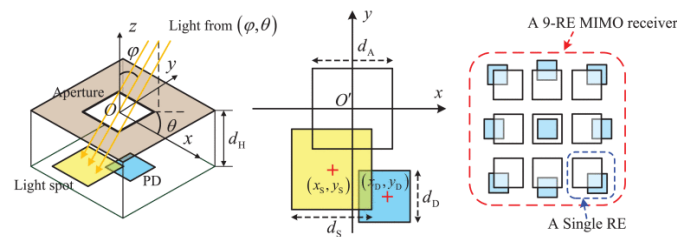
Figure 6.1: ADA described by He et al. Note that only line of sight is used to select the angle of the incident light. From [58].

This chapter discusses a novel design for an optical wireless receiver, using a single detector with a novel solid-state angle filtering method coupled to it. By combining this device with wide field-of-view colour filters, the device is shown to be able to operate in daylight.

6.3 A New Field of View Selection Device (FoVSD)

6.3.1 Construction

Figure 6.2 shows a diagram of the device to select a small FoV from a large FoR. A fixed lens (Lens 1) is initially used to image the FoR in front of the FoVSD onto a plane. An area of the image plane can then be selected by placing a movable aperture (composed of an aperture drawn on liquid crystal display (LCD)) over the region of interest, allowing light to pass through. This allows for a high angular resolution, and arbitrary regions to be selected. Light at large off-axis angles from this construction would not strike a detector, so a second lens (Lens 2) is required to concentrate the light onto the detector. This construction, the FoVSD, allows for VLC detectors to maintain a large FoR, while also having a small FoV with high angular resolution.
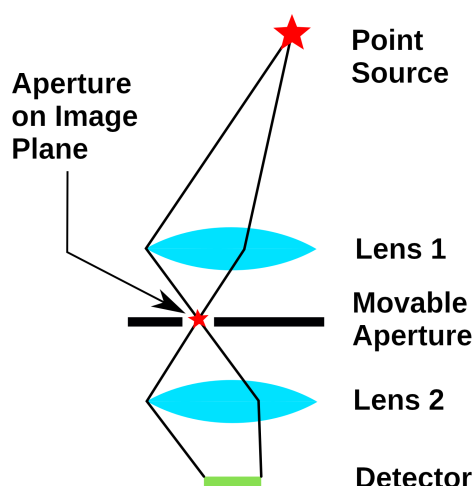
Figure 6.2: Diagram of FoVSD described using two lenses and a movable aperture to select light from a solid angle portion of space.

6.3.2 Movable Aperture

The FoVSD requires an aperture which can be arbitrarily moved around the image plane. To achieve this in solid-state, a liquid crystal display was utilised, as apertures can be written into the device. LCDs have previously been used to create arbitrary apertures, typically for the research of lenseless imaging with coded apertures [59, 60, 61]. The benefits of using an LCD include the ability to draw arbitrary apertures with high resolution in solid state, on an inexpensive, compact device.

When a small LCD used in prior work (an Electronics Assembly DOG series) was characterised, a contrast ratio of 4 was measured with 405 nm light [59]. This display does not have a high contrast ratio for 405 nm light as it was designed for visible wavelengths. The transmitters used for achieving VLC with SiPMs in this work have a wavelength of 405 nm which is not compatible with normal LCDs.

To obtain a contrast ratio which would allow sufficient performance at 405 nm, a monochrome display from a masked stereo lithography 3D printer was used. This type of display was selected as they offer a high resolution, and high contrast ratio at 405 nm, the wavelength used to cure printing resins. The display used was a ChiTu DXQ608-X04 LCD, which

has a resolution of 1620x2560 monochrome pixels and a pixel pitch of 50 μm, and was controlled by a HDMI to MIPI display driver[1].

To draw a circular aperture on the display, a web-page was used with a JavaScript canvas to draw a circle, and then scaled in one direction by a factor of one third. With a Philips IBRS WLED as the light source, a contrast ratio of 1000 was measured. When measured with 405 nm light from a Bivar UV3TZ-15 LED, the LCD provides a contrast ratio of 190. The system loss at 405 nm was measured to be approximately 10 dB.

6.3.3 Lenses and Dimensions

The lenses used do not have to be high quality, as the FoVSD is not used to image a scene, but rather to select a region of interest. For this reason inexpensive plastic lenses and fresnel lenses may be used.

For this study, labaratory grade lenses were used to ensure the performance of the FoVSD was not limited by the lenses. The lenses used in the FoVSD were originally selected for the small LCD (EA DOG132W) which was found to have a poor contrast ratio of approximately 4 at 405 nm. To be able to maintain a FoR of $\pm45°$ on the small display, a short focal length was required, which also makes the FoVSD more compact. The lenses used were 18 mm diameter, 8 mm focal length uncoated moulded aspheric condenser lenses from Edmund Optics, and the SiPM selected for integration in the device was an Onsemi J30020 SMTPA evaluation board.

To determine the ideal spacing between lenses, ray transfer matrix analysis was used to calculate a first design iteration. The software written to run this analysis is detailed in appendix D, which allowed for the ability to quickly verify the choice of and configuration of the lenses met the requirement of a $\pm45°$ FoR.

Figure 6.3 shows examples from the modelling of the FoVSD, where an angle change of incident light causes a change in the lateral distance

---

[1]The HDMI timings used to drive the display are represented by the X.Org modeline:
```
"DXQ608" 115.57 540 610 620 666 2560 2610 2612 2630 -hsync +vsync
```
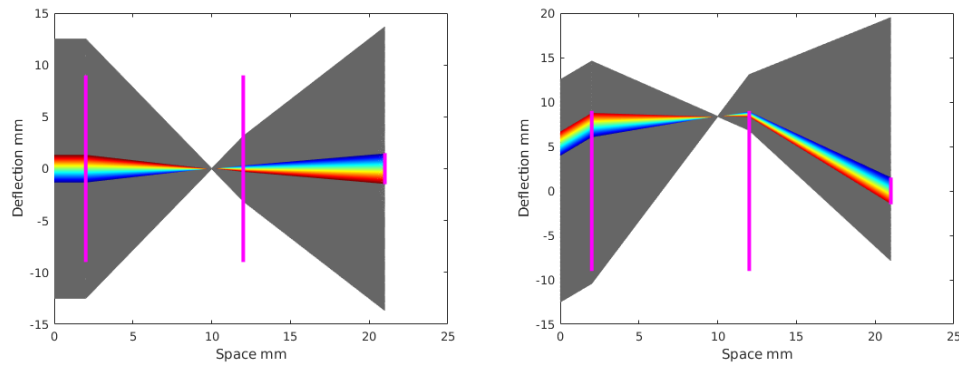
(a) Point source at $0°$ from the normal of the device

(b) Point source at $45°$ from the normal of the device

Figure 6.3: FoVSD modelling and design which achieves a $\pm45°$ FoR. Point sources are infinitely far away such that rays are parallel arriving at the FoVSD. The two 18 mm pink vertical lines are thin lenses, and the 3 mm vertical pink line is the detector. Rays coloured grey are rays which do not strike the detector. Rays which strike the detector are uniquely coloured such that the order of the rays can be easily determined.

along the image plane. The optimal spacing from this analysis was found to be 8 mm between the lenses. Maximising the ratio of the focal length to the diameter was important, as otherwise light at $\pm45°$ would not strike the detector. Interestingly, the region of the first lens which passes light to the detector was found to have a maximum area equal to that of the detector. This observation is consistent with the laws of optics, as étendue is conserved throughout the system.

The results from this analysis were used to start initial experiments to determine the optimal spacing between lenses. Further iteration was required as the lenses used are plano-convex aspheric thick lenses, and aberrations were also present, both of which are unaccounted for by the ray transfer matrix analysis. After experimental iteration, the displacements 13 mm and 11 mm from the centroids of the lenses were found to provide the highest performance in coupling light to the SiPM. To secure the geometry and block ambient light, this design was formalised in a 3D printed mount, shown in section view in figure 6.4. A 40 mm fan was used to cool the SiPM, and curved air ducts were built into the 3D print to provide line of sight breaks to the detector.
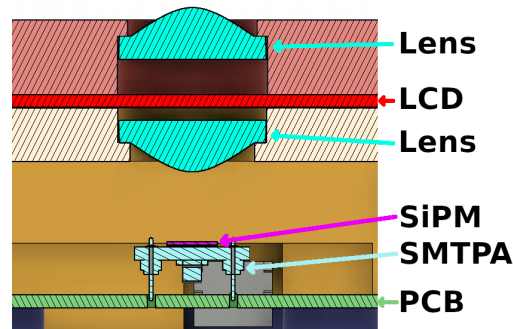
Figure 6.4: Section view of the FoVSD assembly. Visible are the Lenses (in cyan), imaging plane LCD (in red), and the J30020 SiPM detector (in magenta).

6.4 Characterisation

6.4.1 Aperture Dimensions for Selecting VLC Transmitters

A light source with the same exit aperture as a potential transmitter (a GU-10 bulb) was used. GU-10 bulbs are extremely common in modern luminaries in offices and homes, and have an exit aperture of 50 mm. The typical angular divergence, or 'beam angle' of GU-10 bulbs vary depending on the manufacturer. Typical office ceiling heights range from 240 cm to as high as 340 cm, and desks typically are 80 cm tall [62]. In the worst-case scenario for communications, where a device is on a desk and receiving light from the upper end of ceiling heights, the transmitter is 260 cm from the source. At 260 cm from the source, a GU-10 occupies a circle with a $1°$ radius in the FoR.

An experiment was hence performed to determine the optimal aperture diameters to couple light from a $1°$ transmitter onto a detector. An Onsemi J30020 SiPM (SMTPA) was used in the FoVSD, and was biased to 27.5 V. A Bivar UV3TZ-405-15 LED was placed at a distance of 300 mm from the first lens of the FoVSD, to create a source with an angular width of $1°$. The LED was manually aligned to the be normal to the receiver, and in the centre of the FoVSD's FoR. Alignment was performed

by raster scanning the LED across the FoR, and observing the bias current of the SiPM. This Risk Group 0 LED was biased with a Keithley 224 source measure unit to a bias current of 6 mA. The diameter of the aperture was varied from zero pixels to 600 pixels (600 pixels being fully open over the lens), and the bias current was measured with a Keithley 196 digital multi-meter.

The results in figure 6.5 show for a $1°$ source, perfectly aligned with the FoVSD, the bias current monotonically increases with aperture diameter. This bias current increases rapidly up to a diameter of eight pixels, at which point the increase in aperture diameter gives little extra benefit in light from the source, but allows more ambient light in. For this reason, an aperture diameter of eight pixels was selected as the aperture opening to work with practical VLC transmitters while aligned.
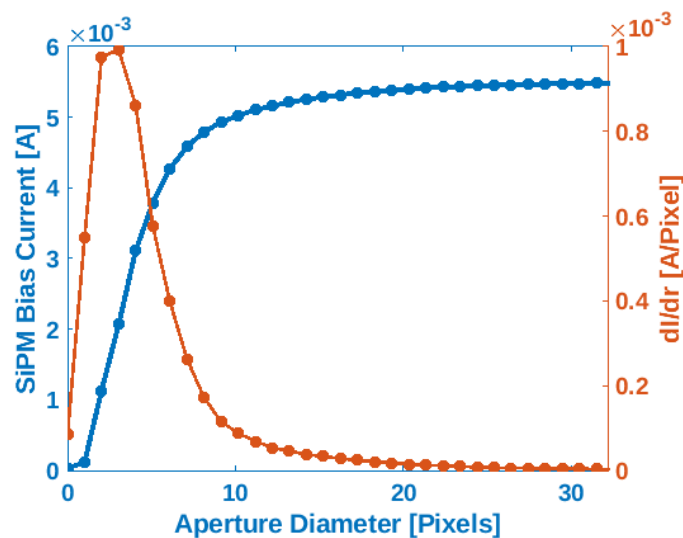
Figure 6.5: Measured bias current for varying aperture size with a $1°$ source. The rate of change of bias current with respect to aperture diameter is also visible.

To measure the performance of the FoVSD when the transmitter is not directly aligned, the FoVSD was mounted on a rotation stage, and the angle of incident light was varied by rotating the FoVSD. For each angle of incident light, seven aperture positions were used to select different FoVs between normal to the FoVSD and $+40°$. For each of the selected FoVs, ten apertures from 0 to 60 pixels in diameter were drawn, and the

SiPM bias current was measured.

The results shown in figure 6.6 show the SiPM bias current of the FoVSD with respect to aperture diameter, and angle of incident light, for different aperture positions to select different FoVs. As the aperture diameter increases, the angle of the FoV which is selected to pass to the SiPM increases proportionally. For diameters less than sixteen pixels, the aperture does not pass all the incident light to the detector. This was found by observing the measurements at each selected angle figure 6.6, and finding the minimum aperture diameter required to cause 90% of the maximum bias current. When an off-axis angle is selected, the FoVSD is able to reject light from all angles other than the selected FoV, which demonstrates that FoV selection is occurring. These results are consistent with the aligned experiment, and show that a four pixel aperture is sufficient for off-axis transmitters.

The displacement of the illuminated area on the display corresponding to angle of light incident to the FoVSD was also measured. While mounted on a rotation stage, seven angles between $0°$ and $40°$ were selected, and the position of the aperture which yielded the maximum bias current was measured by performing a binary search on the display. Figure 6.7 shows the displacements in both pixels and millimetres for different angles of optical sources from the normal of the device. These results show that light sources at arbitrary angles require 2.2 pixels (0.12 mm) per degree from the normal of the FoVSD. The requirement of a 8 pixel aperture diameter for adequate coupling of a $1°$ source shows that non-idealities are present in the device.

6.4.2 Performance Over Field of Regard

The data from aperture diameter of eight pixels, corresponding to the optimal aperture for the $1°$ source, was extracted from the surfaces for each selected angle, and combined on a single figure. Figure 6.8 shows that for apertures at different target positions, angular selection is taking
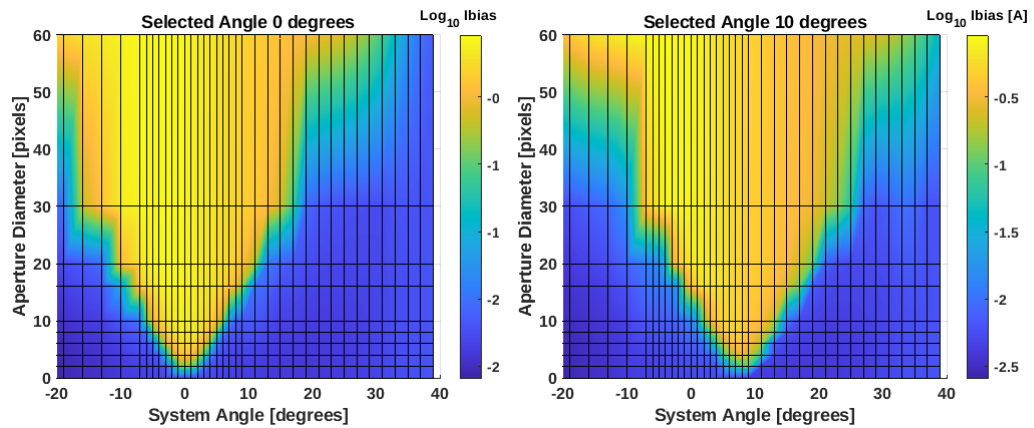
(a) Aperture centred to pass light from 0 degrees.

(b) Aperture centred to pass light from 10 degrees.
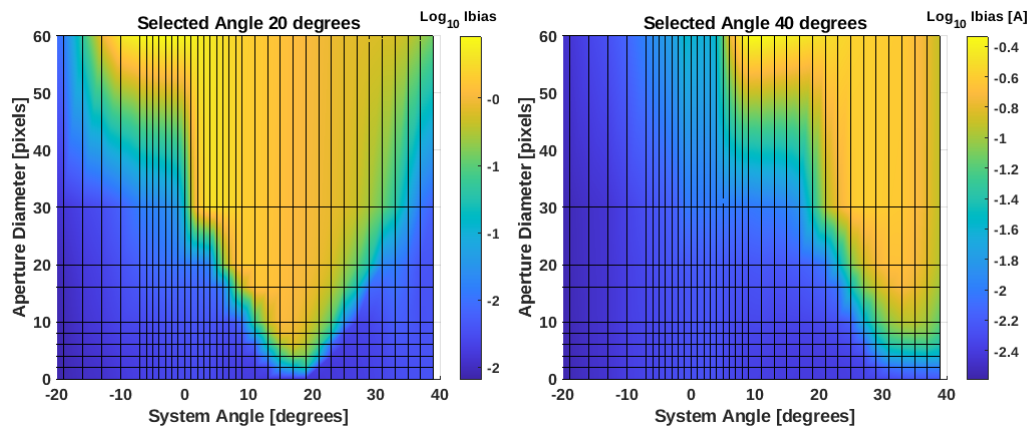
(c) Aperture centred to pass light from 20 degrees.

(d) Aperture centred to pass light from 40 degrees.

Figure 6.6: Measured SiPM bias current for varying transmitter angle and aperture diameter. Four different aperture positions are selected to target optical sources at 0, 10, 20 and 40 degrees.
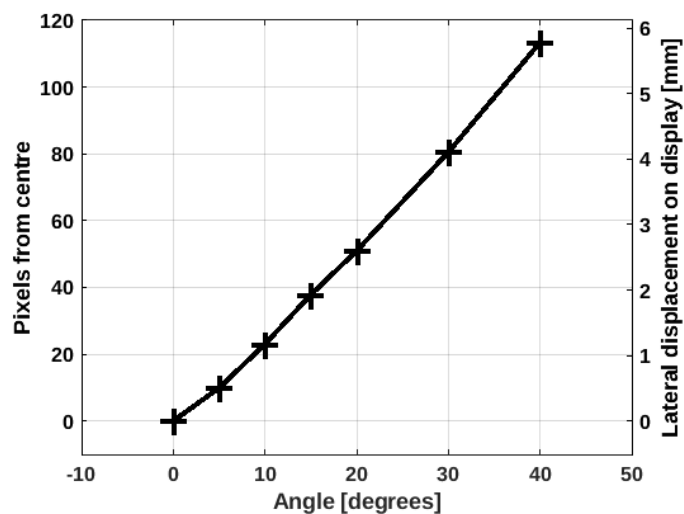
Figure 6.7: Displacement of the spot produced on the display as a function of the angle of the light source.
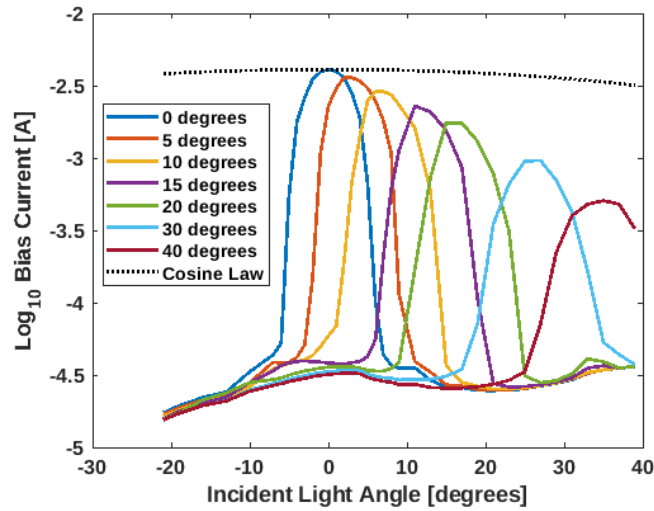
Figure 6.8: Bias current vs incident light angle for different selected target angles. A diameter of eight pixels is used for each offset aperture.

place with a full width half max of 8 degrees and a rejection ratio of 100. The results also show that light from a transmitter $8°$ from the target transmitter can be totally rejected.

Figure 6.8 also revealed that the FoVSD performed significantly worse than the cosine dependence arising from the projected area. When a light source is positioned $30°$ from the FoVSD normal, the irradiance at the SiPM is 25% of the irradiance when perfectly aligned. A simple power model for the angle dependant loss was calculated to be a power law

$$L = L_0 \times 10^{\frac{-|\theta|}{40°}} \qquad (6.1)$$

where L is the irradiance at the detector, L_0 is the irradiance at the detector when incident light arrives normal to the FoVSD, and θ is the angle of the incident light.

To mitigate losses caused by aberrations at larger angles, the aperture diameter was increased, to increase the amount of light coupled to the detector. Results from figure 6.7 were used to determine the minimum aperture diameter that would couple 90% of maximum possible irradiance, for each angle selected. The diameter variation as a consequence of the angle is documented in table 6.1. Figure 6.9 shows the
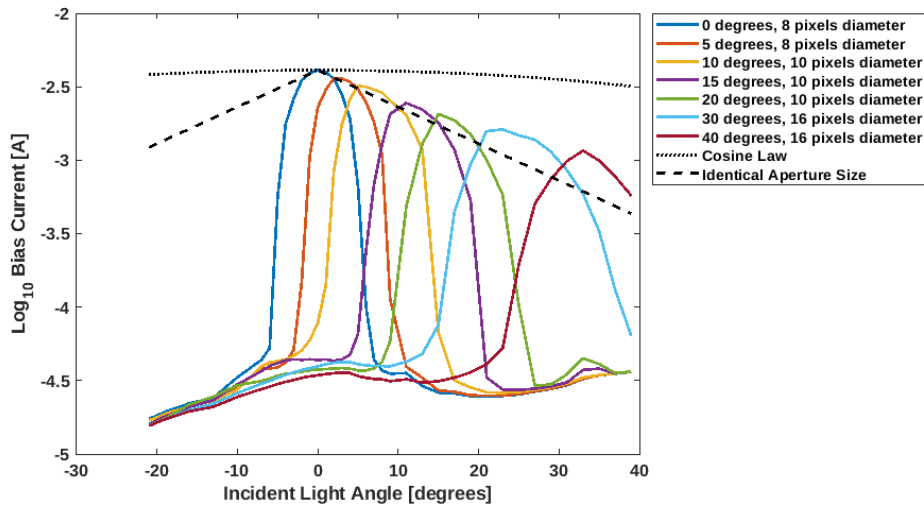
Figure 6.9: Bias current vs incident light angle for different selected target angles. A variable diameter was used to mitigate signal roll-off. Equation (6.1) is used to show the bias current without varying the diameter.

Table 6.1: Aperture Diameter as a function of angle of selected region

Angle [°]	Diameter [Pixels]
$\theta \leq 5$	8
$5 < \theta \leq 20$	10
$20 < \theta \leq 40$	16

system performance when the aperture diameter was varied, depending on the selected angle. Relative to maintaining a constant radius, the angular losses were reduced, but still did not reach the losses predicted by the cosine law. When selecting a transmitter at 30°, 45% of the light reached the detector, which is a factor of 1.8 times the amount of light reaching the detector when the radius was not adjusted.

6.4.3   Ambient Light Interference Model

To estimate the impact of ambient light from a large, bright scene, a Lambertian source was used to emulate typical outdoor environments. The Lambertian light source, covering the field of regard of the FoVSD, was a RS Components light box typically used for photograph negative viewing, and had CFL sources. This light box was was placed 30 cm from the FoVSD (containing a J30020 SiPM), and provided 2600 lux at the FoVSD entrance aperture. The aperture diameter was varied be-

tween fully closed and 120 pixels in diameter, and the bias current was measured for each diameter.

Figure 6.10 shows measurements of the SiPM bias current for varying aperture diameter with the Lambertian CFL source. With the CFL source, the display had a contrast ratio of 70, which is approximately a third of the contrast ratio of 190 at 405 nm. The ambient light irradiance at the SiPM, and hence the bias current increase monotonically with aperture diameter. When the aperture is completely closed, some light still leaked through due to the poor contrast ratio of the LCD.

A model was created to describe the amount of ambient light passed to the detector, as a function of aperture diameter. The angle of the selected FoV is easy to obtain from the diameter,

$$\theta = \frac{d_{\text{pixels}}}{0.2} \tag{6.2}$$

where d_{pixels} is the diameter of the aperture drawn in pixels, and θ is the half angle of the selected FoV.

The solid angle selected by the FoVSD (Ω) is hence calculated from the selected angle θ as

$$\Omega = 2\pi(1 - \cos(\theta)) \tag{6.3}$$

Finally, an expression for the 405 nm equivalent optical irradiance coupled to the detector was calculated. The terms which identify the irradiance 'leaked' through to the display when pixels are in their opaque mode, and the irradiance 'selected' are emphasised.

$$L = (1 - b) \left[\underbrace{\frac{\Omega}{2\pi} L_0}_{\text{Selected}} + \underbrace{\left(1 - \frac{\Omega}{2\pi}\right) \frac{L_0}{C}}_{\text{Leakage}} \right] \tag{6.4}$$

where C is the contrast ratio of the display, L_0 is the irradiance at the

input of the FoVSD and b is a loss factor which represents the fraction of the light lost through the LCD.

To convert between lux from the CFL and 405 nm equivalent irradiance, a conversion factor of 6.0×10^{-4} Wm^{-2}lux^{-1} was used. This factor was determined separately by taking lux measurements and measuring the bias current of a bare SiPM, for a CFL source.

Finally, once the irradiance at the detector (L) has been calculated, the bias current I can be predicted by using equation (3.2) and equation (3.5), repeated here in a combined form,

$$\alpha = \frac{\eta A_{\text{SiPM}}}{E_p} \tag{6.5}$$

$$I = \frac{Q_{\text{cell}} N_{\text{cells}} \alpha (L + L_{\text{dark}})}{1 + \alpha \tau_{\text{recharge}} (L + L_{\text{dark}})} \tag{6.6}$$

where η is the photon detection efficiency, E_p is the photon energy, A_{SiPM} is the area of the SiPM. τ_{recharge} is the recharge time of a single microcell and N_{cells} the number of microcells.

Figure 6.10 shows close agreement between the model in equation (6.4) and measurements. The loss factor b for the display was measured to be 0.897, meaning only 10.3% of the light striking the FoVSD could possibly be coupled to the detector with a fully open aperture. This was confirmed by taking direct measurements of a 405 nm laser source with a 818-UV calibrated photodiode, and comparing with measurements where the display was in the optical path.

6.5 Performance in Daylight

6.5.1 Motivation

The FoVSD has demonstrated the ability to select a small FoV over a large FoR. This capability shows that the FoVSD is able to reject large amounts of ambient light, and allow for VLC links in hostile environments.
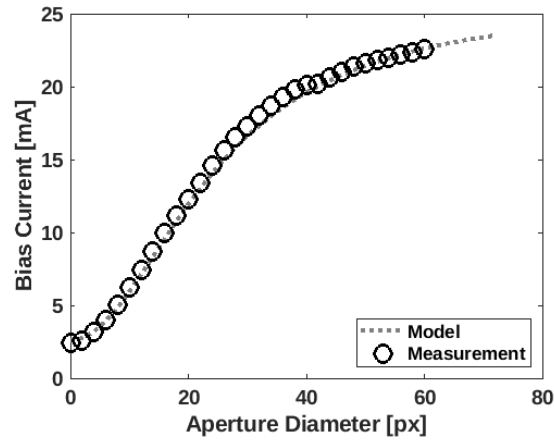
Figure 6.10: SiPM bias current vs aperture diameter. Equation (6.4) is compared against experimental results.

Daylight is a significant problem for VLC, as solar emission occupies the same wavelength bands used to establish VLC links. Rejecting the large amount of ambient light from daylight may be the ideal use-case for the FoVSD, as coloured glass filters alone are not enough to achieve a low enough ambient irradiance, while maintaining a large FoR [12].

6.5.2 Experiment Description

To determine if the FoVSD may enable VLC links in daylight, experiments were performed to quantify the amount of daylight coupled to the detector. An office in the Oxford Holder building, overlooking University Parks, was used to take measurements of the outdoor environment. Lux measurements were captured with a Yoctopuce Yocto-Light-V3 was calibrated against a Sekonic L508 light meter. The Yocto-Light-V3 uses a BH1751FVI sensor, produced by ROHMS. Calibration was necessary as the Yocto-Light-V3 was uncalibrated from the factory, and a linear conversion factor of 1.60 was found to be required to match the Sekonic L508.

In contrast to optical sources such as a LED, laser or WLED lamp, daylight contains a significant quantity of infrared radiation. The LCD used was unable to attenuate infrared light, meaning the SiPM was saturated even when the shutter was closed while exposed to daylight. To remedy this issue, optical filters were placed before the FoVSD input

lens, which a band passed a wavelength range centred at 405 nm [12]. The optical filters selected were BG3 and BG39 coloured glass filters, produced by SCHOTT.

The scene in front of the FoVSD, shown in figure 6.11, was raster scanned with a 8 pixel diameter aperture. A J-30020 SMTPA evaluation board was biased at 27.5 V, and bias currents were measured for each selected FoV. In this experiment, bias currents corresponding to a 40 x 40 grid of different FoVs was captured. This results in 1600 different FoVs being selected, which takes approximately two hours to accomplish. A challenge with taking these measurements over such a long time period, is that the solar flux on a particular region changes with time. To correct this effect, bias currents were normalised by their lux measurement, such that all measurements are relative to the maximum lux level experienced by the device.

6.5.3 Experimental Results and Discussion

Figure 6.12 shows two scans, one at 10,000 lux (an overcast day), and one at night. At night, the FoVSD detected only a street lamp, which caused a bias current of 3.8 μA. The dark scene meant that a low bias current was stimulated, with the average of the scene causing an equivalent of 4 μWm^{-2} of 405 nm equivalent irradiance on the SiPM. The scene projected on the LCD is a circle, and the raster scan captures the entire projected scene forming it. This effect is visible on the measurements in daylight. In daylight, it is only possible to distinguish between the sky and the ground. The sky has a large 405 nm component due to Rayleigh scattering, while the ground reflects relatively little 405 nm light, which can be seen by the difference in the bias currents on the upper and lower halves of the raster scan. The peak bias current at 10,000 lux was 13 mA, which corresponds to a 405 nm equivalent irradiance of approximately 15 mWm^{-2} .

Data from section 4.4.1 were used to estimate the transmitter power

required to support a 405 nm link at 10,000 lux. With no losses from the FoVSD, a transmitter irradiance of 30 mWm^{-2} is required to support a 500 Mbps link. However, the losses from the FoVSD, which has a transmittance of 11.3%, and coloured glass filters, which have a transmittance of 82%, mean that the required transmitter irradiance is approximately 330 mWm^{-2} . This transmitter irradiance is unfortunately far above the eye-safe limit, which means more work is required to develop a system which is able to support a VLC link in daylight.

Figure 6.11: Image of the scanned scene at 10,000 lux (overcast day).

(a) 10,000 lux (overcast day)

(b) 1 lux (night) Visible in this image is a street lamp, in the small region to causing the highest bias current.
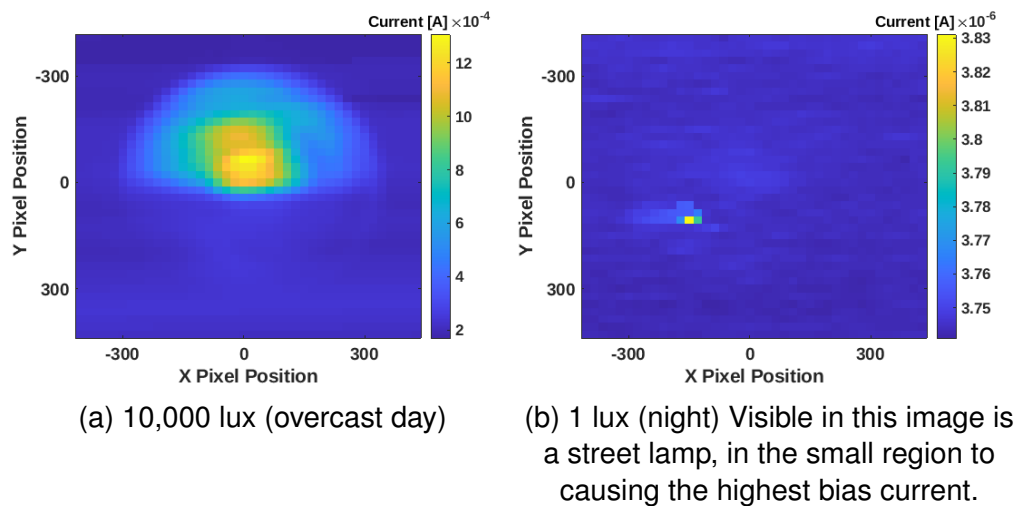
Figure 6.12: Raster scans of the FoVSD with a eight pixel diameter aperture.

6.6 Transmitter Selection

6.6.1 Motivation

In a deployed VLC system, there must be a sufficient overlap between transmitters such that the entire area is covered by at least one transmitter. Having multiple transmitters within the receiver's field of view introduces a significant amount of interference, as each transmitter is a time-varying source. Multiple transmitters being detected will degrade the target link's SNR. Additionally if two transmitters with equal power are being detected, it is impossible to achieve a link without rejecting one of the transmitters, regardless of the detector used. This motivates the desire to select the transmitter in the receiver's FoV. This technique is often referred to as *transmitter selection diversity*, and plays a crucial role in improving the performance and reliability of VLC systems [63]. Transmitter selection diversity has typically been achieved in VLC with beam-steering [64, 65, 66, 67]. However, beam-steering requires costly infrastructure, and can only service a limited number of users. Transmitter selection diversity, through the receiver selecting transmitters, can significantly enhance the overall data rate and capacity of VLC systems, by intelligently selecting the transmitter with the highest SNR at any given moment.

An additional minor benefit of selecting a single transmitter is that a lower SiPM bias current is stimulated within the receiver. By focusing the detector's attention on the most favourable transmitter, it can reduce the power consumption of the receiver, making VLC more viable for mobile devices.

6.6.2 Requirements

The IEEE802.11bb task group focusing on light communications provides comprehensive information about various typical scenarios applicable to VLC systems. One of these scenarios, known as the 'enterprise

scenario', envisions an office space measuring 6 meters by 6 meters with a ceiling height of 3 meters. In this setup, there are 9 access points (AP) positioned within the ceiling. These access points are organised into three rows, and each AP maintains a separation of 2.5 meters from its nearest neighbours. This configuration results in a maximum horizontal distance of 1.77 meters between a receiver and an AP's centerline [68].

Eye-safe transmitters for VLC have been previously described, which can meet these requirements [12]. From the receiver's point of view, the transmitters are positioned 39° apart at their closest [12]. To adequately achieve transmitter selection diversity, sources must be able to be selected, and rejected when they are 39° apart.

6.6.3   VLC Link Wavelength

To determine how well the FoVSD can achieve transmitter selection diversity, experiments were performed. b, the loss factor discussed in equation (6.4) was measured to be 0.887 with a 405 nm source. This system loss is too high to maintain a VLC link at 500 Mbps, which is the minimum data rate required to avoid microcell recharge ISI, as detailed in section 4.2.1. An irradiance of approximately 20 mWm^{-2} was required to support a 500 Mbps link at 405 nm, which is above the 4 mWm^{-2} described as an eye safe limit for practical transmitters [12].

405 nm was previously selected as the VLC link wavelength as it allowed using filters to reject ambient light. Now that the selected FoV is much smaller, these filters are not needed, and other wavelengths can be considered. High bandwidth laser diodes are available at 520 nm, and have been used previously to create VLC links [69]. At 520 nm, the loss factor b on the LCD was measured to be 0.80, which means approximately 1.77 times more irradiance strikes the detector compared to 405 nm. The LCD was more performant at 520 nm, as the contrast ratio of the LCD was 200 at 520 nm, compared to 100 at 405 nm. Importantly, in

addition to a greater amount of light reaching the SiPM, the eye-safe limit with 520 nm light is higher by a factor of 6.25. A further benefit of switching to 520 nm was observed in the contrast ratio of the LCD increasing to approximately 200.

6.6.4 Experimental Results

A link was established using a 520 nm ThorLabs PL520 laser diode, biased at 42 mA. The same RF signal chain, and signal processing were used as with chapter 4, and a data rate of 500 Mbps was selected. The irradiance at the FoVSD was controlled to be 33 mWm^{-2} , the irradiance expected from an eye safe transmitter at 520 nm. Seven angles between $0°$ and $40°$ were selected as transmitter positions. At each transmitter position, FoVs were selected which each of targeted the different transmitter angles considered. Finally, for each combination of transmitter position and selected FoV, the BER was measured. Variable aperture diameters were used depending on the selected FoV angle, following from results in section 6.4.1.

Figure 6.13 shows that transmitters can be selected, such that VLC links can be supported up to a maximum angle of $30°$, where the BER reaches the FEC limit. For a target transmitter aligned with the FoVSD, the results show secondary transmitters can be rejected accurately, such that transmitters $5°$ or more away will not interfere. When the target transmitter is approximately $20°$ away from the transmitter, secondary transmitters up to $40°$ away from the target are detected, but their BER is above the FEC limit. This is due to the presence of comic aberration, which causes the light from transmitters to be spread over the imaging plane excessively, when selecting FoVs at angles above $20°$.

To achieve successful transmitter selection diversity, the FoVSD must be able to select sources $39°$ apart. The results in Figure 6.13 show that transmitters can be selected to a far higher accuracy than this requirement. Importantly, this means that the FoVSD enables the use of

SiPMs as receivers in environments with multiple transmitters, which will be present in practical deployments of VLC.
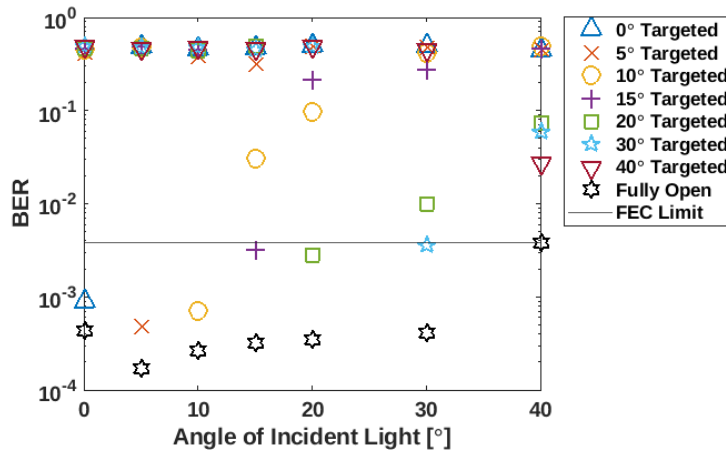
Figure 6.13: BER vs Transmitter Angle for various different targeted transmitter positions. The x axis represents different spatial configurations of the transmitter, while each data series represents a different targeted FoV. 'Fully Open' represents the case where the aperture is fully open, and the entire FoR is selected.

In the context of operation in daylight, using 520 nm would unfortunately not be viable. The ASTM solar spectrum states at 405 nm, 3×10^{18} photons $m^{-2}s^{-1}$ strike the ground [70]. At 520 nm, this increases to 5×10^{18} photons $m^{-2}s^{-1}$. The increased contrast ratio at 520 nm (200 at 520 nm vs 100 at 405 nm) is not enough to reduce the quantity of ambient light reaching the detector. As a consequence, the predicted required transmitter irradiance at 520 nm is approximately 300 mWm^{-2} , which is above the eye safe limit.

6.7   Discussion

This chapter introduced a novel optical receiver, a FoVSD, designed to reject interfering transmitters that can render a VLC link impossible to support. As an additional benefit, the FoVSD rejects ambient light interference in optical wireless communication systems. The device combined a SiPM with a novel solid-state angle filter, to select FoVs over a wide FoR, however any detector could be used. The construction of the device includes a movable aperture created using an LCD, offering high-

resolution aperture control in a cost-effective package. Lens selection and spacing were discussed, emphasising the importance of maintaining a wide FoR while enabling a small, high-resolution FoV.

The device's performance under various lighting conditions was characterised, including a Lambertian light source, which provided insights into its irradiance control and FoV selection ability. The FoVSD was able to reject the Lambertian source, which motivated attempting to use the FoVSD to control daylight. Operation in daylight was investigated, however the FoVSD was unable to reject sufficient ambient light to support a link with eye safe transmitter irradiances.

Furthermore, transmitter selection diversity in VLC systems was investigated. The investigation demonstrated the FoVSD's ability to accurately select transmitters within a specific angular range, enhancing the reliability, and SNR of optical wireless communication systems. A different wavelength was used, which had a lower system loss. The lower loss meant that eye safe links at 520 nm were possible, and were able to be selected (and rejected). This means that the FoVSD gives a practical solution to the problem of multiple transmitters within a receiver's FoV. Without selection, two equally powered transmitters would mean it is impossible support a VLC link. Solving this problem, and enabling links in this previously impossible scenario paves the way toward the use of VLC in practical deployments.

In summary, the novel FoVSD offers a potential solution to transmitter selection diversity. As a demonstration device, the FoVSD was able to select eye safe links at 500 Mbps. This demonstrates that VLC can be effectively used in real-world scenarios where ambient light, and multiple transmitters, are present.

Chapter 7

Conclusion and Future Work

7.1 Conclusion

The need for more communications channels offers the opportunity to address the problems of traffic congestion with traditional RF communications, by utilising free space optical channels to increase the overall quality of service. The work in this thesis has presented an investigation into the use of SiPMs for optical wireless communications, in practical environments where ambient light is present.

Since this investigation began, a working group has begun to define 802.11bb, a new standard for OWC networking, expected to be released in December of 2023 [68]. 802.11bb's scope is limited to up-link and downlinks in the 800 nm to 1,000 nm band (not VLC), for data rates starting from 10 Megabit/s, measured at the MAC (media access control) data service [71]. This standard will define all modes of operation within these constraints, and propel optical wireless communication into public use over the coming decades.

Additionally, research into using SiPMs as VLC receivers is thriving, as underscored by the ongoing efforts from multiple research groups [72, 73, 74, 75, 76, 77]. Recently, a new world record was set with a J-Series 30020 SiPM, which achieved a link at 5 Gigabit/s [78]. This was accomplished through employing volterra-series equalised OFDM. Such exam-

ples of breakthroughs not only validate the robustness of SiPMs in high speed optical wireless communications, but also lay the foundation for subsequent studies focusing on the interplay between complex equalisation techniques and single photon receivers.

This thesis addresses major challenges to the field, by characterising the impact of ambient light on SiPM receivers, and exploring methods to mitigate the negative impacts from ambient light. Additionally, the work explores the comparison of two SiPMs as receivers for robust optical wireless communications at Gigabit/s data rates, at irradiances where the link is Poisson statistics limited. Attention was also given to a newly observed phenomenon in which a new, non-conventional form of ISI was observed when SiPMs are exposed to ambient light and VLC links established.

In chapter 3, a new SiPM (J-Series 30020) was anticipated to achieve a higher data rate due to its higher count rate, when compared to what was previously achieved. This new SiPM was characterised in depth, and a new experiment was performed to show that the maximum count rate of SiPMs does not vary with overvoltage. A model, proposed by Zhang, was fitted to the SiPM's bias current which showed a strong agreement with measurements despite flawed assumptions.

After characterisation work, the J-30020 was demonstrated to achieve a world record data rate of 3.45 Gbps, beating the previous world record holder by over 1 Gigabit/s. When contrasted to the SiPM used by Ahmed et al. a J-30035, a higher count rate was shown to be the reason for achieving higher data rates, and improved saturation performance.

In chapter 4 it was shown that when SiPMs are exposed to ambiently lit conditions, a new non conventional form of ISI is present. Decision feedback equalisation was shown to improve the performance of the receiver when this ISI is present. Interestingly when Linear Equalisation (LEQ) was used, this new form of ISI caused LEQ to perform similarly

to DFE. This result may be due to DFE discarding information on how many microcells fired which the linear equaliser has available. The origins of the unexpected form of ISI arise from the detection of photons changing the effective photon detection efficiency. When microcells are recharging, they have a reduced charge, and have a lower probability of detecting a photon. This means that, due to light in the past, a SiPM will detect more or fewer photons in the future. Understanding the origins of, and general form of this new type of ISI is important for research going forward for single photon detectors.

A study on the impact of background ambient light was reported in chapter 4, to understand the performance penalties suffered. A new evaluation board, a SMTPA, was shown to be closer to an ideal SiPM than the previously used receiver, due to it not having a 50 Ω resistor in series with it. Removing this resistor decreased the microcell recharge time, and removed the impact of the bias voltage changing with the bias current. In the context of VLC links, the benefit of removing this resistor was also measured. The required transmitter irradiance as a consequence of the total incident irradiance, decreased when the resistor was removed, changing the power law relation from $L_{\text{Tx}} \propto L_{\text{Total}}^{0.7}$ to $L_{\text{Tx}} \propto L_{\text{Total}}^{0.58}$. This SMTPA evaluation board was characterised in detail, and compared with Poisson statistics to predict the performance of other configurations of SiPMs. Finally, despite claims on the contrary, the non-paralysability of the J-Series 30020 SiPM was confirmed for the fast output, backing up initial observations in section 3.6.

A method of combining the outputs of up to eight SiPMs was attempted, and the maximum count rate of a single J-30020 SiPM was increased by removal of its anode resistor. Including eight SiPMs in a single receiver was shown to reduce the required transmitter power by a factor of 2.32. This change in required transmitter power was lower than what was estimated by Poisson statistics, which predicted a decrease in

required transmitter power by a factor of 8. However, the performance benefit also meant that multiple SiPM receiver could tolerate a background irradiance 3.2 times higher, with a fixed transmitter power. More work is required on combining multiple SiPMs, as there are more performance benefits to be realised.

In chapter 5 a Monte-Carlo model was introduced to explore the nuanced impact of device saturation and other obscured variables, such as the time dependent microcell effective PDE. The model succeeded in replicating macroscopic phenomena like SiPM saturation and agreed well with measurements, particularly in the context of VLC. This validation extended to uncovering and explaining microcell recharge ISI and providing a correction factor for transmitter power under SiPM saturation conditions. The corroborated MC model, the only validated model for SiPMs as VLC receivers, thus opens avenues for future research in VLC system design and SiPM optimisation.

Finally, chapter 6 presented a novel solid state optical system (a FoVSD) which was developed to discriminate between transmitters, and simultaneously reject ambient light. The FoVSD was characterised and its performance analysed, which demonstrated its ability to precisely select a small FoV over a broad FoR. Consequently, the device effectively mitigates interference from both ambient light and extraneous transmitters, permitting VLC links where they were previously impossible. While the FoVSD demonstrated limitations in rejecting ambient daylight, its capability to select eye-safe transmitters at 520 nm with a data rate of 500 Mbps underscores its potential as a pragmatic solution for complex VLC deployments encountering multiple-transmitter interference.

In culmination, the most salient contributions of this thesis revolve around rigorous characterisation and optimisation of SiPMs as optical wireless receivers, particularly under the influence of ambient light. The work introduces a novel form of ISI emanating from microcell recharge

behaviour, substantially advancing the understanding of SiPM's time dependent effective PDE. It also empirically confirms the utility of DFE and LEQ in mitigating this newly observed ISI. Importantly, passively quenched SiPMs were demonstrated to not be paralysable, corroborating initial observations and debunking prevailing assumptions about their susceptibility to microcell paralysis. Notably, the J-Series 30020 SiPM was extensively characterised, establishing a world record data rate of 3.45 Gbps, attributed to the higher count rates and enhanced saturation performance. This work also provides the first validated Monte Carlo model tailored for SiPMs in VLC systems, offering a reliable tool for future research. Furthermore, the introduction and characterisation of a Field of View Selection Device (FoVSD) added a new dimension to the scope, offering a solution to the problem of multiple-transmitter interference and ambient light in VLC systems. These collective findings not only advance the theoretical underpinning of optical wireless communications but also offer pragmatic solutions for application in emerging standards.

7.2 Future Experimental Work

7.2.1 FoVSD Future Work

A novel optical device for selecting transmitters was described and characterised. The device had some non-idealities, and there is a vast scope for future work.

In this thesis, algorithms for efficiently finding transmitter positions were not considered. It is feasible that sensors on the receiver, such as gyroscopes, cameras and accelerometers, would allow for estimation of the position of the receiver, and therefore transmitters. For rooms where optical transmitter arrays are present; the layout is a known quantity which can be communicated to the receiving terminal. If the position in the room can be accurately calculated, hand-off to another transmitter would simply consist of directing the FoV towards the position of the

nearest transmitter within the field of regard, and iterating to refine the position. Measurement uncertainty may be accounted for by varying the diameter of the aperture. Further work is required to determine what an optimal transmitter search algorithm for the FoVSD may be.

In the initial presentation of the FoVSD, an LCD was used to create an aperture on the imaging plane, which has drawbacks in terms of high losses, low contrast and a slow update rate. Losses are inherently present in LCDs, as they depend on using polarisation to attenuate light, which limits the maximum theoretical transmittance to 50%. In real-world LCDs, the transmittance rarely gets close to 50%, with typical losses being in the range of 87.5% to 95% [79]. Reflective digital micro-mirror devices may offer a remedy to all of these hindrances as they have a potentially infinite contrast ratio, and lower losses.

The optical design used in this work had aberrations present in the imaging plane due to coma. This aberration meant that sources at higher angles from the device's normal require larger apertures to adequately couple light to the detector. Eliminating the coma should be possible through using lenses optimised for this application. Additionally, this avenue may allow for the use of even higher performing lenses, such as fish-eye lenses, which would further improve the FoR. Prism film (otherwise known as Brightness Enhancement Film) may allow for improved FoVSD performance, if placed at the imaging plane.

Finally, despite device saturation, SiPMs have the potential to support an optical link in daylight, using the FoVSD designed in section 6. Coloured glass filters have already been demonstrated to work for office settings, and provide a field of view of $\pm 45°$ [12]. It should therefore be possible by combining the FoVSD with coloured glass filters to design a receiver which is able support high speed VLC in daylight.

7.2.2 Numerical Model and Equaliser Development

A numerical model was designed and validated to accurately predict the performance of a SiPM, but more work is required to include more of the RF chain, including the transmitter and amplifiers. Further work on the numerical model would enable more research to be performed, as experiments take much more time to perform on real hardware, rather than the simulation.

The performance of VLC systems using SiPMs as receivers can be significantly degraded by SiPM saturation, caused by the recharging of individual microcells [40]. The mechanism used to detect each photon itself creates a non-linearity in the response to varying irradiances. Past detected photons cause the instantaneous photon detection efficiency and gain to change for the period of a microcell's recharge time. The Monte Carlo model developed allows for the understanding of how individual microcells operate, and how when used in combination the SiPM behaves as an optical wireless receiver.

Unfortunately, not much consideration has been given to the equalisation of SiPMs. The current state of the art with a J series SiPM is to use a 902 parameter Volterra Series Equaliser [78]. This equaliser must be trained for each irradiance configuration of incident transmitter irradiance, and does not consider the impact of background light. Attempts have been made previously to make an optimal equaliser for SiPMs with using OFDM, however this was performed with the assumption that the SiPM was paralysable [80]. While OFDM is a popular modulation scheme in Optical Wireless Communications, it requires linear channels which the SiPM is unable to offer without pre- or post-equalisation [40].

When a J-30020 SiPM is exposed to sufficiently high irradiances (either transmitter, or ambient light) non-linearity begins to occur at approximately 10 mWm^{-2} L_{total} which causes nonlinear harmonics. These nonlinear harmonics mean the sub-carriers are no longer orthogonal, and

therefore a performance penalty is suffered. The work demonstrating the scaling of sub-carrier SNR as a function of irradiance is worse than Poisson statistics predicts due to the impact of the nonlinear effects inherent to SiPMs [40]. Effective pre- or post-equalisation will allow a higher rate to be achieved with OOK and OFDM with SiPMs. An optimal, analytically constructed, equaliser could hence be developed to mitigate the impact of SiPM saturation, which is key to gaining the best performance of an optical link.

7.2.3 Demonstrating Versatile SiPM Receivers

More work is needed in investigating the combination of multiple SiPMs together. The 8 SMTPA SiPM board designed did not perform as well as the Poisson statistics prediction. A better understanding of why a performance detriment is present is needed to allow for the development of higher performing 'multiple-SiPM receiver boards in the future. This may be achieved by using the simulation described in chapter 5, and considering the exact electrical layout of the SiPMs. The path lengths for each SiPM are not identical, which may cause different arrival times of fast output pulses. This variability can be implemented into the simulation and be explored in a controlled environment to understand the impact of differences of PCB trace length. Other circuit boards with equal track lengths have been developed. These circuit boards contain four SiPMs and can be tested, and cross-referenced with Poisson statistics predictions to determine the origin of the penalty.

Another possibility is an experimental investigation into the fast output pulse width's impact on OOK link performance. The J-30035 SiPM has a fast output pulse width of 1.5 ns, whereas the J-60035 has an output pulse width of 3.0 ns. Nine J-30035 SMTPA evaluation board SiPMs are available, as well as a J-60035 SMTPA evaluation board SiPM. Summing four J-30035 and comparing them to a single J-60035 will allow for investigation of different output pulse widths with an identical detection

area. Results can be cross-referenced with the simulation, where work on device parameter variation has been performed, to fully understand the resultant penalties.

7.2.4 Future High Data Rate Optical Receivers

In this thesis, multiple SiPMs were combined together to create a larger detector. A problem with using multiple SiPMs is that their price is not proportional to their area. Consequently, an array of SiPMs would cost significantly more than a single SiPM with the same area. However, an issue with using large SiPMs means that the capacitance and therefore fast output pulse width increases.

A method of reducing the pulse width for large area devices is suggested by a close inspection of the layout on the bottom face of SiPMs produced by Onsemi. The bottom face reveals that these SiPMs have multiple fast outputs that are connected together to create one fast output [30]. In particular, through silicon via (TSV) processes are used at several locations on a SiPM to connect fast outputs for different areas of a SiPM to its bottom side. These fast outputs are then connected together by metal traces. The resulting combined fast output is then connected to a single output pad. Figure 7.1 shows a 3 mm by 3 mm J series SiPM has six fast outputs that are connected to a single pad, with trace lengths carefully adjusted such that they have the same propagation delay [30]. Using a connection for each of these areas would create an array of six SiPMs with an area of 1.5 mm^2 each. These six outputs could be made available separately by a relatively small change at the end of the manufacturing process. They could then be combined by using the method in figure 7.2. The result would be a 9 mm^2 SiPM with a fast output width of less than 1 ns.

Recent work emanating from the Monte-Carlo simulation developed within the thesis has suggested a pathway towards a receiver capable of operating at Terabit/s by using stacked chips for detection and signal
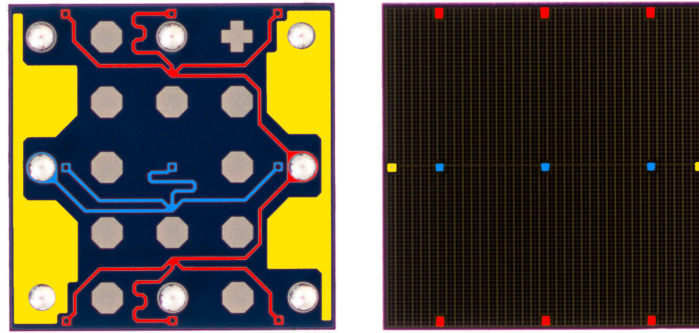
Figure 7.1: A view of a J series 30035 SiPM. Left shows the back of the SiPM, where different traces are highlighted different colours for visibility. Yellow is the cathode (connected to bias source), blue is the anode (connected to ground, or a series resistor to measure instantaneous bias current). Red traces are the fast outputs. The fast output on this device is combined from six separate regions. Right shows the top of the SiPM, where the through-silicon via processes connect to the traces on the rear. (Adapted from [30]).
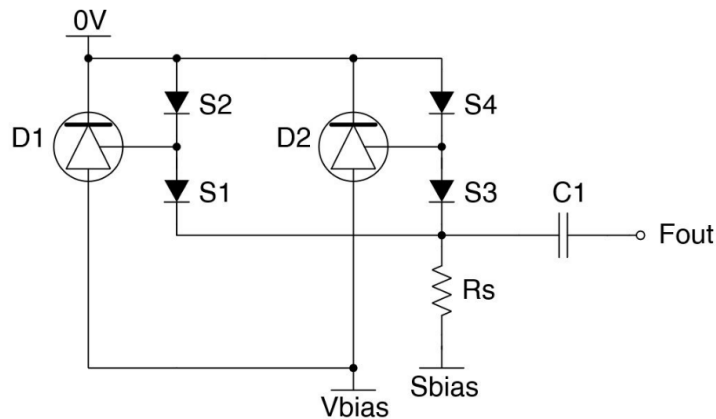
Figure 7.2: Schematic showing signal driven multiplexing by utilising dual schottky diodes to combine SiPM fast outputs [57].

processing [43]. This work, if pursued, would create the next generation of optical wireless receivers.

Appendix A

RF Interference

A.1 Description

Two main sources of RF interference were present during this project, RF from the transmitter, and RF from the laboratory environment. An impedance mismatch at the laser diode caused RF waves to radiate from the transmitter and couple to the SiPM and produce a 5 mV$_{pp}$ interference signal. The interference was confirmed to be RF to be from the laser, as when the transmitter beam was blocked the signal was still present, and could be correlated to the transmitter. To remove this interference, metallised cloth was wrapped around the cage system for the laser. When the metallised cloth shield was placed around the laser transmitter cage system, the phase of the noise changed, however it was still present. The metallised cloth had to be extended along the SMA cable feeding the laser, which when firmly secured to leave no gaps, removed the interference completely.

When the SiPM was on during working hours, a large 20+ mV$_{pp}$ signal would frequently appear on the oscilloscope. This interference was generated by users in the environment around the laboratory from mobile phones and laptop computers. When the SiPM is not biased, the peak to peak voltage of the interference decreases, however the lack of shot noise from the SiPM allowed the interference to be better cap-

(a) Mobile telecommunications band.

(b) 2.45 GHz ISM band (Wi-Fi, Bluetooth).

(c) Time Domain Mobile telecommunications band.

(d) Time Domain 2.45 GHz ISM band (Wi-Fi, Bluetooth).
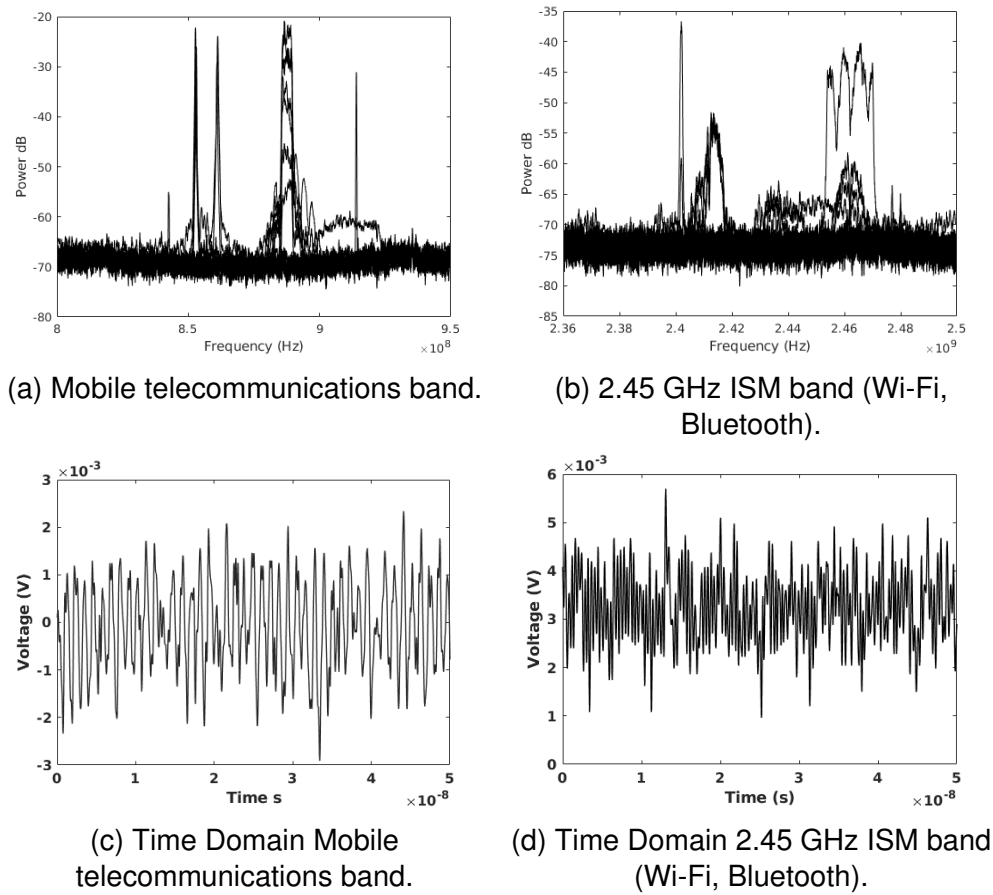
Figure A.1: RF interference present when operating the experiment during working hours.

tured and hence identified as Wi-Fi and telecommunications signals. Figure A.1 shows two frequency ranges which were found to interfere with the experiment. Figure A.1a and figure A.1c show the presence of mobile telecommunications signals, with *4G Cellular* mobile phone signals appearing between 850 MHz and 860 MHz, and *Fixed Mobile RadioLocation* signals present between 880 MHz and 890 MHz [81]. Figure A.1b and figure A.1d show the 2.45 GHz Industrial Scientific Medical (ISM) band where Wi-Fi and Bluetooth are present [81].

A.2 Mitigation

To mitigate the impact of this external interference, an interference detector was written, which allowed for the experimental rig to discard a capture from the oscilloscope, and re-attempt the BER calculation with no human intervention. The interference detector smooths the power

spectrum between frequencies of interest, fits a straight line to this smoothed spectrum, and subtracts the line as a form of 'baseline correction'. Finally, the power spectrum is tested to determine if any part is 2 dB above the baseline, which if true will reject the capture from the oscilloscope and run the experiment again. A code listing is presented below which implements this, and was used for automated experiments.

A.3   Code Listing

The following code is in MATLAB, which assumes a data structure `dataRX` to contain a timebase and voltage measurements, as would be obtained from an oscilloscope.

```matlab
function [interference_present, bands] = detect_interference(dataRX)
    % takes a structure `dataRX` which has fields `time` and
    % `voltage` from an oscilloscope capture.
    % Returns a boolean if interference is detected

    % define frequency bands to reject
    % each band has a name, start and stop
    % frequench, dB above baseline threshold
    % limit, and a smoothing factor
    bands(1).name   = "2.45GHz ISM WiFi BT";
    bands(1).start  = 2.35E9;
    bands(1).stop   = 2.5E9;
    bands(1).thresh = 2;
    bands(1).sfact  = 0.03;

    bands(2).name   = "900MHz Telecom";
    bands(2).start  = 8E8;
    bands(2).stop   = 9.5E8;
    bands(2).thresh = 5;
    bands(2).sfact  = 0.03;

    % number of points the FFT generates
    fftsize = 2^20;

    v = dataRX.voltage;
    dt = dataRX.time(2) - dataRX.time(1);

    % apply blackman window to time series
    v = (v) .* blackman(numel(v))';

    V = fft(y,fftsize);         % Perform Fourier Transform
    Pvv = V.*conj(V)/fftsize;   % Linear PSD
    Pvv = 10*log10(Pvv);        % dB PSD
    Pvv = Pvv(1:(1+fftsize/2)); % Remove alias

    freq = (1/dt)*(0:(fftsize/2))/fftsize;  % Frequency Hz

    % Loop over all previously defined frequency bands,
```

```matlab
39        % to detect if interference is present in any of them
40
41        interference_present = false;
42        for i = 1:numel(bands)
43            b = bands(i);
44
45            % Get indexes for PSD cropping
46            idx_start = find(freq > b.start, 1);
47            idx_stop  = find(freq > b.stop , 1);
48
49            % Crop the PSD, and smooth it
50            band_freq   = freq(idx_start:idx_stop);
51            Pvv_section = Pvv(idx_start:idx_stop);
52            Pvv_section = smooth(Pvv_section, b.sfact);
53
54            % Correct smoothing issues caused by edges
55            edgesize    = ceil(b.sfact*(idx_stop-idx_start));
56            noedge      = edgesize:(numel(Pyy_section) - edgesize);
57            band_freq   = band_freq(noedge)';
58            Pyy_section = Pyy_section(noedge);
59
60            % Calculate Polynomial baseline
61            p = polyfit(linspace(-1,1, numel(band_freq)), Pvv_section',2);
62
63            % Subtract polynomial baseline
64            Pvv_section = Pvv_section - polyval(p, linspace(-1,1,
↪   numel(band_freq)))';
65
66            % Threshold detection if interference is present
67            hasPower    = any(Pvv_section > b.thresh);
68            bands(i).hasPower = hasPower;
69
70            if hasPower
71                % log the presence of interference at the band
72                fprintf(strcat("Detected ",b.name, "\n"));
73            end
74            interference_present = or(interference_present, hasPower);
75        end
76    end
```

Appendix B

Monte-Carlo Simulation Code Listing and Additional Detail

Figure B.1: SimSPAD logo

B.1 SimSPAD Overview

SimSPAD is a free open source (GPL3) avalanche photodetector Monte Carlo simulator, created for this DPhil project [82]. The SimSPAD logo is shown in figure B.1. The C++ code shown below is an extract of SimSPAD, specifically the `SiPM` class used in SimSPAD to simulate photodetection. The listing shows a minimal 'SiPM' class, which can be used to create a `SiPM` object, and run a Monte Carlo simulation on an optical input.

B.2 Code Listing and Description

A 'SiPM' object is created with the following inputs:

numMicrocell A scalar integer of the number of microcells in the SiPM.

vBias A scalar double of the SiPM bias voltage.

vBr A scalar double of the SiPM breakdown voltage.

tauRecovery A scalar double of the microcell recovery time constant.

digitalThreshhold A scalar double of the digital threshhold of the SiPM.

pdeMax The maximum PDE used in the function mapping V_{over} to PDE.

vChr Characteristic voltage for the function mapping V_{over} to PDE.

dt A scalar double of the simulation timestep.

With the 'SiPM' object, the `SiPM.simulate(expectedPhotons)` method can be called, which takes:

expectedPhotons A vector of expected number of photons striking the SiPM per time step.

This minimal version of SimSPAD produces a single output, which is an array of output charge per time step.

```
1   /*
2    * This file is part of the SimSPAD distribution
3    * (http://github.com/WillMatthews/SimSPAD).
4    * Copyright (c) 2022 William Matthews.
5    *
6    * This program is free software: you can redistribute it and/or modify
7    * it under the terms of the GNU General Public License as published by
8    * the Free Software Foundation, version 3.
9    *
10   * This program is distributed in the hope that it will be useful, but
11   * WITHOUT ANY WARRANTY; without even the implied warranty of
12   * MERCHANTABILITY or FITNESS FOR A PARTICULAR PURPOSE. See the GNU
13   * General Public License for more details.
14   *
15   * You should have received a copy of the GNU General Public License
16   * along with this program. If not, see <http://www.gnu.org/licenses/>.
17   */
18
19   #include <iostream>
20   #include <vector>
21   #include <string>
22   #include <cmath>
23   #include <algorithm>
24   #include <random>
25
26   #define VERSION "0.2.1_thesis_minimal"
27
28   using namespace std;
29
```

```cpp
30  SiPM::SiPM(int numMicrocell_in, double vbias_in, double vBr_in, double
    ↪    tauRecovery_in, double digitalThreshold_in, double cCell_in, double
    ↪    vChr_in, double pdeMax_in, double dt_in)
31  {
32      numMicrocell = numMicrocell_in;  // Number of microcells in SiPM
33      vBias = vbias_in;                // SiPM bias voltage
34      vBr = vBr_in;                    // SiPM breakdown voltage
35      tauRecovery = tauRecovery_in;    // Recharge recovery time tau RC
36      tauFwhm = 0;                     // FWHM output pulse time
37      // Readout threshold (0 for analog)
38      digitalThreshold = digitalThreshold_in;
39      cCell = cCell_in;                // Microcell capacitance
40      vOver = vbias_in - vBr_in;  // Overvoltage
41      vChr = vChr_in;          // Characteristic voltage for PDE->vOver
42      pdeMax = pdeMax_in;      // PDEmax characteristic for PDE->vOver
43      dt = dt_in;              // Simulation time step
44
45      // microcell live time of last detection vector
46      microcellTimes = vector<double>(numMicrocell, 0.0);
47
48      LUTSize = 20;                    // Look Up Table Size
49      tVecLUT = new double[LUTSize];   // Preallocate LUT Time array
50      pdeVecLUT = new double[LUTSize]; // Preallocate LUT PDE array
51      vVecLUT = new double[LUTSize];   // Preallocate LUT Voltage array
52
53      seed_engines();
54      precalculate_LUT();
55  }
56
57  SiPM::SiPM() {}
58
59  SiPM::~SiPM() {} // destructor
60
61  // Convert overvoltage to PDE
62  inline double SiPM::pde_from_volt(double overvoltage)
63  {
64      return pdeMax * (1 - exp(-(overvoltage / vChr)));
65  }
66
67  // Convert time since last detection to PDE
68  inline double SiPM::pde_from_time(double time)
69  {
70      double v = volt_from_time(time);
71      return pde_from_volt(v);
72  }
73
74  // Convert time since last detection to microcell voltage
75  inline double SiPM::volt_from_time(double time)
76  {
77      return vOver * (1 - exp(-time / tauRecovery));
78  }
79
80  // Simulation function - takes as an argument a 'light vector'
81  // Light vector is the expected number of photons to strike the SiPM
82  // in each simulation time step dt.
83  vector<double> SiPM::simulate(vector<double> light)
84  {
85      vector<double> qFired = {};
86      double l;
87      double T = 0;
```

```cpp
88
89      // Initialise SiPMs with Renewal Process Model.
90      init_microcells(light);
91
92      // O(light.size())
93      for (int i = 0; i < (int)light.size(); i++)
94      {
95          // If expected num of photons per dt is negative, set to zero
96          l = light[i] > 0.0 ? light[i] : 0.0;
97
98          qFired.push_back(simulate_microcells(T, l));
99          T += dt;
100     }
101     return qFired;
102 }
103
104 // Shapes the output of the SiPM with a Gaussian pulse
105 // Convolves a Gaussian with the output.
106 // Requires additional 'signal-processing.cpp'
107 // vector<double> SiPM::shape_output(vector<double> inputVec)
108 // {
109 //     vector<double> kernel = get_gaussian(dt, tauFwhm);
110 //     return conv1d(inputVec, kernel);
111 // }
112
113 // Seed Random Engines
114 void SiPM::seed_engines()
115 {
116     poissonEngine.seed(random_device{}());
117     unifRandomEngine.seed(random_device{}());
118     renewalEngine.seed(random_device{}());
119 }
120
121 // Random double between range a and b.
122 double SiPM::unif_rand_double(double a, double b)
123 {
124     return unif(unifRandomEngine) * (b - a) + a;
125 }
126
127 // Uniform random integer. Do not change - this is fast
128 int SiPM::unif_rand_int(int a, int b)
129 {
130     return (int)(a + static_cast<double>(rand()) /
    ↪ (static_cast<double>(RAND_MAX / (b - a))));
131 }
132
133 //// SIMULATION METHODS
134
135 // Initialises SiPMs based on derived Renewal Process Distribution.
136 // This is correct for constant photon arrival rates.
137 // The true distribution for general input needs investigation.
138 // This is run at simulation time as it calculates the
139 // mean photon arrival rate.
140 void SiPM::init_microcells(vector<double> light)
141 {
142     double meanInPhotonsDt = 0; // Mean number of photons per time step
143     if (!light.empty())
144     {
145         meanInPhotonsDt = reduce(light.begin(), light.end()) /
    ↪ (double)light.size();
```

```cpp
146          }
147          if (meanInPhotonsDt == 0)
148          {
149              // If no light, set meanInPhotonsDt to be small epsilon.
150              meanInPhotonsDt = 1 / (double)light.size();
151          }
152
153          // Define and generate Inter-Detection distribution
154          // Generate rate parameter for arriving photons
155          double lambda = meanInPhotonsDt / (dt * numMicrocell);
156          double tmax = tauRecovery * 20; // Number of RC times to consider
157          int nIntegralPDE = 200;          // PDE integral points
158          int nPDF = 1500;                 // Number of weights in PDF
159          double t;                        // Time
160          double p_t;           // Integral of the PDE from 0 to t divided by t
161
162          // Inter detection time PDF
163          // f_t(t) = $pde(t) \lambda exp(-\lambda * t * p_t(t))$
164          vector<double> f_t = vector<double>(nPDF, 0.0);
165          vector<double> T = vector<double>(nPDF, 0.0); // Time vector 1xnPDF
166
167          for (unsigned long i = 0; i < nPDF; i++)
168          {
169              t = i * tmax / (double)nPDF;
170              T[i] = t; // populate time vector
171          }
172
173          // p_t(t) provides the approximation of $\frac{1}{t} \int_0^t
    ↪   pde(t) dt$
174          // This line calculates the integral, the division is
175          // carried out in the loop on the elements that are needed.
176          vector<double> p_t = cum_trapezoidal(&SiPM::pde_from_time, 0.0, t,
    ↪   nPDF * nIntegralPDE);
177
178
179          // Do integration: \int_t^{\infty} f_t(t) dt
180          // As weights are produced, normalisation is not required
181          reverse(f_t.begin(), f_t.end());
182
183          // PDF of time since detection for random stopping time
184          vector<double> weights = cum_trapezoidal(f_t, T[1] - T[0]);
185          reverse(weights.begin(), weights.end());
186
187          // Generate time since last detection distribution
188          // $f_x(t) = \frac {\int_t^{\infty} f_t(t) dt} {\int_0^{\infty}
    ↪   \int_t^{\infty} f_t(t) dt dt}$
189          // Use piecewise linear as an approximation
190          std::piecewise_constant_distribution<> d(T.begin(), T.end(),
    ↪   weights.begin());
191
192          // Randomly sample this distribution
193          for (int i = 0; (int)i < numMicrocell; i++)
194          {
195              // Negative as in the past - before simulation has begun
196              microcellTimes[i] = -d(renewalEngine);
197          }
198      }
199
200  // For a single time step, simulate all the microcells
201  // in the SiPM detector. This function relies on the
```

```
202    // internal private state microcellTimes, which stores
203    // the times when the last detection occured for each microcell.
204    // Inputs are the current time T, and the expected number of photons
205    // for this time step arriving at the detector
206    double SiPM::simulate_microcells(double T, double photonsPerDt)
207    {
208        double output = 0; // output charge for a single time step
209        double volt = 0;    // voltage for microcell
210
211        // Randomly sample poisson parameter lambda input
212        poisson_distribution<int> distribution(photonsPerDt);
213
214        // Number of incident photons
215        int poissonPhotons = distribution(poissonEngine);
216
217        int struck_cell;    // Index of the microcell struck with a photon
218
219        // For each incident photon...
220        for (int j = 0; j < poissonPhotons; j++)
221        {
222            // Randomly choose a microcell the photon hits.
223            struck_cell = unif_rand_int(0, numMicrocell);
224
225            // If microcell has already been struck, skip it.
226            if (T == microcellTimes[struck_cell])
227            {
228                continue;
229            }
230
231            // Test current microcell PDE (from LUT) against a
232            // random uniform sample to determine if detected.
233            if (unif_rand_double(0, 1) < pde_LUT(T -
    ↪  microcellTimes[struck_cell]))
234            {
235                // An avalanche (detection) has occurred.
236
237                // Get microcell voltage from LUT
238                volt = volt_LUT(T - microcellTimes[struck_cell]);
239
240                // Set detection time to now
241                microcellTimes[struck_cell] = T;
242
243                // Digital threshold test
244                if (volt > digitalThreshold * vOver)
245                {
246                    // Add fired microcell charge to output
247                    output += volt * cCell;
248                }
249            }
250        }
251        return output;
252    }
253
254    //// LOOKUP TABLE PARAMS AND FUNCTIONS
255
256    // Initialise lookup tables for the SiPM being simulated.
257    // Run at construction time. Generates Voltage and PDE tables.
258    void SiPM::precalculate_LUT(void)
259    {
260        // Number of points in lookup table
```

```
261        const int numPoints = (int)LUTSize;
262        // Determine the time range of the lookup table
263        const double maxTime = tauRecovery > 0 ? 5.3 * tauRecovery : 1E-9;
264        // dt for elements in the lookup table
265        const double ddt = (double)maxTime / numPoints;
266        for (int i = 0; i < numPoints; i++)
267        {
268            // Time
269            tVecLUT[i] = i * ddt;
270
271            // Voltage
272            vVecLUT[i] = vOver * (1 - exp(-tVecLUT[i] / tauRecovery));
273
274            // PDE
275            pdeVecLUT[i] = pde_from_volt(vVecLUT[i]);
276        }
277    }
278
279    // Photon detection efficiency as a function of time lookup table
280    double SiPM::pde_LUT(double x) const
281    {
282        return LUT(x, pdeVecLUT);
283    }
284
285    // Microcell voltage as a function of time lookup table
286    double SiPM::volt_LUT(double x) const
287    {
288        return LUT(x, vVecLUT);
289    }
290
291    // Define a generic lookup table that works with time
292    double SiPM::LUT(double x, double *workingVector) const
293    {
294        double *xs = tVecLUT;        // Precalculated LUT elements
295        double *ys = workingVector;  // Precalculated LUT elements
296        const int count = LUTSize;   // Number of elements in the array
297        int i;                       // Index to iterate over
298        double dx, dy;               // Differentials
299
300        // Check if fully recharged first. Most likely to be recharged
301        // under low arrival rate scenarios (typical use).
302        if (x > xs[count - 1])
303        {
304            return ys[count - 1]; // return maximum
305        }
306        // Find i, such that xs[i] <= x < xs[i+1]
307        for (i = 0; i < count - 1; i++)
308        {
309            if (xs[i + 1] > x)
310            {
311                break;
312            }
313        }
314        // Interpolate in the region of the LUT where xs[i] <= x < xs[i+1]
315        dx = xs[i + 1] - xs[i];
316        dy = ys[i + 1] - ys[i];
317        return ys[i] + (x - xs[i]) * dy / dx;
318    }
319
320    // Cumunulative Trapezoidal integration of vector 'f' with spacing 'dx'
```

```cpp
vector<double> SiPM::cum_trapezoidal(vector<double> f, double dx)
{
    vector<double> result;
    result.reserve(f.size());

    double s = f[0] * dx / 2; // Beginning and end add to formula
    result.push_back(s);

    for (int i = 1; i < (int)(f.size() - 1); i++)
    {
        s += 2 * f[i] * dx / 2;
        result.push_back(s);
    }
    s += f[f.size() - 1] * dx / 2; // End add to formula
    result.push_back(s);

    return result;
}


// Cumunulative Trapezoidal integration of function 'f'
// between the limits 'lower' and 'upper', with 'n' points.
vector<double> SiPM::cum_trapezoidal(double (SiPM::*f)(double), double
↪  lower, double upper, unsigned long n)
{
    // create output vector
    vector<double> output = {};
    output.reserve(n);

    // Step size of integral
    double dx = (upper - lower) / n;

    // Beginning and end add to formula
    double s = (this->*f)(lower)*dx / 2;
    output.push_back(s);

    for (unsigned long i = 1; i < (n - 1); i++)
    {
        s += dx * (this->*f)(lower + i * dx);
        output.push_back(s);
    }

    s += (this->*f)(upper)*dx / 2;
    output.push_back(s);

    return output;
}
```

B.3 Performance and Complexity Analysis

In its initial form, the simulation was written in MATLAB and required fifteen minutes to simulate the required amount of SiPM response to calculate a BER. After rewriting the program in C++, and optimising using different statistical sampling methods, execution time was driven down to approximately 170 ms, giving an improvement in execution speed by a factor of 5,300. This performance improvement enabled the simulator to be practically used by members of the research group.

The heavily-optimised C++ simulator was able to achieve an execution time of 65 ps per microcell per time step when illuminated with 10 photons per dt. This was achieved on a system using Ubuntu 20.04, a Ryzen 5 3600X processor, and DDR4-3200 memory. SimSPAD was compiled with g++, using a `O3` flag. Table B.1 shows execution times for different quantities of photons per time step. Performance measurements were taken by timing using `std::chrono::steady_clock` over 10,000 samples, and as a consequence included initialisation through the renewal process, which takes approximately 50 ps/(cell dt). The results in table B.1 suggests a linear growth. Under high photon arrival rates, microcells are more likely to be struck more than once, and as a consequence halt their execution in the loop early.

Table B.2 shows a complexity analysis for the simulation program. Interesting observations include changing the number of microcells does not alter execution time once initialised, but does consume more memory. Initialisation of the microcells is inherently an $\mathcal{O}(n)$ process, so as a consequence the entire program has runtime complexity,

$$\mathcal{O}(MN + D) \tag{B.1}$$

Where M is the mean number of photons striking the detector in each time step, N is the number of time steps simulated, and D is the number

of microcells simulated.

Table B.1: Simulation execution times for a J-30020 SiPM (14,410 microcells), 10,000 samples, 3 V_{over}

Photons / dt	Execution Time (ps/(cell dt))
0	60
1	65
10	85
100	400
1,000	3,000
10,000	20,000

Table B.2: Complexity analysis table, for execution time and memory usage as a function of different inputs

Parameter	Run Time	Memory
Number of Photons	$\mathcal{O}(n)$	$\mathcal{O}(n)$
Length of Light Vector	$\mathcal{O}(n)$	$\mathcal{O}(n)$
Number of Microcells	$\mathcal{O}(1)$	$\mathcal{O}(n)$
Number of Microcells (Initialisation)	$\mathcal{O}(n)$	$\mathcal{O}(n)$

B.4   SimSPAD Server

The C++ based program by itself would require individual users to compile the source code to run the program. Additionally, the majority of this thesis' work has used MATLAB to process BER results. Integrating C++ with MATLAB is also complex, so for most users this is not feasible. To enable mass-usage of SimSPAD, the simulator was contained in a web server, with a very simple API.

The web server receives a POST request from a user which contains a binary object of SiPM parameters, and a vector of the number of expected photons per time step. After Monte Carlo simulation, the result is returned, consisting of the SiPM parameters and the simulated SiPM response. This architecture decision means MATLAB, Python, and any other language with HTTP support can easily interact with the simulator. Multi-threading is immediately available by using cpp-httplib [83], which enables multiple simulations to be run simultaneously.

A POST request for this application has contents which are all double precision floating point numbers, encoded as chars. The first ten double precision floats are SiPM and simulation parameters, which are *in order*:

dt Simulation time step size

numMicrocell Number of Detectors

vBias Bias Voltage

vBr Breakdown Voltage

tauRecovery Recharge time constant

pdeMax Max PDE for PDE-Vover equation

vChr Characteristic Voltage for PDE-Vover equation

cCell Capacitance per detector

tauFwhm Output pulse full width half max time

digitalThreshold Detection Threshold (as a fraction of the overvoltage)

The remainder of doubles in the request are the optical input in expected number of photons per time step dt striking the photo-detector. When the simulation is completed, the response is the exception that the vector of optical input is replaced with a vector of the SiPM's response.

Appendix C

Derivation of Inter-Detection Time Probability Density Function

C.1 Acknowledgement

Dr Mihai-Alin Baidu contributed to the derivation of the distributions of inter-detection times for microcells [84].

C.2 Derivation of the Probability Density Function of Inter-detection Times

To calculate the probability density function, the discrete case is considered first. Photons arrive according to a Poisson point process of rate Λ, which is constant with time. Given an avalanche occurred at time t, the goal is to calculate the distribution of the time elapsed until the next avalanche. The time elapsed until the next avalanche is denoted by X.

The next avalanche is caused by the kth photon that arrives after t.

All cases need to be considered for all k in $0, 1, 2....$

$$\mathbb{P}(X \in (x, x+\mathrm{d}x)) = \sum_{k=1}^{\infty} \mathbb{P}(k-1 \text{ arrivals in } (t, t+x) \text{ not causing avalanches}$$

$$\text{and one arrival in } (t + x, t + x + \mathrm{d}x) \text{ that causes an avalanche)} \quad \text{(C.1)}$$

Rewritten, this is

$$\mathbb{P}(X \in (x, x + \mathrm{d}x)) =$$

$$\sum_{k=1}^{\infty} \mathbb{P}(k - 1 \text{ arrivals in } (t, t+x)) \mathbb{P}(\text{no avalanche}|k - 1 \text{ arrivals in } (t, t+x))$$

$$\mathbb{P}(\text{arrival in } (t + x, t + x + \mathrm{d}x)) \mathbb{P}(\text{avalanche}|\text{arrival in } (t + x, t + x + \mathrm{d}x))$$

$$\text{(C.2)}$$

Given that there are $k - 1$ arrivals in $(t, t + x)$, the $k - 1$ points are independently and uniformly distributed over $(0, x)$, $T_i \overset{iid}{\sim} \mathcal{U}(0, x)_{i=1..k-1}$ [84]. So,

$$\mathbb{P}(X \in (x, x + \mathrm{d}x)) =$$

$$\sum_{k=1}^{\infty} \underbrace{\frac{(\Lambda x)^{k-1}}{(k - 1)!}e^{-\Lambda x}}_{\text{Poisson Photon Probability}} \mathbb{E}\left[\overbrace{\prod_{i=1}^{k-1}(1 - \eta(V_\mu(T_i)))}^{\text{Probability of no avalanches}}\right] \underbrace{(\Lambda \mathrm{d}x)\eta(V_\mu(x))}_{\substack{\text{Probability of arrival} \\ \text{in d}x \text{ and avalanche}}} \quad \text{(C.3)}$$

Where $\eta(V_\mu(x))$ is the probability of an avalanche occurring given that a photon arrives at x, and $V_\mu(x)$ is the voltage across the microcell at x. Since all T_i are independently uniformly distributed, the expectation can be split into a product of expectations.

$$\mathbb{E}\left[\prod_{i=1}^{k-1}(1 - \eta(V_\mu(T_i)))\right] = \prod_{i}(1 - \mathbb{E}[\eta(V_\mu(T_i))]) = \left(1 - \mathbb{E}[\eta(V_\mu(T))]\underset{T \sim \mathcal{U}(0,x)}{}\right)^{k-1}$$

$$\text{(C.4)}$$

$$\text{Let} \quad p(x) = \mathbb{E}[\eta(V_\mu(T))]\underset{T \sim \mathcal{U}(0,x)}{} \quad \text{Then,} \quad \text{(C.5)}$$

$$\mathbb{P}(X \in (x, x + \mathrm{d}x)) = \Lambda \eta(V_\mu(x))\mathrm{d}x \sum_{k=1}^{\infty} \frac{(\Lambda x)^{k-1}}{(k-1)!} e^{-\Lambda x} (1 - p(x))^{k-1} \quad \text{(C.6)}$$

The density of x then follows as

$$f_\mu(x; \Lambda) = \eta(V_\mu(x))\Lambda e^{-\Lambda x} \underbrace{\sum_{k=1}^{\infty} \frac{(\Lambda x(1 - p(x)))^{k-1}}{(k-1)!}}_{= e^{\lambda x (1 - p(x))}} \quad \text{(C.7)}$$

$$f_\mu(x; \Lambda) = \eta(V_\mu(x))\Lambda e^{-\Lambda x p_\mu(x)} \quad \text{(C.8)}$$

where

$$p_\mu(t) = \frac{1}{t} \int_0^t \eta(V_\mu(t))\mathrm{d}t \quad \text{(C.9)}$$

This distribution, a renewal process, is a special case of the more general renewal process, where the inter-arrival times are not necessarily exponentially distributed. The distribution of inter-arrival times found here is not the complete solution, as a more useful distribution would be the times since detection distribution, which depends on the history of the incident light.

Appendix D

Ray Transfer Matrix Analysis Code Listing

D.1 Description

This appendix documents the MATLAB code used to design the FoVSD. The listing below is a ray transfer matrix analysis script, written to compute the performance of the angle selection system, given lens spacing parameters, and lens dimensions.

Ray transfer matrix analysis (commonly known as ABCD matrix analysis) is a mathematical form of ray tracing, which poses that simple optical systems can be written as the form:

$$
\begin{bmatrix} x_1 \\ \theta_1 \end{bmatrix} = \begin{bmatrix} A & B \\ C & D \end{bmatrix} \begin{bmatrix} x_0 \\ \theta_0 \end{bmatrix}
\tag{D.1}
$$

This is derived from the paraxial approximation, and still requires full ray-tracing to evaluate aberrations as would be required for a full optical design. For design of the FoVSD, propagation and thin lenses were assumed.

Propagation by a distance d has the ABCD matrix:

$$\begin{bmatrix} 1 & d \\ 0 & 1 \end{bmatrix} \tag{D.2}$$

Thin lenses with a focal length f has the ABCD matrix:

$$\begin{bmatrix} 1 & 0 \\ \frac{-1}{f} & 1 \end{bmatrix} \tag{D.3}$$

D.2   Limitations

This basic simulation is limited in that the lenses simulated by matrix D.3 are assumed to be thin. In practise, the lenses used were thick, aspheric plano-convex lenses. The lack of accurate lens simulation led to unexpected coma aberration being present in the system.

Despite these flaws, this basic ray transfer matrix analysis allowed for rapid development of the FoVSD. The software was used to calculate displacements for lens, LCD, and SiPM placement for a the FoVSD, however experiments were required to determine final lens positions, as they were not accurately predicted by the simulation due to the thin lens approximation.

D.3   MATLAB Listing

This code listing combines matrix D.2, and matrix D.3 to arbitrarily simulate lenses at different displacements. `numray` defines the number of rays in the simulation, which enter at the angle `angle` in degrees. The program plots the path of all the rays, and counts the number of rays which strike a 3 mm SiPM detector at the end of the simulation.

```matlab
numray = 300; % number of rays in simulation
angle = 45;   % light input angle in degrees

x1s = linspace(-12.5, 12.5, numray) * 1E-3; % displacement
t1s = deg2rad(angle) * ones(size(x1s));     % angle
```

```matlab
6
7   focal    = [8,   8] * 1E-3;
8   displace = [10, 10] * 1E-3;
9   diameter = [18, 18, 3] * 1E-3;
10
11  in_angle = run_system(x1s, t1s,   displace, focal, diameter);
12  in_0     = run_system(x1s, zeros(size(x1s)), displace, focal,
    ↪  diameter);
13
14
15  function [num_inbounds] = run_system(x1s,t1s, displacement, flength,
    ↪  diameter)
16  % Requires use of the MATLAB Symbolic Toolbox
17
18      % ABCD Matrix for propagation in space
19      propagate = @(d) [1, d; d, 1];
20      % ABCD Matrix for thin lens
21      thinlens = @(f) [1, 0; -1/f, 1];
22      % ABCD Matrix for thick lens (unused)
23      thicklens = @(n1,n2,R1,R2,t) [1, 0; (n2-n1)/(R2*n1), n2/n1] * [1,
    ↪  t; 0, 1] * [1, 0; (n1-n2)/(R1*n2), n1/n2];
24
25      % Propagation distances before first lens, between lenses, and
    ↪  after second lens.
26      a = sym('a',[1 3]);
27
28      % Generate ABCD Matrices for each step between lenses
29      system(:,:,1) = propagate(a(1));
30      system(:,:,2) = propagate(a(2)) * thinlens(flength(1)) *
    ↪  system(:,:,1);
31      system(:,:,3) = propagate(a(3)) * thinlens(flength(2)) *
    ↪  system(:,:,2);
32
33      spacings = [2*1E-3, displacement];
34
35      % Run ABCD Matrix Calculations
36      % Iterate over all parts of optical system
37      for j = 1:size(system,3)
38          % Get start and end of block
39          space = linspace(0,spacings(j), 2);
40          % Iterate over all space between components
41          for k = 1:numel(space)
42              eval(strcat('a',num2str(j), ' = ', num2str(space(k)),';'));
43              sys = double(subs(system(:,:,j)));
44
45              % Iterate over all rays
46              for i = 1:numel(x1s)
47                  x1 = x1s(i);
48                  t1 = t1s(i);
49                  ray = [x1; t1];
50                  out = sys * ray;
51
52                  % Store ray vector position and angle
53                  x2(i,k+(j-1)*2) = out(1);
54                  t2(i,k+(j-1)*2) = out(2);
55              end
56          end
57          eval(strcat("a",num2str(j), "=", num2str(spacings(j)),";"));
58          system = subs(system);
59      end
```

```matlab
60
61      % Array of points in space sampled
62      spacevector = [];
63      for i = 1:numel(spacings)
64          spacevector = [spacevector,
    ↪ spacevector(end)+linspace(0,spacings(i),2)];
65      end
66
67      % Count number of rays striking detector
68      offset = 0;
69      inbounds = true(1,size(x2,1));
70      for i = 1:numel(spacings)
71      offset = offset + 2;
72          in = abs(x2(:,offset)) < sy(i)/2;
73          inbounds = and(inbounds,in');
74      end
75      num_inbounds = sum(inbounds);
76
77      % Plot Result
78      figure();
79      set(0,'DefaultAxesColorOrder',jet(num_inbounds));
80      if sum(inbounds) > 0
81          % If striking detector, color with Jet Colourmap
82          plot(spacevector * 1E3, 1E3 * x2(inbounds,:)');
83      end
84      hold on;
85      if sum(~inbounds) > 0
86          % If not striking detector, Colour rays Grey
87          plot(spacevector * 1E3, 1E3 * x2(~inbounds,:)', 'color',
    ↪ [0.4,0.4,0.4]);
88      end
89      xlabel("Space mm");
90      ylabel("Deflection mm");
91
92      stotal = 0;
93      for i = 1:numel(spacings)
94          s = spacings(i)*1E3;
95          stotal = stotal + s;
96          plot([stotal,stotal],1E3*[-diameter(i)/2, diameter(i)/2], 'm',
    ↪ 'linewidth',3);
97      end
98
99  end
```

References

[1] Chen Siyuan and Wei Yupeng of Huawei. *Addressing Two Challenges to High-Density Wi-Fi Deployment*. 2018. URL: `https://e.huawei.com/hk/publications/global/product-insights/201610261426/focus/201610261441` (visited on 08/11/2018).

[2] Z. Ahmed et al. "A SiPM-Based VLC Receiver for Gigabit Communication Using OOK Modulation". In: *IEEE Photonics Technology Letters* 32.6 (2020), pp. 317–320.

[3] Fahad Zafar, Masuduzzaman Bakaul, and Rajendran Parthiban. "Laser-Diode-Based Visible Light Communication: Toward Gigabit Class Communication". In: *IEEE Communications Magazine* 55.2 (2017), pp. 144–151. DOI: `10.1109/MCOM.2017.1500672CM`.

[4] Svilen Dimitrov and Harald Haas. *Principles of LED Light Communications: Towards Networked Li-Fi*. Cambridge University Press, 2015. DOI: `10.1017/CBO9781107278929`.

[5] *Visible Light Communication*. Cambridge University Press, 2015. DOI: `10.1017/CBO9781107447981`.

[6] Z. Wang et al. "Visible Light Communications : Modulation and Signal Processing". In: 2017.

[7] Zabih Ghassemlooy et al. *Visible light communications: theory and applications*. CRC press, 2017.

[8] Nan Chi et al. "Visible light communications: demand factors, benefits and opportunities [Guest Editorial]". In: *IEEE Wireless Communications* 22.2 (2015), pp. 5–7.

[9] IEEE. *IEEE 802.15 WPAN Task Group 13 (TG13) Multi-Gigabit/s Optical Wireless Communications*. 2018. URL: `http://www.ieee802.org/15/pub/TG13.html` (visited on 09/11/2018).

[10] D. L. HUTT, K. J. SNELL, and P. A. BÉLANGER. "Alexander Graham Bell's PHOTOPHONE". In: *Opt. Photon. News* 4.6 (1993), pp. 20–25. DOI: `10.1364/OPN.4.6.000020`. URL: `https://www.optica-opn.org/abstract.cfm?URI=opn-4-6-20`.

[11] *VA249 Press Kit Intelsat 39 / EDRS-C*. 2023. URL: `http://www.arianespace.com/wp-content/uploads/2019/07/VA249-press-kit_EN.pdf`.

[12] Wajahat Ali et al. "Giga-Bit Transmission Between an Eye-Safe Transmitter and Wide Field-of-View SiPM Receiver". In: *IEEE Access* 9 (2021), pp. 154225–154236. DOI: `10.1109/ACCESS.2021.3116704`.

[13] Edward M.D. Fisher, I. Underwood, and Robert Henderson. "A Reconfigurable Single-Photon-Counting Integrating Receiver for Optical Communications". In: *Solid-State Circuits, IEEE Journal of* 48 (July 2013), pp. 1638–1650. DOI: 10.1109/JSSC.2013.2253222.

[14] Hany Elgala, Raed Mesleh, and Harald Haas. "Indoor optical wireless communication: potential and state-of-the-art". In: *IEEE Communications Magazine* 49.9 (2011), pp. 56–62.

[15] Long Zhang. "Single photon avalanche diodes for visible light communication". PhD thesis. University of Oxford, 2018.

[16] Dario Tagliaferri et al. "Nonlinear visible light communications broadcast channel precoding: A new solution for in-flight systems". In: *IEEE Photonics Journal* 10.4 (2018), pp. 1–14.

[17] Karel Kulhavý. *Ronja Tetrapolis Specification*. 2016. URL: http://ronja.twibright.com/tetrapolis/spec.php.

[18] S. Nishihara et al. "10.3 Gbit/s burst-mode PIN-TIA module with high sensitivity, wide dynamic range and quick response". In: *Electronics Letters* 44.3 (2008), pp. 222–223.

[19] Stefan Lischke et al. "High bandwidth, high responsivity waveguide-coupled germanium p-i-n photodiode". In: *Opt. Express* 23.21 (2015), pp. 27213–27220. DOI: 10.1364/OE.23.027213. URL: http://www.opticsexpress.org/abstract.cfm?URI=oe-23-21-27213.

[20] Long Zhang et al. "A Comparison of APD- and SPAD-Based Receivers for Visible Light Communications". In: *J. Lightwave Technol.* 36.12 (2018), pp. 2435–2442. URL: http://jlt.osa.org/abstract.cfm?URI=jlt-36-12-2435.

[21] *Introduction to the Silicon Photomultiplier (SiPM)*. 2018. URL: https://www.onsemi.com/pub/Collateral/AND9770-D.PDF.

[22] Stefan Gundacker and Arjan Heering. "The silicon photomultiplier: fundamentals and applications of a modern solid-state photon detector". In: *Physics in Medicine; Biology* 65.17 (2020), 17TR01. DOI: 10.1088/1361-6560/ab7b2d. URL: https://doi.org/10.1088/1361-6560/ab7b2d.

[23] Wajahat Ali et al. "Silicon photomultiplier receivers and future VLC systems". In: *2020 IEEE Globecom Workshops (GC Wkshps*. 2020, pp. 1–5. DOI: 10.1109/GCWkshps50303.2020.9367590.

[24] Danial Chitnis and Steve Collins. "A SPAD-Based Photon Detecting System for Optical Communications". In: *J. Lightwave Technol.* 32.10 (2014), pp. 2028–2034. URL: https://opg.optica.org/jlt/abstract.cfm?URI=jlt-32-10-2028.

[25] Zubair Ahmed et al. "A Comparison of VLC Receivers That Incorporate Two Different SiPMs". In: *IEEE Photonics Journal* 15.2 (2023), pp. 1–8. DOI: 10.1109/JPHOT.2023.3239112.

[26] Z. Ahmed et al. "A Shot-Noise Limited 420 Mbps Visible Light Communication System using Commerical Off-the-Shelf Silicon Photomultiplier (SiPM)". In: *2019 IEEE International Conference on Communications Workshops (ICC Workshops)*. 2019, pp. 1–5.

[27] C.E. Shannon. "Communication in the Presence of Noise". In: *Proceedings of the IRE* 37.1 (1949), pp. 10–21. DOI: 10.1109/JRPROC.1949.232969.

[28] R. V. L. Hartley. "Transmission of information". In: *The Bell System Technical Journal* 7.3 (1928), pp. 535–563. DOI: 10.1002/j.1538-7305.1928.tb01236.x.

[29] Dominic O'Brien, Sujan Rajbhandari, and Hyunchae Chun. "Transmitter and receiver technologies for optical wireless". English. In: *Philosophical transactions. Series A, Mathematical, physical, and engineering sciences* 378.2169 (Apr. 2020). ISSN: 0962-8428. DOI: 10.1098/rsta.2019.0182.

[30] *J-Series SiPM Sensors Silicon Photomultipliers(SiPM), High PDE and Timing Resolution Sensors in a TSV Package*. 2019. URL: https://www.onsemi.com/pub/Collateral/MICROJ-SERIES-D.PDF.

[31] *Silicon Photomultipliers (SiPM), Low-Noise, Blue-Sensitive C-Series SiPM Sensors*. 2019. URL: https://www.onsemi.com/pdf/datasheet/microc-series-d.pdf.

[32] Honglei Li et al. "High Bandwidth Visible Light Communications Based on a Post-Equalization Circuit". In: *IEEE Photonics Technology Letters* 26.2 (2014), pp. 119–122. DOI: 10.1109/LPT.2013.2290026.

[33] Honglei Li et al. "A 550 Mbit/s real-time visible light communication system based on phosphorescent white light LED for practical high-speed low-complexity application". In: *Opt. Express* 22.22 (2014), pp. 27203–27213. DOI: 10.1364/OE.22.027203. URL: https://opg.optica.org/oe/abstract.cfm?URI=oe-22-22-27203.

[34] Stefan Lischke et al. "High bandwidth, high responsivity waveguide-coupled germanium p-i-n photodiode". In: *Opt. Express* 23.21 (2015), pp. 27213–27220. DOI: 10.1364/OE.23.027213. URL: https://opg.optica.org/oe/abstract.cfm?URI=oe-23-21-27213.

[35] D. Milovančev et al. "VLC Using 800-μm Diameter APD Receiver Integrated in Standard 0.35-μm BiCMOS Technology". In: *IEEE Photonics Journal* 13.1 (2021), pp. 1–13. DOI: 10.1109/JPHOT.2020.3036549.

[36] T. Jukić et al. "200 μm APD OEIC in 0.35 μm BiCMOS". English. In: *Electronics Letters* 52 (2 2016), 128–130(2). ISSN: 0013-5194. URL: https://digital-library.theiet.org/content/journals/10.1049/el.2015.3540.

[37] William Matthews et al. "A SiPM-based VLC Receiver for 3.45 Gigabits/s Communication Using OOK Modulation". In: *2020 IEEE Photonics Conference (IPC)*. 2020, pp. 1–2. DOI: 10.1109/IPC47351.2020.9252218.

[38] William Matthews et al. "A 3.45 Gigabits/s SiPM-Based OOK VLC Receiver". In: *IEEE Photonics Technology Letters* 33.10 (2021), pp. 487–490. DOI: 10.1109/LPT.2021.3069802.

[39] W. Ali et al. "A wide field-of-view receiver that incorporates fluorescent fibers and a SiPM". In: 2021.

[40] William Matthews, Cuiwei He, and Steve Collins. "DCO-OFDM Channel Sounding with a SiPM Receiver". In: *2021 IEEE Photonics Conference (IPC)*. 2021, pp. 1–2. DOI: 10.1109/IPC48725.2021.9592851.

[41] Long Zhang et al. "The Future Prospects for SiPM-Based Receivers for Visible Light Communications". In: *Journal of Lightwave Technology* 37.17 (2019), pp. 4367–4374. DOI: 10.1109/JLT.2019.2923957.

[42] Z Ahmed. "Silicon photomultipliers for visible light communications". PhD thesis. University of Oxford, 2022.

[43] William Matthews and Steve Collins. "A roadmap for multi-Gigabit to Terabit free space optical communications receivers". In: *MDPI Sensors* 23(3).1101 (2023), pp. 1–22. ISSN: 1424-8220. DOI: 10.3390/s23031101.

[44] "Forward Error Correction for High Bit Rate DWDM Submarine Systems". In: *Standard ITU-Recommendation G. 975.1, Int. Telecommun. Union, Geneva, Switzerland* (2004).

[45] Shenjie Huang and Majid Safari. "Hybrid SPAD/PD Receiver for Reliable Free-Space Optical Communication". In: *IEEE Open Journal of the Communications Society* 1 (2020), pp. 1364–1373. DOI: 10.1109/OJCOMS.2020.3023009.

[46] Horst Zimmermann. "APD and SPAD Receivers : Invited Paper". In: *2019 15th International Conference on Telecommunications (ConTEL)*. 2019, pp. 1–5. DOI: 10.1109/ConTEL.2019.8848547.

[47] Yuanquan et al. Wang. "Demonstration of 575-Mb/s downlink and 225-Mb/s uplink bi-directional SCM-WDM visible light communication using RGB LED and phosphor-based LED". In: *Optics express* 21 (2013). DOI: 10.1364/OE.21.001203.

[48] Rui Bian, Iman Tavakkolnia, and Harald Haas. "15.73 Gb/s Visible Light Communication With Off-the-Shelf LEDs". In: *Journal of Lightwave Technology* 37.10 (2019), pp. 2418–2424. DOI: 10.1109/JLT.2019.2906464.

[49] William Matthews et al. "Inter-Symbol Interference and Silicon Photomultiplier VLC Receivers in Ambient Light". In: *IEEE Photonics Technology Letters* 33.9 (2021), pp. 449–452. DOI: 10.1109/LPT.2021.3067511.

[50] W. Matthews and S. Collins. "The negative impact of anode resistance on SiPMs as VLC receivers". In: *2022 PRIME Conference*. 2022.

[51] William Matthews and Steve Collins. "An experimental and numerical study of the impact of ambient light of SiPMs in VLC receivers". In: *MDPI Photonics* 9(12).888 (2022), pp. 1–17. ISSN: 2304-6732. DOI: 10.3390/photonics9120888.

[52] Slawomir Piatek. "Measuring the electrical and optical properties of silicon photomultipliers". In: *Hamamatsu Technical Notes* (2014). URL: https://hub.hamamatsu.com/us/en/technical-notes/mppc-sipms/measuring-the-electrical-and-optical-properties-of-silicon-photomultipliers.html.

[53] Tasnim Hamza and Mohammad Ali Khalighi. "On Limitations of Using Silicon Photo-Multipliers for Underwater Wireless Optical Communications". In: *2019 2nd West Asian Colloquium on Optical Wireless Communications (WACOWC)*. 2019, pp. 74–79. DOI: 10.1109/WACOWC.2019.8770202.

[54] Yichen Li et al. "Nonlinear Distortion in SPAD-Based Optical OFDM Systems". In: *2015 IEEE Globecom Workshops (GC Wkshps)*. 2015, pp. 1–6. DOI: 10.1109/GLOCOMW.2015.7414148.

[55] Wajahat Ali et al. "The Impact of the Length of Fluorescent Fiber Concentrators on the Performance of VLC Receivers". In: *IEEE Photonics Technology Letters* 33.24 (2021), pp. 1451–1454. DOI: 10.1109/LPT.2021.3115965.

[56] Andrea Goldsmith. *Wireless Communications*. Cambridge University Press, 2005. DOI: 10.1017/CBO9780511841224.

[57] *Signal Driven Multiplexing of Silicon Photomultiplier Arrays*. URL: https://www.onsemi.com/pub/Collateral/AND9772-D.PDF.

[58] Cuiwei He et al. "Angular Diversity Aperture (ADA) Receivers for Indoor Multiple-Input Multiple-Output (MIMO) Visible Light Communications (VLC)". In: *IEEE Access* 7 (2019), pp. 145282–145301. DOI: 10.1109/ACCESS.2019.2945075.

[59] P. Ruiz et al. "Light field acquisition from blurred observations using a programmable coded aperture camera". In: *21st European Signal Processing Conference (EUSIPCO 2013)*. 2013, pp. 1–5.

[60] M. Grosse et al. "Coded Aperture Projection". In: *ACM Trans. Graph.* 29.3 (2010), pp. 1–12.

[61] A. Zomet and S.K. Nayar. "Lensless Imaging with a Controllable Aperture". In: *IEEE Conference on Computer Vision and Pattern Recognition (CVPR)*. 2006.

[62] Jie Lian et al. "Indoor visible light communications, networking, and applications". In: *Journal of Physics: Photonics* 1.1 (2019), p. 012001. DOI: 10.1088/2515-7647/aaf74a. URL: https://dx.doi.org/10.1088/2515-7647/aaf74a.

[63] Vipul Dixit and Atul Kumar. "Performance analysis of angular diversity receiver based MIMO-VLC system for imperfect CSI". In: *Journal of Optics* 23.8 (2021), p. 085701. DOI: 10.1088/2040-8986/ac1321. URL: https://dx.doi.org/10.1088/2040-8986/ac1321.

[64] Dominic O'Brien. "Beamsteering for ultra-high data-rate optical wireless communications". In: Feb. 2019, p. 19. DOI: 10.1117/12.2506266.

[65]   Yusuf Said-Eroglu et al. "Slow Beam Steering for Indoor Multi-User Visible Light Communications". In: *2018 IEEE 19th International Workshop on Signal Processing Advances in Wireless Communications (SPAWC)*. 2018, pp. 1–5. DOI: `10.1109/SPAWC.2018.8445955`.

[66]   Crisanto Quintana et al. "Ultra-wide coverage VLC system with alignment-free receiver". In: *2018 Global LIFI Congress (GLC)*. 2018, pp. 1–4. DOI: `10.23919/GLC.2018.8319104`.

[67]   Osama Zwaid Aletri, Mohammed T. Alresheedi, and Jaafar M. H. Elmirghani. "Infrared Uplink Design for Visible Light Communication (VLC) Systems with Beam Steering". In: *2019 IEEE International Conference on Computational Science and Engineering (CSE) and IEEE International Conference on Embedded and Ubiquitous Computing (EUC)*. 2019, pp. 57–60. DOI: `10.1109/CSE/EUC.2019.00020`.

[68]   *IEEE P802.11 Wireless LANs TGbb Simulation Scenarios*. 2021. URL: `https://mentor.ieee.org/802.11/dcn/18/11-18-1423-08-00bb-tgbb-simulation-scenarios.docx`.

[69]   H Chun et al. "A wide-area coverage 35 Gb/s visible light communications link for indoor wireless applications". In: *Scientific Reports* 9.2019 (2019), Article:4952.

[70]   National Research and Energy Laboratory. "Reference Air Mass 1.5 Spectra". In: *NREL Grid Modernization* (2023). URL: `https://www.nrel.gov/grid/solar-resource/spectra-am1.5.html`.

[71]   *Status of IEEE 802.11 Light Communication TG*. 2023. URL: `https://grouper.ieee.org/groups/802/11/Reports/tgbb_update.htm`.

[72]   Bastien Béchadergue et al. "Indoor Optical Wireless Communication Coverage Optimization Using a SiPM Photoreceiver". In: *2023 IEEE Wireless Communications and Networking Conference (WCNC)*. 2023, pp. 1–6. DOI: `10.1109/WCNC55385.2023.10118956`.

[73]   Long Zhang et al. "Performance Estimation and Selection Guideline of SiPM Chip within SiPM-Based OFDM-OWC System". In: *Photonics* 9.9 (2022). ISSN: 2304-6732. DOI: `10.3390/photonics9090637`. URL: `https://www.mdpi.com/2304-6732/9/9/637`.

[74]   Zhenzhou Deng et al. "A Novel Visible Light Communication System Based on a SiPM Receiver". In: *Proceedings of the 4th International Conference on Telecommunications and Communication Engineering*. Ed. by Maode Ma. Singapore: Springer Singapore, 2022, pp. 98–111. ISBN: 978-981-16-5692-7.

[75]   Yi Liu et al. "High-capacity optical wireless VCSEL array transmitter with uniform coverage". In: *Free-Space Laser Communications XXXV*. Ed. by Hamid Hemmati and Bryan S. Robinson. Vol. 12413. International Society for Optics and Photonics. SPIE, 2023, 124130J. DOI: `10.1117/12.2649265`. URL: `https://doi.org/10.1117/12.2649265`.

[76]   Feng Liu et al. "Ultra-Sensitive UV Solar Blind Optical Wireless Communications with SiPM". In: *In Draft* (2023).

[77] Guanxiong Zhang et al. "Free-Space Optical Communication Link with Liquid Crystal Beam-steering". In: *IEEE Photonics Technology Letters (In Review)* (2023).

[78] Shenjie Huang et al. "5 Gbps optical wireless communication using commercial SPAD array receivers". In: *Opt. Lett.* 47.9 (2022), pp. 2294–2297. DOI: 10.1364/OL.454994. URL: http://opg.optica.org/ol/abstract.cfm?URI=ol-47-9-2294.

[79] Susanne Klein. "Optical Efficiency for Different Liquid Crystal Colour Displays". In: *HP Labs Technical Reports* (June 2000).

[80] Cuiwei He, Zubair Ahmed, and Steve Collins. "Signal Pre-Equalization in a Silicon Photomultiplier-Based Optical OFDM System". In: *IEEE Access* 9 (2021), pp. 23344–23356. DOI: 10.1109/ACCESS.2021.3056148.

[81] *UK frequency allocation table (UKFAT)*. URL: http://static.ofcom.org.uk/static/spectrum/fat.html.

[82] William Matthews. *SimSPAD*. Version 0.2.2. June 2023. URL: https://github.com/WillMatthews/SimSPAD.

[83] GitHub Contributors. *cpp-httplib*. Version 0.12.6. June 2023. URL: https://github.com/yhirose/cpp-httplib.

[84] Mihai Baidu. Private Communication. Mar. 10, 2023.